

A Quantum Gas of Polar Molecules

by

Kang-Kuen Ni

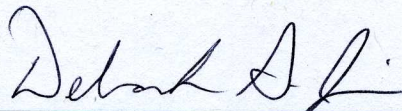
B.S. Creative Studies, University of California, Santa

Barbara, 2003

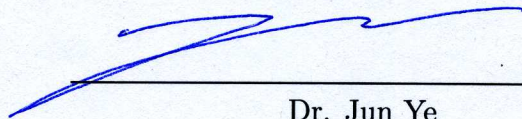
A thesis submitted to the
Faculty of the Graduate School of the
University of Colorado in partial fulfillment
of the requirements for the degree of
Doctor of Philosophy
Department of Physics

2009

This thesis entitled:
A Quantum Gas of Polar Molecules
written by Kang-Kuen Ni
has been approved for the Department of Physics



Dr. Deborah S. Jin



Dr. Jun Ye

Date Oct. 28, 2009

The final copy of this thesis has been examined by the signatories, and we find that both the content and the form meet acceptable presentation standards of scholarly work in the above mentioned discipline.

Ni, Kang-Kuen (Ph.D., Physics)

A Quantum Gas of Polar Molecules

Thesis directed by Professor Dr. Deborah S. Jin

Ultracold polar molecular gases promise new directions and exciting applications in precision measurements, ultracold chemistry, electric-field controlled collisions, dipolar quantum gases, and quantum information sciences. This thesis presents experimental realization of a near quantum degenerate gas of polar molecules, where the phase-space density of the gas achieved is more than 10 orders of magnitude higher than previous results. The near quantum degenerate gas of polar molecules is created using two coherent steps. First, atoms in an ultracold gas mixture are converted into extremely weakly bound molecules near a Fano-Feshbach resonance. Second, the weakly bound molecules are transferred to the ro-vibronic ground state using a coherent two-photon Raman technique. The fact that these ground-state molecules are polar is confirmed with a spectroscopic measurement of the permanent electric dipole moment. Finally, manipulation of the molecular hyperfine state is demonstrated; this allows molecules to be populated in a *single* quantum state, in particular, the *lowest* energy state. With an ultracold gas of molecules, full control of molecular internal state, and electric field as a new handle, ultracold molecular collisions, including ultracold chemical reactions and dipolar collisions, are studied.

Dedication

For Ruey-Shiang, Wei-Tou, Kangyu, and Till

Acknowledgements

First, I would like to thank my advisors, Debbie Jin, Jun Ye, and Carl Wieman. Carl convinced me to come to JILA and started up the KRb project with another graduate student, Josh Zirbel. Although he was only around during my first three years of graduate school when we were still building the main apparatus, I have learned tremendous amount of technical skills as well as scientific ways of thinking from him. Here, I would like to share a private email from Carl on his thought as what one should learn in graduate school and hopefully it also summed up the excellent education I got here in JILA. “The thing that I believe is absolutely essential is that the students leave graduate school able to function as independent scientists. This means understanding and evaluating what topics in their field are worthwhile (or not), and being able to design and carry out good research projects. For my students, that includes getting a lot of expertise in a variety of experimental technologies and techniques, being able to design and build complex apparatus and make it work, being able to carry out and analyze good experiments, be able to present their work well both in speaking and writing, and being able to work effectively with collaborators. And of course there is learning to work hard in a focused efficient manner. These are all the aspects of what it takes to be a good scientist, and I believe that if a student masters this working on something like a cold atom experiment with me, they should be able to move successfully into many other areas of research or teaching later on as they choose...”

I am privileged to continue and finish my thesis with Debbie. She became my advisor during the period that I have learned and grown the most scientifically in grad school. Debbie has an amazing intuition in physics. She never let all the technical and even conceptual details get in the way of understanding the simplest and the big picture ideas while still being extremely rigorous and careful. I thank her for being patient and critical of my writings, my presentations, and my being as a student and a researcher. I am always amazed by how much she is available to us. There were countless times when we would chat from experimental problems to things in daily life for hours and hours.

I am also very fortunate to work and to learn from Jun. His optimistic and enthusiastic spirits have encouraged me numerous times when I was feeling pessimistic or frustrated. In addition, he has an infinite bank of technical knowledge and physics intuitions that always help to solve our problems. He is one of the few advisors who can still turn knobs on an optical table and make things better!

I have benefited as a physicist and a person from spending long hours a day for many years with Josh Zirbel and Silke Ospelkaus. Josh has infinite patient teaching me how to align optics, build circuits, prepare vacuum, and diagnose problems. We have spent many years together in the dark basement constructing our apparatus. Although we built the apparatus together, most of the credit should go to him for leading the effort and setting the high standards for making things work well in the lab. The robust KRb system is the key to our success that both Josh and I as well as other KRb members have benefited greatly from. I am very excited that both of us have survived grad school after years of discouragements and frustrations from all the technical and the scientific challenges and now be ready for anything in the future.

This thesis would not have been accomplished in the “timely” fashion without the collaboration with Silke. Silke joined Josh and I at the time when we

were working toward our first result. She immediately taught us how to work efficiently toward fruitful results. Over the next two and a half years, I have learned a tremendous amount from her and enjoy working with her greatly. Together with Silke, there is nothing we cannot accomplish!

I would also like to thank other members on the project, Avi Pe'er, Marcio Miranda, Brian Neyenhuis, and Dajun Wang, who contributed a great deal in making this thesis happen. Avi had been thinking about making molecules even before joining our collaborated project and immediately elevated my understanding of working toward making deeply bound molecules. Marcio joined us with his expertise of working with a frequency comb. He had always helped us advancing toward our next goal. Brian had joined us a few years back and helped with numerous projects allowed us to be always progressing. Dajun joined with a great amount of knowledge of KRb spectroscopy and helped us make our way through our own vast amount of spectroscopy data. Silke and I have now left this wonderful experiment in the hands of Marcio, Brian, and Dajun, who I am sure will soon bring more exciting news from the project.

Our project would not have been successful without collaborations with many theorists. Svetlana Kotochigova and Paul Julienne have helped us find a way to make absolute ground-state molecules. They have been extremely nice and generous with their time to be always answering our questions with pages of emails promptly. Goulven Quémener and John Bohn are in-house theorists who happen to be the world experts on polar molecules and ultracold collisions. I thank them for their theoretical insights and for never saying “no” to any thing we asked them to calculate. I enjoy discussing and talking to them with all the exciting happenings with KRb even outside the dedicated three continuous hours every week. I also like to thank Dominic Meiser who is an expert on Mathematica for always helping me with anything Mathematica.

JILA has been a wonderful place to work. With the collaborative atmosphere in JILA, we have numerous weekly meetings. One of them is the “tri-group” meeting. I thank Eric Cornell and all the members of the tri-group, who are the most supportive fellow group members, for always sharing their expertise, equipments, and most importantly lunch discussions. I thank the Ye group members, especially Brian Sawyer and Ben Stuhl who work on Stark decelerating molecules, for sharing expertise and helping me simulate electric fields that are relevant for our experiments. I also thank friends in graduate school, in particular Stephanie Meyer, David Hume, Adam Pearlstein, Brian Seaman, Rajiv Bhat, Meret Kramer, Murray Holland, Ying-ju Wang, and Wengang Zhang.

Members of JILA electronic and machine shops and IT department, in particular, Terry Brown, Carl Sauer, Mike Whitmore, James Fung-A-Fat, Blaine Horner, Hans Greene, Tracy Keep, Todd Asnicar, Tom Foote, Ariel Paul, Kim Hagen, and J. R. Raith, are the professional help who have contributed to our work. I thank all the JILA staff who had made it easy with all the purchasing, traveling, computer related issues, etc. In particular, I thank Krista Beck for her assistance over the years while being an assistant to Carl and Debbie.

My family have provided me with constant support even when they are far away. My father (Dr. Ni #1 in my family) has always been enthusiastic about discussing physics through long-distance phone calls and helped me stay motivated throughout the years. My mother has provided infinite support and always has great confidence in me. My sister, who has become Dr. Ni #7 in my family last year was in grad school with me throughout the same time. Going through grad school together encouraged me during many periods of low time.

Finally, I would like to thank Till Rosenband for his Mathematica and ANSYS wizardry. I thank him for his unconditional support and his company for numerous adventures together.

Contents

Chapter	
1	Introduction 1
1.1	Why Ultracold Polar Molecules? 1
1.2	Overview of the Thesis 2
1.3	Dipole-Dipole Interaction 8
1.3.1	Ultracold Collisions of Dipoles 10
1.3.2	Dipolar Quantum Gas 15
1.4	Contents of this Thesis 16
2	Challenges for Making Ultracold Polar Molecules 17
2.1	Introduction 17
2.2	Direct Cooling of Molecules 18
2.3	Photo-association 19
2.4	Fully Coherent Scheme 23
3	Apparatus 26
3.1	K-Rb Machine 26
3.2	Electric-field Plates 30
3.3	Molecular Spectroscopy Lasers 32
3.3.1	Widely Tunable Ti:sapphire Laser 32
3.3.2	Diode Lasers 33

3.3.3	Ti:sapphire Comb	34
3.3.4	Phase Locking	35
4	Feshbach Molecules	40
4.1	Heteronuclear Feshbach Molecules	41
4.1.1	Conversion Efficiency	43
4.1.2	Lifetime	44
4.1.3	Electric Dipole Moment	46
4.2	Enhancement Factor	48
4.3	Detection	49
5	KRb* Potentials	54
5.1	Hund's Coupling Cases	54
5.1.1	Hund's Case (a)	56
5.1.2	Hund's Case (b)	56
5.1.3	Hund's Case (c)	57
5.2	Near-Threshold States	57
5.2.1	$v' = -14$ of $2(0^-)$	62
5.3	Bridging to Deeply Bound Molecules	62
5.4	$2^3\Sigma^+$ and the $\Omega = 0^-$ and $\Omega = 1$ Components	63
5.4.1	$v' = 10$ of $2^3\Sigma^+$ ($\Omega = 0^-$)	65
5.4.2	$v' = 23$ of $2^3\Sigma^+$ ($\Omega = 1$)	70
6	Coherent Two-Photon Raman Transfer	72
6.1	Three-level System	73
6.2	Dark Resonance	76
6.3	Detuned STIRAP, $v = -3$	79
6.4	Extending STIRAP to Deeply Bound States	81

7	Triplet Rovibrational Ground-State Molecules	
	($N = 0, v = 0$ of $a^3\Sigma^+$)	87
7.1	Scheme	87
7.2	Hyperfine-rich Ground-state Structure	89
7.3	Stark Spectroscopy	93
7.4	Transfer	95
8	Absolute Ro-Vibronic Ground-State Polar Molecules	
	($N = 0, v = 0$ of $X^1\Sigma^+$)	98
8.1	Transfer Scheme	100
8.2	Two-photon Spectroscopy	100
8.3	Stark Spectroscopy Analysis	102
8.4	Population Transfer	106
8.5	Trapped Molecular Temperature and Density	109
9	Identifying and Manipulating Molecular Hyperfine States	114
9.1	Identify Hyperfine States	116
9.2	Manipulate Molecular Hyperfine States	117
9.2.1	State Transfer to the Lowest Hyperfine State	117
9.2.2	More Hyperfine Spectroscopy	120
10	Ultracold Chemistry and Inelastic Collisions	123
10.1	Atom-Molecule Collisions	124
10.2	Universal Loss Rate	128
10.3	Molecule-Molecule Collisions	129
10.3.1	p -wave Collisions	131
10.3.2	s -wave Collisions	135

11	Electric Dipole-Dipole Collisions	137
11.1	Working with Electric Dipoles	137
11.1.1	E-field Gradients	138
11.1.2	Fringing Fields and a Non-symmetric Ground Plane	140
11.2	Inelastic Dipolar Collisions	143
11.2.1	Anisotropy of Losses	145
11.2.2	Anisotropic Heating	147
11.3	Elastic Dipolar Collisions	150
11.4	Cross-dimensional Rethermalization	151
12	Conclusions and Future Directions	155
12.1	Conclusion	155
12.2	Future Work	156
	Bibliography	158
	Appendix	
A	Sample Mathematica Code	168
B	Tapered Amplifier Design	172

Chapter 1

Introduction

1.1 Why Ultracold Polar Molecules?

The brand new field of ultracold polar molecules is motivated by the success of ultracold atoms. Ultracold atomic gases have provided many exciting and diverse applications including atomic clocks, precision tests of fundamental physics, sensors of tiny forces, and new architectures for quantum information. These systems are miniature laboratories for studying ultracold collisions, resonances, and few-body physics. They also provide model systems where one can explore many-body quantum phenomena such as Bose-Einstein condensation, superfluidity, and Fermi superfluidity. The underlying basis for these many uses is that ultracold atomic gases can be trapped, interrogated for long times, and precisely controlled at the quantum level, in both the atoms' internal (i.e. electronic, fine, and hyperfine) and external degrees of freedom (i.e. motional state in the laboratory frame). Extending this type of control to an ultracold gas of polar molecules opens exciting new research directions because of the richer energy level structure of molecules, the possibility for reactive collisions, and the relatively strong and long-range electric dipole-dipole interaction between polar molecules.

The rich energy level structure of molecules, which includes rotational and vibrational levels, opens new possibilities for precision measurements [1, 2, 3]. One example is the search for a permanent electric dipole moment of the electron,

where polar molecules can provide much larger internal electric fields than could be directly applied to electrons in the lab or inside an atom. The more complex internal states of polar molecules will also enable the development of new tools for controlling and manipulating ultracold gases. In the arena of ultracold collisions, polar molecule gases offer electric-field tuning of interactions [4], access to new types of resonances [5], and ultracold chemistry [6]. For quantum information applications, the relatively strong dipole-dipole interaction, which can be switched on and off as desired with an applied external electric field, offers a means for controlled creation of entangled states [7, 8, 9]. The dipole-dipole interaction, which is long-range as opposed to the contact interaction of ultracold atoms, could also be exploited in quantum gases of polar molecules to realize novel phases of matter [10, 11, 12].

1.2 Overview of the Thesis

This thesis tells the story of our quest to make and study a quantum gas of ground-state polar molecules. This has been a long-standing goal in the ultracold gas community since the creation of quantum degenerate atomic gases more than a decade ago [13, 14]. The work described in this thesis demonstrated creation of an ultracold gas of ground-state polar molecules [15] that is more than 10 orders of magnitude higher in phase-space density than previously achieved and is only a factor of 15 in phase-space density away from quantum degeneracy. Phase-space density is defined as $n\Lambda^3$, where n is the peak density of the gas and Λ is the thermal de Broglie wavelength.

In 2002, Carl Wieman, Debbie Jin, and Jun Ye at JILA began planning a collaborative ultracold molecule experiment that would use their respective expertise. This was during the exciting time when the Wieman group was using a Fano-Feshbach resonance to form Rb_2 Feshbach molecules in a Bose-Einstein

condensate and seeing coherent atom-molecule oscillations [16], and the Jin group had just observed the first evidence of K_2 Feshbach molecules in a quantum degenerate Fermi gas [17]. It was thought that as a first step toward ultracold polar molecules, we should develop the technology of making and understanding heteronuclear Feshbach molecules. Then, we would team up with the Ye group to find a way of transferring Feshbach molecules to the absolute ground state. Shortly after formulating the idea, Josh Zirbel and I began constructing our apparatus in the summer of 2003. A detailed description of the apparatus is in J. Zirbel's thesis [18].

Making a quantum gas of polar molecules is challenging in part due to the same complex internal structure that makes molecules an interesting and richer system compared to an atomic system. There are, in general, two cooling approaches. One is to directly cool molecules to low translational temperatures. However, all the cooling methods demonstrated so far can only reach down to the mK regime with a trapped gas density of 10^8 cm^{-3} or below. This corresponds to a phase-space density of the order 10^{-13} [19, 20, 21]. The other approach is to associate pairs of ultracold atoms into tightly bound molecules. The main difficulty with this approach is to find a way to efficiently convert atoms that are usually very far apart to tightly bound molecules without allowing the released binding energy to heat up the gas. In 2005, Sage *et al.* [22] demonstrated a scheme where they could make about 10 RbCs molecules in their absolute rovibrational ground-state from 10^8 laser-cooled atoms in a single transfer cycle, with a gas phase-space density achieved on the order 10^{-14} . Their result highlighted a general scheme as well as the challenges to convert ultracold atoms into tightly bound molecules.

To make a quantum gas of polar molecules in their absolute ground state (lowest vibrational, rotational, and electronic ground state), we perform a two-

step coherent transfer process. In the first step, we make weakly bound Feshbach molecules from a quantum degenerate mixture of K and Rb atoms. In the second step, we shrink the size of the molecules to reach the absolute ground state using a *single-step* of two-photon Raman transfer. The first step is described in J. Zirbel’s thesis [18]. Although I will cover the whole story in this thesis, I will focus more on the second step, which is surprisingly efficient. This “surprising” result was built on a step-by-step learning process that started after making and understanding KRb Feshbach molecules in 2006 (in Hamburg) [23] and 2007 (in our group) [24]. The work presented in this thesis was done in collaboration with many people, in particular with Silke Ospelkaus.

Once weakly bound Feshbach molecules are available, it is necessary to use a fully coherent transfer technique to manipulate their internal state to reach the absolute ro-vibronic ground state. Coherent transfer ensures that the molecules all populate a single internal quantum state and that the ultracold gas is not heated in the process. In 2007, Winkler *et al.* [25] demonstrated robust and highly efficient state transfer of homonuclear Rb₂ Feshbach molecules to their second least bound state (vibrational level $v = -2$ and binding energy $E_b = h \cdot 637$ MHz) using a coherent two-photon Raman transfer technique. We implemented the same technique in our heteronuclear system (which would allow us eventually to make polar molecules), and demonstrated transfer of KRb Feshbach molecules to another near-threshold vibrational state, $v = -3$ ($h \cdot 10$ GHz) [26]. The efficient transfer relies on (1) identifying a suitable electronically excited intermediate state that has large Franck-Condon factors (FCFs) to both the initial and the target states and (2) maintaining phase coherence of the two laser beams that drive the transfer process. For transfer from Feshbach molecules to another near-threshold (weakly bound) molecular state, a suitable intermediate state is relatively easy to find, although one must consider possible constraints from selection rules. It

turns out that the most important thing is to find an isolated line that makes the system an “ideal” three-level system.

For transfer to near-threshold molecular states, maintaining phase coherence of the two Raman beams, which have a beat frequency of tens of GHz or below is straightforward using good electronics and commercial photodiodes and synthesizers. However, it is a challenge to extend the technique for our next step of reaching more deeply bound states. To allow transfer to any arbitrary deeper bound molecular state and even to the absolute ground state, we implemented a stabilized optical frequency comb that spans the wavelength range from 532 nm to 1064 nm. The comb laser provides a stable reference that allows us to maintain phase coherence of any two or more lasers in this large wavelength range.

With a Raman laser system capable of reaching deeply bound molecular states, the next issue is finding a suitable intermediate state that allows us to bridge the enormous difference between the wave functions of Feshbach molecules and deeply bound molecules. Although our ultracold gas apparatus typically yields spectroscopy data with extremely high sensitivity and accuracy, it has a relatively low duty cycle compared to conventional spectroscopy experiments. Therefore, we needed to choose a scheme carefully and used all available data from conventional spectroscopy to narrow down our search. Given our previous experience in searching for intermediate states near threshold, it appeared to be a daunting task to follow the vibrational series (for both excited state and ground state) from threshold to the deeply bound regime. For example, the ground state potentials alone support 132 vibrational levels.

It was after discussions with our theoretical collaborators, Svetlana Kotochigova and Paul Julienne, that we understood both the advantages and the challenges for instead directly searching for a low vibrational (low- v) ground state. The advantage is that conventional hot molecule spectroscopy has precise infor-

mation specifically for the low- v states [27, 28]. Their data allows an accurate construction of the molecule potential in the region where it is, to a good approximation, harmonic, which yields a relatively small uncertainty of the absolute ground-state location. Therefore, if we could identify a suitable intermediate state with good FCFs to both the initial Feshbach molecules and our desired low- v state, the search for the target state would have a finite range to cover. Identifying such an intermediate state in the “forest” of excited-state potentials also required significant theoretical calculations and a full knowledge of what experimental spectroscopy was already available.

Working in the low- v regime, we first demonstrated transfer to the triplet rovibrational ground state. Encouraged by these results, we then pursued transfer to the absolute ro-vibronic ground state. We chose a scheme that used an intermediate state that was similar to the photoassociation work by Sage *et al.* [22]. This choice was partially based on the demonstration by Sage *et al.* for RbCs and partially based on the fact that related spectroscopy data was available [27]. Although the predicted transition strengths were relatively small, we were hopeful that we could achieve reasonable coupling strengths because we were working with a near quantum degenerate gas where the cloud size is very small and the coupling Raman lasers can be focused to a very tight spot for a high intensity.

In 2008, to the surprise of the community and to our own delight, we were able to perform a *single-step* of STImulate Raman Adiabatic Passage (STIRAP) to transfer 90% of Feshbach molecules to the absolute ground state. At nearly the same time, two other groups reported using a similar technique to transfer homonuclear Cs₂ and Rb₂ Feshbach molecules into their respective deeply bound states [29, 30]. Since then, we have identified and manipulated the hyperfine state of the ground-state molecules. In particular, we can create molecules that not only populate a *single* hyperfine state, but we also have the ability to put them in *any*

desired hyperfine state. The robust production of absolute ground-state molecules in any desired hyperfine state aided in our first exploration of the basic collisional properties of ground-state KRb molecules. We investigated inelastic/reactive for both atom-molecule and molecule-molecule collisions. For atom-molecule collisions, we could prepared all species, K, Rb, and KRb, in the lowest energy states. We observed KRb loss due to ultracold chemical reactions with K. When either Rb or KRb were in an excited hyperfine state, we observed hyperfine-state-changing collisions. We then removed all the atoms and began to explore molecule-molecule collisions. The KRb molecules we create are indistinguishable fermions prepared at a temperature of a few hundreds of nano-Kelvin, which is below the height of the p -wave barrier of $k_b \cdot 24 \mu\text{K}$ [31]. Molecules collisions via s -wave are not allowed by the quantum statistics and collisions via p -wave are suppressed by the barrier. We observed molecule collisions via tunneling through the p -wave barrier followed by a near unit-probability of chemical reactions at short-range. For distinguishable fermions (molecules prepared in two different spin states) and s -wave collisions, the collision rates are enhanced by a factor of 10-100.

Understanding basic collisional properties of molecules allowed us begin to explore one unique feature of polar molecules – their *large* and *tunable* electric dipole moment. In the presence of an external electric field, the molecules begin to polarize along the field direction and the dipole-dipole interactions between molecules begin to play an important role in collisions. In addition, depending on the orientation of dipoles, “head-to-tail” collisions between dipoles are attractive and “side-by-side” collisions are repulsive. The attractive (or the repulsive) interaction effectively lowers (or raises) the p -wave collisional barrier and subsequently enhances (or reduces) the chemical reaction rate for KRb-KRb. We explored this anisotropic nature of dipolar collisions by looking at both the inelastic loss and the corresponding temperature evolution of the molecular gas.

1.3 Dipole-Dipole Interaction

Going back to the motivations for ultracold polar molecules, in many applications, the specific chemical nature of molecules is not critical, and the essential ingredient is having a reasonable large permanent electric dipole moment. The dipole-dipole interaction, in SI units, has the form $\frac{\vec{d}_1 \cdot \vec{d}_2 - 3(\vec{d}_1 \cdot \hat{r})(\vec{d}_2 \cdot \hat{r})}{4\pi\epsilon_o r^3}$, where \vec{d}_1 and \vec{d}_2 are the two dipole moments, ϵ_o is the permittivity of vacuum, and \vec{r} is the separation between the two dipoles. The dipole-dipole interaction has two features that are very different from typical interactions between ultracold atoms. First, the dipole-dipole interaction falls off as $1/r^3$ and therefore has a long-range character. In contrast, the interparticle potentials between atoms and/or non-polar molecules can be adequately described as a “contact interaction,” which can to an excellent approximation be simply treated as a delta-function. Second, the dipole-dipole interaction is spatially anisotropic, and, as can be seen from the expression above, the interaction can be either attractive or repulsive depending on the orientation of the two dipoles with respect to the intermolecular vector, \vec{r} . In contrast, the interaction between atoms at ultracold temperatures is typically limited by finite angular momentum barriers to spatially isotropic s-wave interactions, i.e. where the relative orbital angular momentum is zero. This special property of polar molecules permits the experimentalists to control the relative spatial orientation, and thereby tune the intermolecular interaction with external electric fields.

Samples of ultracold gases with dipole-dipole interactions have been realized using chromium atoms in a Bose-Einstein condensate [32]. Chromium has an exceptionally large magnetic dipole moment of $6 \mu_b$, where μ_b is the Bohr magneton. In these pioneering experiments, the anisotropic character of the dipole-dipole interaction has been beautifully revealed [33, 34]. One of the key advantages of

polar molecules is that the electric dipolar interaction can be much stronger. For example, the interaction between two polar molecules with a typical electric dipole moment of order of a Debye, where $1 \text{ D} = 3.34 \cdot 10^{-30} \text{ C}\cdot\text{m}$, is approximately equal to the interaction between magnetic dipoles with a dipole moment of $100 \mu_b$. These much stronger interactions will in particular allow the long-range character ($1/r^3$) of the dipolar interaction to be manifested in experiments. This long-range nature of the dipole-dipole interaction is exploited in proposals aimed at realizing new types of many-body Hamiltonians and novel phases of matter with ultracold polar molecules. A review of theoretical work on this subject can be found in Ref. [10, 35].

To get a sense of the range of dipolar interactions, it is convenient to give a characteristic length scale, called the dipole length $l_D = Md^2/(4\pi\epsilon_0\hbar^2)$ [36], where M is the reduced mass, d is the dipole moment of the molecules, and \hbar is Planck's constant divided by 2π . The dipole length is essentially a measure of the intermolecular separation at which the dipole-dipole interaction energy equals the kinetic energy that corresponds to a de Broglie wavelength at that separation. To get appreciable long-range interactions in a gas of polar molecules, we want l_D to be comparable or greater than the average interparticle spacing. For atoms interacting via magnetic dipoles, this dipole length is typically on the order of a few tens of Bohr radii, a_0 , or less. For example, Rb with a magnetic dipole moment of $1 \mu_b$ has a dipole length of $l_D = 1 a_0 = 5 \cdot 10^{-11} \text{ m}$, while Cr with a magnetic dipole moment of $6 \mu_b$ has $l_D = 23 a_0$. This is more than 100-fold smaller than the mean interparticle distance even in ultracold atomic gas samples at the highest achievable densities (n) obtained thus far, for which $n^{-1/3} \approx 5000$ to $20000 a_0$. For polar molecules interacting via electric dipoles, however, this length scale can be as large as 10^4 to $10^6 a_0$, and therefore could be comparable to or even much larger than the interparticle spacing in an ultracold gas. For

example, KRb with a dipole moment of 0.566 D has a dipole length l_D of 6000 a_0 , while LiCs with a dipole moment of 5.5 D has l_D of $6 \cdot 10^5 a_0$. In addition, the complex internal structure of molecules offers unique possibilities for shielding and controlling molecular interactions by means of AC and DC electric fields [37].

Dipole-dipole interactions in an ultracold gas of polar molecules can include both two-body and many-body effects. Two-body effects are due to processes where one needs only consider two molecules interacting with each other in isolation. These include, for example, ultracold collisions and ultracold chemistry, where the fact that the gas is actually made up of many molecules simply enhances the observed total rate of these processes. In contrast, many-body effects are those that are not simply the sum of two-body processes. One example is the mean-field energy of a dipolar Bose-Einstein condensate [38]. In general, observing many-body effects will likely require a quantum degenerate sample of polar molecules, such as a Bose-Einstein condensate or a quantum degenerate Fermi gas.

1.3.1 Ultracold Collisions of Dipoles

Collisions in the ultracold regime have a number of novel features. With their low energies and long interaction times, ultracold collisions are sensitive probes of the interaction potential and can often be controlled with the application of modest external fields. In addition, the quantum statistics of the colliding particles, for example that of identical fermions or identical bosons, can play an important role. Molecular gases could introduce a new type of ultracold collision, namely chemically reactive collisions, and polar molecules offer the unique possibility for electric-field control of collisions. Understanding these two-body processes will be important for exploring many-body phenomena in ultracold gases of polar molecules.

For a given collision energy, interparticle collisions classically occur over a range of impact parameters with corresponding angular momentum barriers. For atoms, the ultracold temperature regime is often characterized by the requirement that collisions occur in only one angular momentum partial wave, namely the s-wave, the only one for which no centrifugal barrier exists. Similarly, for molecules at no external electric field when their dipoles have not yet been activated, the ultracold regime can be defined by requiring that only s-wave collisions occur. (Of course for indistinguishable fermions, s-wave collisions are not allowed.) This requirement means that collision energies in the gas should be much less than the height of the p-wave centrifugal barrier, which is, for example, $24\mu\text{K}$ [31] for KRb molecules. In the presence of an external electric field, however, the molecules will tend to polarize and the dipole-dipole interaction becomes important. This has the effect of mixing different angular momentum partial waves, and even though ultracold collisions may occur in a single scattering channel, that channel can no longer be simply described by a single partial wave.

The long-range nature of the interaction between polar molecules gives rise to a very different and fascinating temperature dependence of ultracold collisions for polar molecules compared to neutral atoms. The following discussion is summarized from the theoretical insights and results from Bohn *et al.* [36]. For species with a short-range potential (cf., delta function approximation for ultracold atom-atom potentials), the elastic collision cross section becomes a constant, independent of temperature in the ultracold regime. This threshold regime of temperature-independent elastic scattering cross section is a consequence when the range of the interaction is much smaller than the inverse scattering wavevector, $1/k$. Although this makes the theoretical description of the collisions really simple, the elastic cross section is also capped to a certain value. As discussed above, for dipole-dipole scattering, the range of the interaction can be characterized by

a dipole length, l_D . The threshold regime for scattering then occurs only when $l_D < 1/k$, which means that the relative kinetic energy of two colliding molecules is less than $E_D = \hbar^6(4\pi\epsilon_o)^2/(M^3d^4)$. Take KRb as an example (shown in Fig. 1.1), when fully polarized, this threshold regime corresponds to a temperature of order 80 nK. As the induced dipole moment of KRb decreases, hence the decrease of l_D , the temperature-independent elastic cross section also decreases. The long-range dipolar elastic collisional cross section in the threshold T -independent regime is proportional to the fourth power of the dipole moment ($\propto d^4$). One consequence is that because dipole length is large, the elastic cross section is huge. For fermionic KRb molecules, where dipolar collisions mixes odd partial waves, the cross section is $2 \cdot \frac{16\pi}{15} \cdot l_D^2 = 6.7 \cdot 10^{-8} \text{cm}^2 \cdot (\frac{d}{\text{Debye}})^4$. Another important consequence is that for temperatures higher than E_D/k_B (k_B is the Boltzmann constant), the elastic scattering cross section will be $\sigma = 8\pi l_D/(3k)$ and therefore increasing with decreasing temperature as $T^{-1/2}$. This corresponds to a temperature independent rate constant for elastic collisions of $k_{elastic} = \sigma v = 8\pi l_D \hbar/(3M)$, which for KRb with a dipole moment of 0.566 D would yield $k_{elastic} \approx 2.5 \cdot 10^{-9} \text{cm}^3/\text{s}$ independent of the temperature down to 80 nK. This means that KRb polar molecules at 80 nK are predicted to have elastic cross sections on the order of $\sigma \approx 5 \cdot 10^7 \text{Å}^2$, a scale much bigger than a typical size of a molecule!

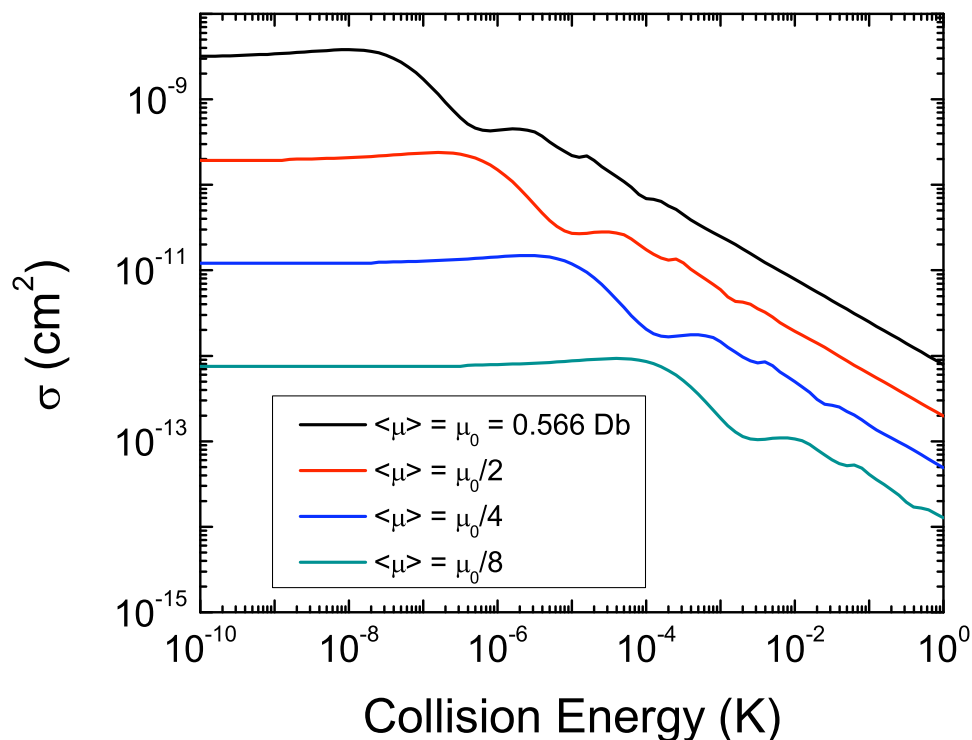


Figure 1.1: Universal elastic dipolar collision cross section v.s. collisional energy (for spin-polarized fermionic KRb polar molecules) with an induced dipole moment of 0.566 D, 0.283 D, 0.142 D, and 0.07 D [36]. The cross section shows two different regimes as a function of collisional energy (temperature). The cross section increases with decreasing temperature and reaches a threshold regime when the de Broglie wavelength is comparable or larger than the dipolar interaction length scale. In addition, the dipolar elastic cross section is orders of magnitude larger than a typical cross section for s-wave scattering of ultracold atoms.

Now, let us consider a question relevant to the experiments, namely what is the density required to observe elastic dipole-dipole collisions. To be experimentally sensitive to collisional effects, such as loss of trapped molecules for inelastic collisions or rethermalization of the gas for elastic collisions, requires that the typical time between collisions, given by one over the collision rate, is less than the interrogation time. Therefore, for a rough estimate, if we have a time of 1 s to observe a trapped sample of polar molecules with a dipole moment of 1 D, $k_{elastic} \approx 8 \cdot 10^{-9} \text{ cm}^3/\text{s}$ and this implies a minimum number density of about $n \approx 1.3 \cdot 10^8 \text{ cm}^{-3}$ is required to observe elastic dipole-dipole collisions. This is a general prediction for elastic collisions of polar molecules. For any specific experiment, other important considerations will include the effects of quantum statistics, contributions from the short-range part of the scattering potential, and the possibility of scattering resonances [5, 4], which can further increase these collision rates by orders of magnitude. Additionally, although the above discussion mainly focused on elastic processes, investigating inelastic collisions will be the crucial first step because it will determine the lifetime of trapped samples of polar molecules. In particular, chemically reactive collisions between polar molecules (or between polar molecules and atoms) represent an intriguing new frontier of encounters to be explored in the ultralow temperature regime. By detecting inelastic, or reactive, scattering through trap loss measurements, one can explore how these processes depend on temperature, electric field, quantum statistics, the internal state of the trapped molecules, and the geometry, or dimensionality, of the trapping potential. In summary, long-range interactions at this ultracold regime can determine the rates for short-range reactions.

1.3.2 Dipolar Quantum Gas

Ultracold gases can be used to realize interesting many-body quantum systems where the interactions between particles, along with particles' quantum statistics, govern the macroscopic behavior of the system. In an ultracold gas of polar molecules, the interparticle interactions are relatively strong, spatially anisotropic, and long-range. Proposals taking advantage of these interactions, here I listed only a limited number of examples, include studies of Bose-Einstein condensates or Fermi gases with dipolar interactions [10, 35], experimental realization of exotic condensed matter Hamiltonians with polar molecules confined in an optical lattice [12], architectures for manipulating quantum information [7, 8, 9], and creation of self-assembled dipolar crystals [39].

These proposals typically require molecules with large dipole moments in a gas with relatively high density (small inter-particle separation) and ultralow temperature. The highest densities and lowest temperatures are achieved for gases that are quantum degenerate. In particular, in a Bose-Einstein condensate of polar molecules, even a relatively small dipole moment is sufficient to realize a situation where the dipole-dipole interaction strength far exceeds the kinetic energy. More generally, the quantum degeneracy of a gas can be characterized by its phase-space density, $PSD = n\Lambda^3$ where n is the peak density and Λ is the thermal de Broglie wavelength. For a quantum degenerate gas, $PSD \geq 1$. For a given gas temperature and density, the size of the dipole moment sets the interaction strength and in general, one wants a larger dipole moment to more easily observe interaction effects. As an extreme example in the strongly interacting limit, it is predicted that a gas of polar molecules confined in a two-dimension pancake geometry can form a dipolar crystalline phase [39, 40]. For a gas density of 10^{12} cm^{-3} and molecular mass of about 100 amu (atomic mass unit), this crystalline

phase requires that the dipole moment be greater than 3 Debye [39].

1.4 Contents of this Thesis

Chapter 2 will present previous results from other groups and the challenges in trying to produce an ultracold gas of polar molecules. Chapter 3 will introduce some key aspects of the apparatus – the K-Rb machine and the Raman laser system. Chapter 4 covers the basics of the heteronuclear KRb Feshbach molecules that serve as the starting point for the state transfer that eventually makes polar molecules. Chapter 5 presents our understanding and mapping of the KRb electronic excited states that we use to transfer Feshbach molecules to deeply bound states. Chapter 6 discusses our demonstration of near-threshold state transfer using a two-photon Raman technique. We extend the technique for state transfer to the triplet rovibrational ground state in Chapter 7 and reach the absolute ro-vibronic ground state in Chapter 8. In Chapter 9, a general scheme of molecular hyperfine state manipulation is presented. With full control of the internal state quantum numbers of polar molecules, we study their collisions with atoms, indistinguishable molecules, and distinguishable molecules in Chapter 10. In Chapter 11, we study molecular dipolar collisions by tuning of an external electric field. Finally, Chapter 12 summarizes the thesis and gives an outlook for future directions.

Chapter 2

Challenges for Making Ultracold Polar Molecules

2.1 Introduction

Molecules are intriguing systems where their internal energy levels, which include hyperfine, rotational, vibrational, and electronic levels, span a large spectrum ranging from kHz to hundreds of THz. However, because of this complex level structure, cooling molecules, both in their translational motion and their internal states, is difficult. Experimental efforts aimed at producing cold or ultracold polar molecules generally follow one of two different approaches: one is to directly cool molecules to an ultralow temperature; the other is to start from ultracold atoms, and then associate them into tightly bound molecules. Taking examples from different cooling methods, I have summarized previous progress and the result from this thesis (the last row) in Table 1.

Method	Dipole (D)	T	Trapped Density	PSD	Ref
buffer gas cooling	NH (1.39)	550 mK	10^8 cm^{-3}	10^{-14}	[19]
stark deceleration	OH (1.67)	50 mK	$10^6\text{-}10^7 \text{ cm}^{-3}$	10^{-13}	[20, 21]
photo-association	RbCs (1.3)	100 μK	10^4 cm^{-3}	10^{-14}	[22]
coherent transfer	KRb (0.574)	160 nK	10^{12} cm^{-3}	0.06	this thesis

Table 2.1: Summary of experimental results for production of cold and ultracold polar molecules. Selected examples of the molecule species with its electric dipole moment (calculated or measured) and the achieved gas temperature, trapped number density, and phase-space density are given. (The photo-association result was for an untrapped sample of molecules.)

2.2 Direct Cooling of Molecules

The most straightforward approach for producing ultracold polar molecules would simply be to directly cool them to ultralow temperatures, just as is done for ultracold atomic gases. However, the powerful technique of laser cooling [41, 42, 43], which launched experimental investigation of ultracold atomic gases, is much more challenging for molecules due to complex internal state structures. The basic issue is that achieving low temperature necessitates momentum recoil accumulated from thousands to millions of excitation and spontaneously emitted photons. This in turn requires efficient cycling in a “closed” 2 or 3 level system, which is generally not feasible in electronic excitation of molecules. Recently, laser cooling of molecules via coherent scattering inside high-finesse optical cavities has been proposed [44, 8, 45, 46], but a necessary ingredient for successful implementation is an initial sample of cold molecules with a sufficiently high density to enable collective effects [46]. Free space laser cooling has also been proposed [47], including the possibility of constructing a general purpose magneto-optic trap for a certain class of polar molecules [48].

Many general molecule cooling techniques developed over the last 10 years have proved to be very successful in producing a diverse set of cold polar molecules, including but not limited to CaH, CaF, OH, NH₃, ND₃, H₂CO, NH, PbO, and YbF. These so-called “direct cooling” techniques include imbedding and cooling molecules in a cryogenically cooled helium buffer gas [49, 19, 50], slowing molecules from a supersonic jet through Stark deceleration [51, 21], magnetic [52, 53] or optical deceleration [54], velocity filtering of a molecular beam [55], production of cold molecules via kinematic collisions [56], or backward motion of a molecular beam source nozzle [57]. Direct cooling of polar molecule gases provides access to temperatures in the range of 10’s to 100’s of mK, which is sufficiently cold to allow

molecules to be confined in electro-static [20], AC electric field [58], and magnetic traps [59, 19]. These cold species can be used for precision measurements [3], collisional studies [60, 21, 61], and cold chemistry [6, 62]. To further reduce the molecular temperature, methods such as the proposed laser cooling approaches discussed above, cooling via evaporation, or sympathetic cooling with ultracold atoms might prove to be viable. Two preconditions for their success will be i) a favorable ratio of elastic and inelastic collisions and ii) a sufficiently dense sample of molecules accumulated inside a trap. With further improvements that permit lower temperatures and higher trapped gas densities, it looks promising for dipole-dependent cold collision dynamics in directly cooled polar molecule gases to be accessible for study in the near future.

2.3 Photo-association

An alternative to directly cooling polar molecules is to start from ultracold atoms and convert them pairwise into deeply bound molecules. This takes advantage of the fact that atoms can be laser cooled to temperatures of $100 \mu\text{K}$ or below. However, the challenge here is to efficiently bring the atoms together to form tightly bound molecules while avoiding any heating of the gas due to the release of the binding energy, which usually corresponds to a temperature of a few thousand Kelvins (Fig. 2.1). Heating in general means that many energy states are populated, including both external and internal states.

One way to accomplish this is photo-association [63], where one uses light to drive a transition between a scattering state of two atoms and an electronically excited molecular state. The electronically excited molecules then quickly decay by spontaneous emission to electronic ground-state molecules. The advantage of this incoherent optical process, as opposed to collisional formation of molecules, is that the binding energy is removed in the energy difference between the absorbed

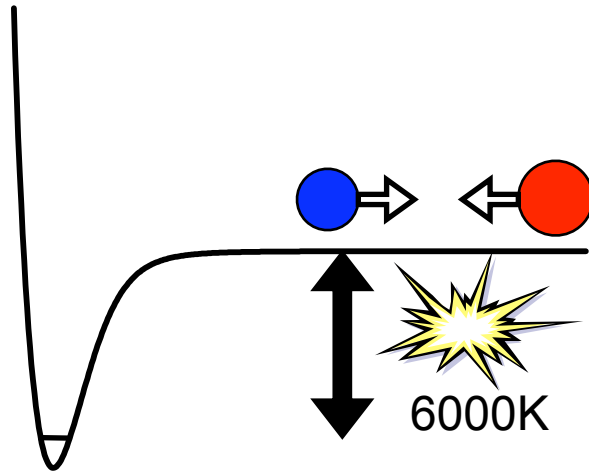


Figure 2.1: Forming ultracold molecules from ultracold atoms is challenging because a large binding energy is released when two atoms form a tightly bound molecule. For example, the binding energy of the ro-vibronic ground-state KRb molecules equals to a temperature of 6000K (4000 cm^{-1}), which is 10^{10} times larger than a typical temperature of an ultracold atom gas.

and emitted photons rather than being released as kinetic energy that heats the ultracold gas. In photo-association, ideally only a small amount of heating of molecular external motion remains due to the recoil of the molecule as it emits a photon in its spontaneous decay; this heating typically corresponds to a few hundreds of nano-Kelvin. However, typically many internal states are populated at the end of a photo-association process.

Use of photo-association to make ultracold polar molecules in their rotational, vibrational, and electronic ground state was first demonstrated by Sage *et al.* [22]. In their experiment, optical fields were applied to transfer Rb and Cs atoms in a continuum of scattering states to the absolute ground state of the RbCs molecule using the two steps illustrated in Fig. 2.2. A two-step process was necessary because of the extremely small wavefunction overlap between two free atoms and a tightly bound molecule. For example, even at a density of 10^{12} cm^{-3} ,

which is a couple orders of magnitude higher than that of laser-cooled atom gases, the typical distance between two atoms is $20,000 a_0$. In contrast, a tightly bound diatomic molecule has an internuclear separation of $10 a_0$ or less.

The first step used by Sage *et al.* was photo-association followed by spontaneous decay to produce large, weakly bound electronic ground-state molecules in high vibrational (high- v) states. In the spontaneous decay, many high- v levels of the triplet ground state were populated, with the biggest branching ratio being 7% into $v = 37$ [22]. The second step was then to apply two laser fields for a pump-dump transfer process using absorption and stimulated emission. This step transferred molecules in the $v = 37$ of the triplet ground-state to $v = 0$ of the singlet ground-state through an intermediate electronic excited state.

This photo-association technique produced absolute ground-state molecules that were at the ultracold temperature of $100 \mu\text{K}$ in their translational motion. However, the creation process was inefficient. In this proof-of-principle experiment, each laser pulse sequence only produced 10 absolute ground-state molecules from the initial 10^8 atoms. In addition, molecules in many other higher energy vibrational and rotational levels were produced at the same time. Nevertheless, this experiment highlights the general scheme as well as the challenges in converting ultracold atoms into tightly bound molecules. Other experiments have used photo-association of laser-cooled atoms to create ultracold polar molecules in alkali systems such as KRb [64, 65], NaCs [66], and LiCs [67].

To make this incoherent process more efficient in the production of deeply bound ground-state molecules, one obviously desires to have an enhanced coupling strength from the initial scattering atom state to a suitable excited molecular state as well as an increased Franck-Condon factor from that excited molecular state to a deeply bound vibrational level in the electronic ground potential. An enhanced phase-space density of the initial atomic gas can dramatically enhance

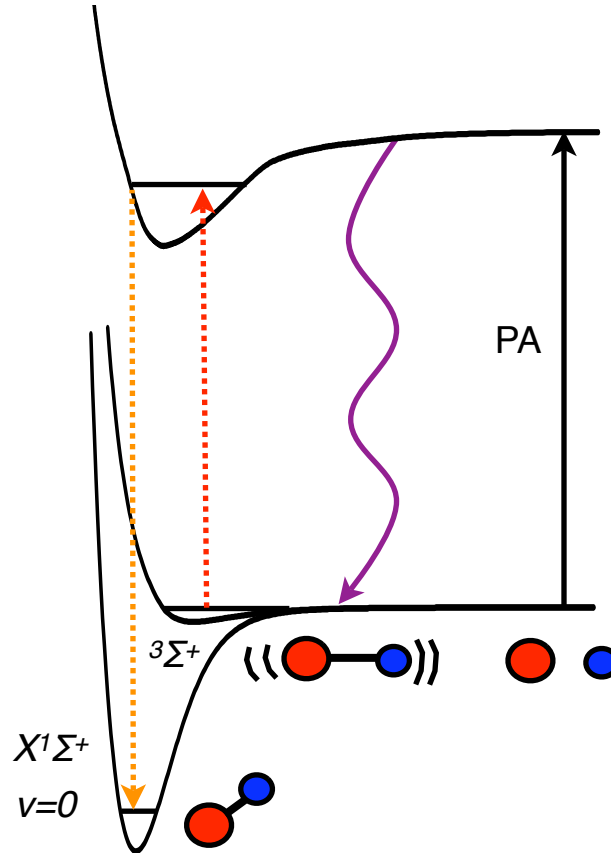


Figure 2.2: Schematic of a two-step optical transfer process described in Sage *et al.*[22] that produced RbCs in the absolute ground state from laser-cooled Rb and Cs atoms. The first step is to create weakly bound molecules (in high vibrational levels) by photo-associating (PA) atoms into excited-state molecules that then decay back to the ground electronic state by spontaneous emission (wiggly line). These weakly bound molecules provide a better wavefunction overlap for the second transfer to the absolute ground state. The second step is to use a stimulated emission pump-dump process (dashed arrows), to enhance optical transfer from weakly bound molecules to the absolute ground state. Typically this process created 10 molecules in the absolute ground state when starting from 10^8 atoms in a single two-step transfer.

the transition rate for the first step. But optimization of the overall efficiency is limited by the molecular structure. Furthermore, this incoherent process will not be able to produce molecules populating only a single target state. Techniques and proposals have emerged to enhanced the transition strengths using accidental resonances between molecular states, either in the excited electronic potentials [68, 69] or in the ground potential [70]. A recent proposal suggests that simply performing photo-association of atoms near a Fano-Feshbach resonance is sufficient to drive them into a deeply bound molecular state either through one-photon or two-photon transitions [71, 72]. Although resonant-assisted photo-association enhances the transition by orders of magnitude, the overall transition rate is still rather weak. Using either one-photon or two-photon processes to efficiently drive atoms to a deeply bound state still appears challenging. An additional issue with this approach is that the initial state is a scattering state (unless the initial atomic gas is quantum degenerate), and the time scale for two atoms to come close enough to be photo-associated, which can be of order a few ms, can effectively limit the transition Rabi frequency.

2.4 Fully Coherent Scheme

One extremely powerful solution to all the challenges outlined above is to use a transfer process that is fully coherent and therefore even reversible. In particular, we can replace each incoherent step of the photo-association method by a coherent transfer step. The advantages of a fully coherent method are i) it is adiabatic, and therefore results in no heating and ii) it is *single* target-state selective, therefore the process can be much more efficient. However, to avoid strong transfer field to induce non-linear effect, one or two coherent steps may not be sufficient to pair atoms together and transfer them to the absolute rovibrational molecular ground state. In that case, a general solution is to use a

carefully designed train of coherent pulses that can achieve a complete population transfer to a single target state via coherent accumulation of small population for each pulse [73]. But it turns out that for KRb, and this should also be true for other heteronuclear bi-alkali molecules in general, one can find a *single* excited electronic state that has relatively strong transition strengths and makes a single- or two-step transfer possible.

In the following chapters, I will describe in detail the complete scheme of the fully coherent method that we use to produce a near quantum degenerate gas of ultracold polar molecules in their ro-vibronic ground state [15]. Here I provide a quick summary. As opposed to a typical photo-association experiment discussed in the previous section, we start with an ultracold atomic gas at a high phase-space density. This high phase-space density is achieved using the now standard techniques of laser cooling followed by forced evaporation [74, 75]. At the end of the evaporation, we have a quantum degenerate gas of K and Rb atoms, each in a single hyperfine state, at a temperature of several hundred nK. The atoms are confined in a far-detuned optical dipole trap, which can also confine the resulting KRb molecules.

We then use two coherent steps for production of ultracold polar molecules. First, we use a magnetic-field tunable Fano-Feshbach resonance, to convert atoms pairwise into molecules. (Strictly speaking, this step is not fully coherent because the initial state is a thermal ensemble and there is loss during the conversion.) Secondly, these extremely weakly bound molecules are then optically transferred into the ro-vibronic ground state using a two-photon coherent process. The basic approach of making molecules near a Fano-Feshbach resonance and then using coherent optical manipulation of the molecules' internal state has also been used to produce ultracold gases of homonuclear (i.e., non-polar) molecules [30, 29]. In the next chapters, I will discuss in more detail the two steps in this transfer that

makes it possible to map the high phase-space density of an ultracold atomic gas into tightly bound polar molecules in the ultracold regime.

Chapter 3

Apparatus

The main workhorse of the experiments presented in this thesis has two parts, the atoms/molecules machine and a spectroscopy/Raman laser system.

3.1 K-Rb Machine

The detail of the hardware and the software features of the K-Rb machine can be found in J. Zirbel's thesis [18]. Here I will briefly discuss the methods that we use to prepare ultracold gas of ^{40}K and ^{87}Rb atoms, and describe a few specific additions to the apparatus since Zirbel's thesis.

The first step of our experiment is to prepare an ultracold mixture of K and Rb atoms. To do this, we start by trapping and cooling K and Rb simultaneously in a dual-species magneto-optical trap (MOT). We typically have K atom number $N_K = 1 \cdot 10^7$ (w/o the presence of the Rb MOT) and Rb atom number $N_{Rb} = 2 - 4 \cdot 10^9$ in the MOT. The MOT loading time is on the order of 5 s. We then physically move atoms through a 0.7-m transfer region to a differentially pumped higher vacuum region of the chamber. The transfer efficiency is 10-20%. The atoms are then loading into a standard Ioffe-Pritchard (IP) magnetic trap. At this stage, we perform forced evaporative cooling on Rb by driving hot Rb atoms from the $|F = 2, m_F = 2\rangle$ state to the untrapped $|1, 1\rangle$ state. At the same time, the K atoms gas is sympathetically cooled by thermal contact with the directly

cooled Rb gas. The K atoms are in the $|9/2, 9/2\rangle$ state. Here, F denotes the total atomic spin and m_F is the spin projection along the magnetic-field direction. We also remove any Rb atoms in the $|2, 1\rangle$ state to prevent trap loss due to collisions with K atoms in the $|9/2, 9/2\rangle$ state. At the end of the IP trap evaporation, we typically have $2 - 3 \cdot 10^6$ Rb atoms and $6 - 7 \cdot 10^5$ K atoms at $1 \mu\text{K}$. This gas mixture is then transferred into an optical dipole trap (OT). (The system is capable of having up to $5 \cdot 10^6$ Rb atoms in the presence of the same number of K atoms simply by increasing Rb MOT laser power (and hence the Rb MOT number), but we found that in the later stages, higher Rb number limits the K number.)

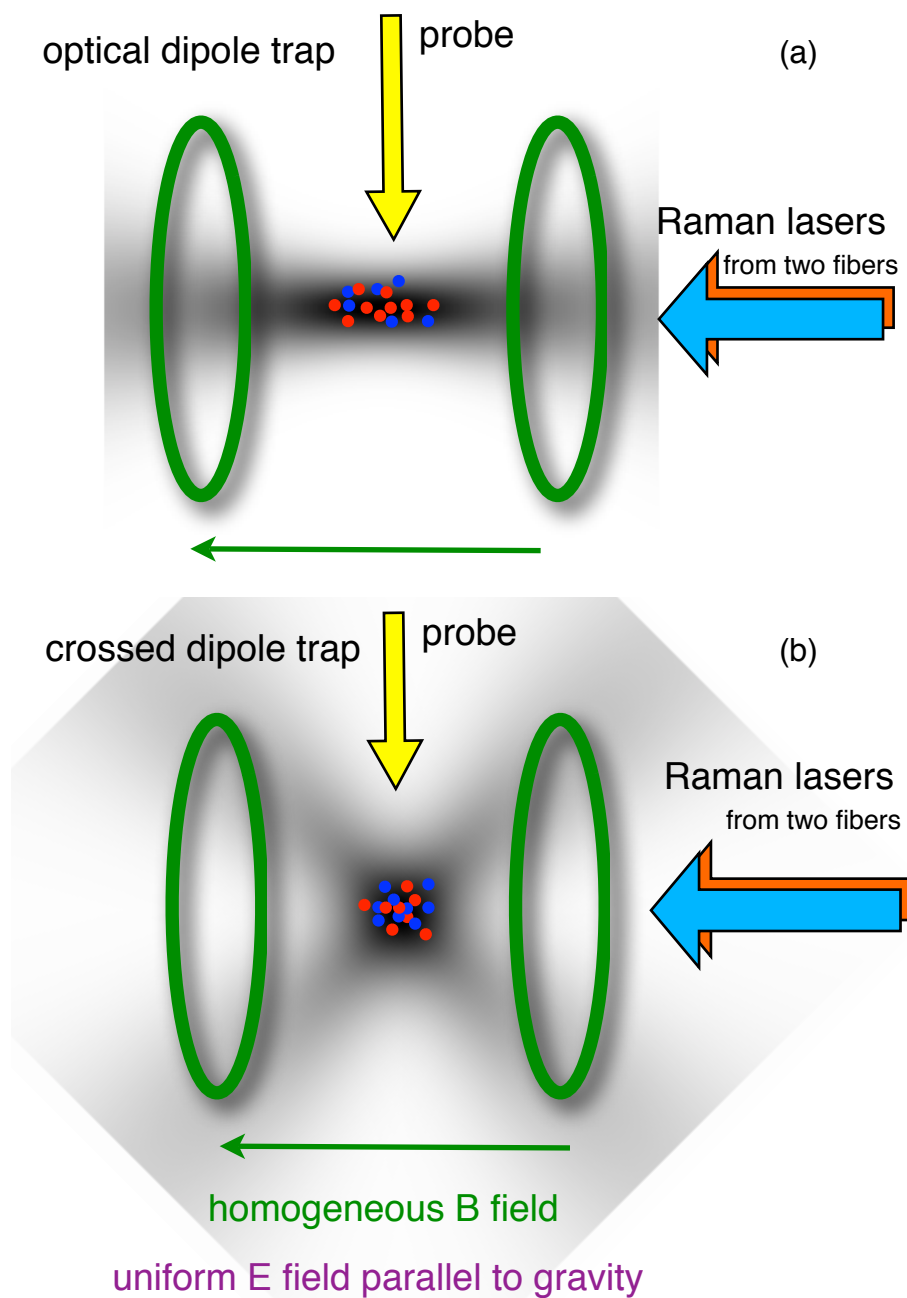
For our experiments aimed at making ro-vibronic ground-state molecules, we used a *single-beam* optical dipole trap with a waist of $40 \mu\text{m}$ (Fig. 3.1(a)). The trap laser beam was derived from either a 1064 nm single frequency fiber laser or a 1090 nm multi-mode fiber laser. After loading atoms in the optical trap, we transfer the K and Rb atoms into their respective lowest hyperfine states, K in $|9/2, -9/2\rangle$ and Rb in $|1, 1\rangle$, at a magnetic field of 31.29 G. The transfer uses adiabatic rapid passage by a frequency swept rf and microwave fields. We then increase the magnetic field to 532.30 G for further evaporation before ramping the field close to 546 G for Feshbach molecule creation. Evaporation in the optical trap is accomplished by lowering the laser power to cool the gas to a few hundreds of nanoKelvins. In the later experiments (Chapter 10 and 11), we changed our dipole trap to a crossed beam geometry with two intersecting elliptical-shaped beams (Fig. 3.1(b)). Each beam has a waist of $40 \mu\text{m} \times 200 \mu\text{m}$. (When using the crossed beam optical dipole trap, we also shape our Raman laser beam to be elliptical. The 690 nm Raman laser is focused to a waist of $38.5 \mu\text{m} \times 205 \mu\text{m}$, and the 970 nm Raman laser is focused to $43.5 \mu\text{m} \times 205 \mu\text{m}$ waist.) A summary of our operating condition is given in Table. 3.1.

Finally, I wish to mention that we were able to shorten the experimental

	MOT	IP # and Temp.	OT # and Temp
Rb atoms	$2 - 4 \cdot 10^9$	$2 - 3 \cdot 10^6$ at $1 \mu\text{K}$	$3 \cdot 10^5$ at 300 nK
K atoms	$1 \cdot 10^7$ (w/o Rb)	$6 - 7 \cdot 10^5$ at $1 \mu\text{K}$	$3 \cdot 10^5$ at 300 nK
Feshbach Molecules			$3 - 5 \cdot 10^4$ (Ch. 4)

Table 3.1: A benchmark of experimental operating condition.

cycle time by a factor of 2 since Zirbel's thesis: the evaporation time in the IP trap was shorten from 60 s to 35 s and the evaporation time in the OT went from 40 s to 3-4 s. The significant reduction of OT evaporation time was accomplished simply by aligning the trap so that the beam had a smaller tilt away from being perpendicular to the direction of gravity. This also improved our atom and Feshbach molecule numbers in the OT by a factor of 2 or 3.



Top View (gravity direction into the page)

Figure 3.1: Top view of a simplified layout of our experiment (a) using a single beam optical dipole trap and (b) using a crossed beam dipole trap. In both configurations, a uniform magnetic field is provided by a pair of Helmholtz coils. The Raman laser beams for molecular internal state manipulation co-propagate along the magnetic-field direction. The imaging beam or “probe” is perpendicular to the magnetic-field direction. Gravity in this picture points into the page.

3.2 Electric-field Plates

One new addition to the apparatus was a pair of electric-field plates. Because these were incorporated after the main apparatus was built, the plates were constrained to be located outside of our glass-cell (“science cell”) vacuum chamber (Fig. 3.2).

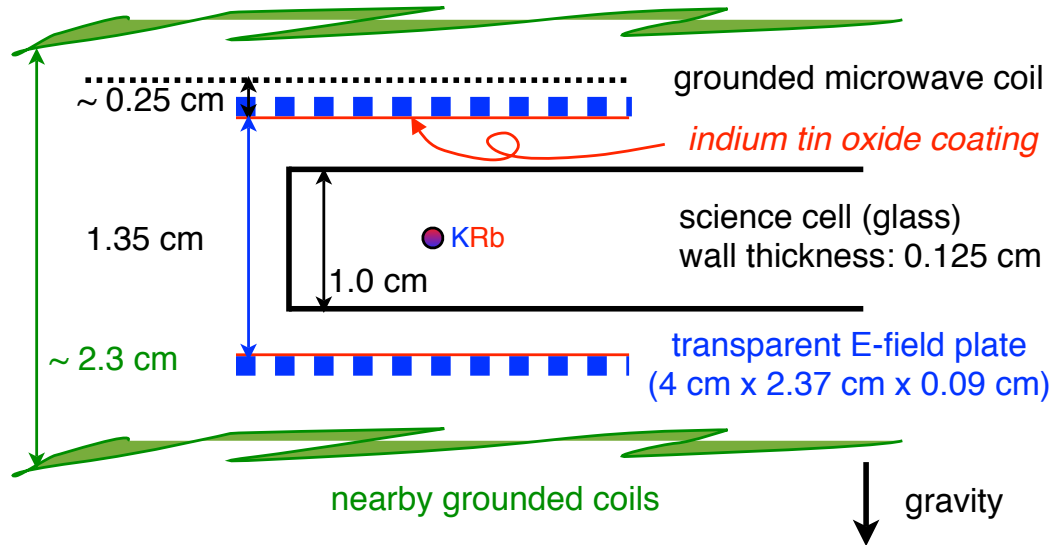


Figure 3.2: Schematic cross-section view of the apparatus near the “science cell” (not drawn to scale). One anti-gravity coil and an rf coil are left out from the drawing.

The E-field plates are cut from #CH-50IN-S209 transparent plates with indium tin oxide coating purchased from Delta Technologies. The plates transmit 80-90% of light in the wavelength range of 600 nm to 1100 nm. (Plates with 5-10% better transmission properties are also available from the same company now.) The plates are 4.0 cm long, 2.37 cm wide, and 0.09 cm thick and the inner walls are separated by 1.35 ± 0.02 cm with a phenolic holder. The coating surfaces face each other. The pair of plates fits around our glass cell, which comes from Starna Cells and is made out of Borofloat (a type of pyrex glass with dielectric

constant ~ 4.8) with a single wall thickness of 0.125 cm. The E-field at the position of “our molecules” is calculated from the geometry and the applied voltages on the plates in addition to considering the glass walls as dielectric material between the plates. For an applied voltage difference of 1V across the plates, the corresponding uniform E-field between plates pointing along the gravity direction is

$$\frac{1\text{V}}{1.35\text{ cm}} \cdot \frac{1.35\text{ cm}}{1.35\text{ cm} - 2 \cdot 0.125\text{cm} + 2 \cdot 0.125\text{cm}/4.8} = 0.868 \frac{\text{V}}{\text{cm}}. \quad (3.1)$$

This calculated field has an uncertainty from the measured separation between plates (1.5%), the dielectric constant of the glass material (1%), the thickness of the glass wall (unknown), and the fringe field that came from the finite size of the plates (0.7%). Together, we estimated the total uncertainty of the calculated field to be 3-5%. This does not include possible free floating electrons or patch charges. So far, we do not have an independent way of calibrating the electric field.

Obviously, the biggest concern with placing the plates outside the vacuum chamber is that dielectric breakdown can occur at a relatively low applied voltage. (The air breakdown field is 30 kV/cm.) Therefore, we tried to insulate surrounding metal by covering them with many layers of Kapton tape. One of the closest metal planes is a microwave coil that is laid out on a copper circuit board and is only 0.16 cm from the E-field plate surface and 0.25 cm from the E-field coating surface where the voltage is applied (Fig. 3.2). With 3 - 5 layers of Kapton tapes, we only saw immediate discharge between the microwave coil and the E-field plate above ~ 6 kV applied voltage difference. We also tested the breakdown voltage by putting a grounded wire wrapped in 2 layers of Kapton tape *directly* on the coating surface, which is essentially a test of the breakdown of the Kapton tape. For this test, we saw discharge happened at ~ 4 kV. (This wire is the same as what we used for the magnetic-field coils that surround the E-field plates.) In addition,

we have also tested the plates with a mocked up glass cell in between. For our system, we are confident that we can apply up to 10 kV (+5 kV on one plate and -5kV on the other) across the field plates before any breakdown happens. This corresponds to an electric field of ~ 9 kV/cm.

However, we run into another limit before the dielectric breakdown occurs. Namely, when the electric field is turned up too high, we saw our glass cell (perhaps) being polarized and does not relax after the field is off. This usually happens at an applied voltage of 6.0 kV (5.2 kV/cm) and was seen using sensitive Stark spectroscopy on KRb (Chapter 8.3).

3.3 Molecular Spectroscopy Lasers

To manipulate molecular internal ro-vibronic states, we used many different tunable lasers to map out relevant electronic excited states and ground states of $^{40}\text{K}^{87}\text{Rb}$. These lasers include a home-built tunable Ti:sapphire (Ti-Sa) laser, an ELS VersaDisk tunable around 1030 nm, and home-built diode lasers in either Littman or Littrow configurations at various wavelengths.

3.3.1 Widely Tunable Ti:sapphire Laser

A widely tunable *cw* Ti-Sa laser is ideal for performing molecular spectroscopy in the wavelength range that is relevant for finding suitable intermediate states to bridge the large wavefunction mismatch between Feshbach molecules and any desired deeply bound state. The laser we use was built by Lisheng Chen before/during the same time when we were building the K-Rb machine. An excellent discussion of the layout of our Ti-Sa laser and the elements for large and stable frequency tuning can be found in Chapter 2.2 of Chen's thesis [76]. Since Lisheng had already graduated by the time we started to work with the Ti-Sa, it was postdoc Avi Pe'er who revived the Ti-Sa laser and helped to incorporate it

into our experiment.

The wavelength tuning range of the Ti-Sa is mostly set by the cavity mirrors and the normal lasing wavelength of a Ti-Sa crystal. We first used the Ti-Sa laser to scan for KRb^* states near the Rb D1 line (~ 795 nm). For this purpose, we used a set of mirrors with coating that allows a tuning range from 730 nm to 850 nm. The wavelength is tuned using optical elements in the cavity, including a thick etalon, a thin etalon, and a birefringent filter (see Chen’s thesis [76]). In this wavelength range, the Ti-Sa laser is offset-locked to a temperature stabilized Fabry-Perot cavity that has a mode spacing of 250 MHz. The Ti-Sa linewidth is < 20 kHz and the absolute long-term frequency stability is better than 2 MHz.

We later changed the mirrors inside the cavity such that the Ti-Sa was lasing near $1 \mu\text{m}$ with a tuning range of ± 50 nm. This change is ideal for the search of one-photon transitions from Feshbach molecules to KRb^* states in the excited potential $2^3\Sigma^+$. For this wavelength range, we directly lock the Ti-Sa laser to the Ti-Sa frequency comb (see discussion below).

3.3.2 Diode Lasers

We use numerous home-built external cavity diode lasers in the Littrow configuration for our K-Rb machine; these use non-AR-coated diodes from Hitachi and Sharp. But for molecular spectroscopy, we use AR-coated (coated either in JILA or commercially from Eagleyard) diode lasers mostly in the Littman configuration. This configuration, although it usually gives less available laser power, has the advantage that the output does not steer within a large frequency tuning range. For our current setup, we manipulate the internal states of KRb using a pair of diode lasers in the Littman configuration as our “Raman lasers.”

3.3.3 Ti:sapphire Comb

A stable optical frequency comb is crucial in maintaining a well-defined phase relation between our Raman lasers, which are very different in frequency. The basics of state-of-the-art frequency combs can be found in many JILA theses, e.g. [77]. The purpose of this section is only to describe how we incorporate the comb into our system and perform some basic diagnostics and characterizations. More detail will be available in the next thesis from our project by Marcio Miranda, who has been the main person responsible for operating and maintaining the comb.

In our experiment, we use a home-built Ti-Sa frequency comb. When the Ti-Sa is mode-locking, the laser output from the cavity is a train of pulses that are equally spaced in time. The operating condition for the laser is measured to have 650 - 750 mW time-averaged laser power and a spectrum centered around 800 nm with a full width half max (FWHM) of ~ 30 nm (Fig. 3.3). Directly out of the laser cavity, we then broaden the spectrum (shown in Fig. 3.4) using a non-linear supercontinuum fiber (Crystal Fibre FemtoWHITE 800) with a coupling efficiency of $\sim 30\%$. This broadened spectrum conveniently covers the wavelengths we are interested in with a certain spectral holes that can be avoided with compromises among all the wavelengths of interest. This is accomplished by fine adjustments of the alignment and the polarization into the non-linear fiber.

The comb serves as a frequency ruler in the optical domain. Our comb is precisely stabilized in the following way: The repetition rate, $f_{rep} \approx 756$ MHz, determined by the comb cavity length is maintained by referencing one comb tooth to a stable 1064 nm Nd:YAG. The Nd:YAG (linewidth < 1 kHz) is locked to a stable cavity in Jan Hall's lab. The error signal from f_{rep} is feedback to the PZT of a cavity mirror to actively adjust the comb cavity length. The comb offset

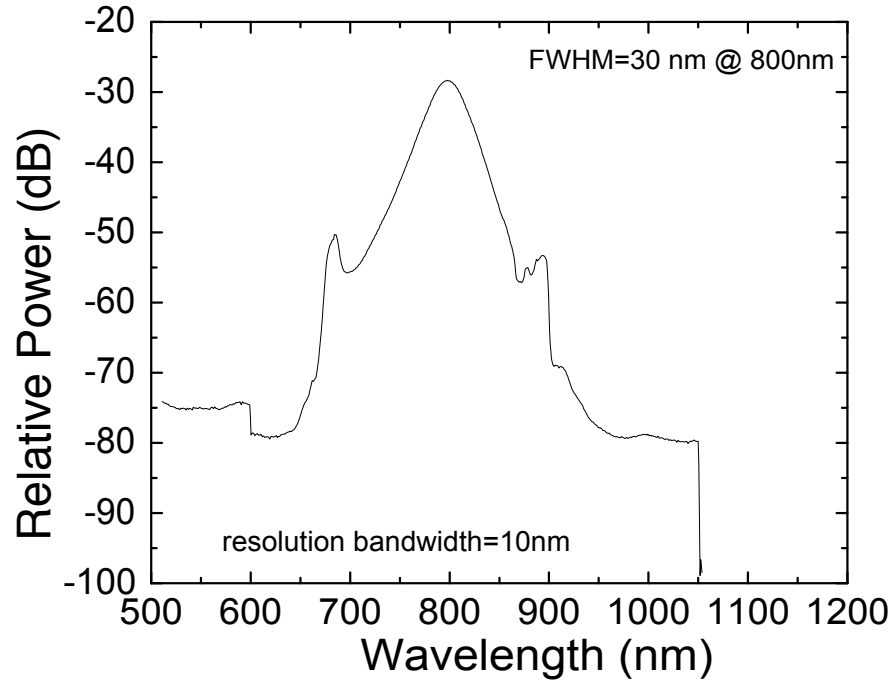


Figure 3.3: Ti-Sa comb spectrum, measured directly out of the comb cavity. The time-averaged power of the laser is ~ 700 mW. The laser spectrum centered at 800 nm with a full width half max of 30 nm.

frequency f_{co} , which can be tuned by the pump laser power into the cavity, is usually around 50-300 MHz. The f_{co} beat is derived from beating the 532 nm part of the comb spectrum and the doubling of the 1064 nm part of the spectrum, in a so-called self-referencing configuration. The f_{co} is then locked to a stable rf source that is in turn referenced to a 10 MHz commercial quartz clock (Wenzel Associates). The error signal of f_{co} is feedback to an acoustic-optical modulator to actively adjust the pump power into the cavity.

3.3.4 Phase Locking

As I have mentioned earlier, maintaining the phase coherence of the Raman lasers is crucial for coherent transfer molecules between internal states. Therefore, we have to insure the two Raman lasers to not only maintaining their frequencies,

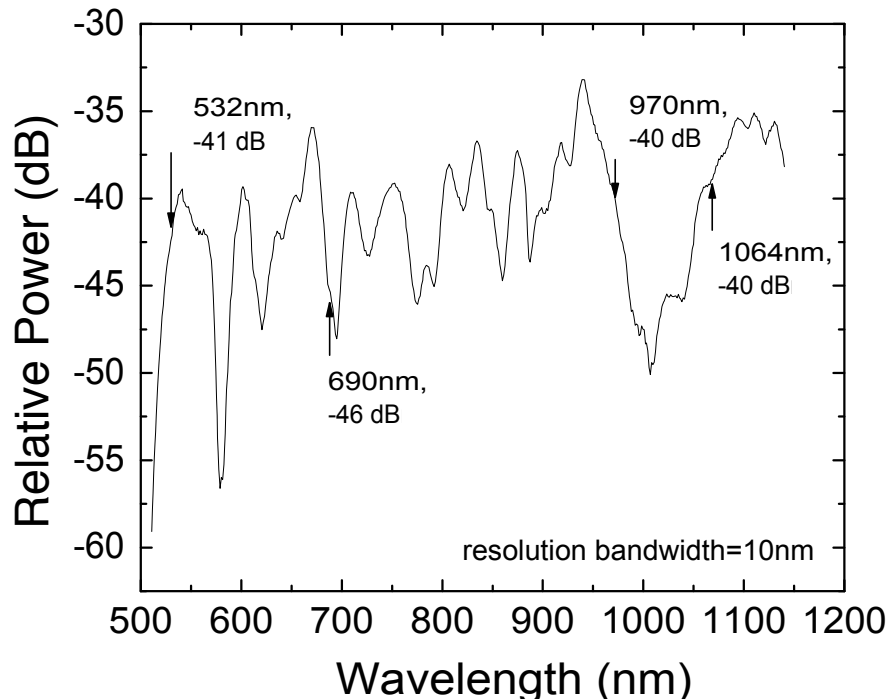


Figure 3.4: Full spectrum of the frequency comb in our system after broadened through a non-linear supercontinuum fiber. Operating with this spectrum, we typically get Raman laser (690 nm and 970 nm) beats, YAG (1064 nm) beat, and f_{co} (532 nm and doubling of 1064 nm) on the order of 30 - 35 dB (100 kHz bandwidth) from the noise floor.

but also have a definite and predictable phase evolution throughout the duration of the transfer. Our coherent transfer manipulation usually takes a few μs , therefore the relative laser linewidth has to be on the order of 10 kHz for the transfer (that uses a few MHz Rabi frequency coupling) to be efficient. The phase coherence of the Raman lasers are maintained through phase-locking (with current feedback of Raman laser diodes) to our stable frequency comb. In our setup, most of the laser power from the Raman laser system is directly sent to our vacuum chamber for molecular internal state manipulation. We do not send the comb light to the molecules (Fig. 3.5). The complete electronics of the locking configuration is shown in Fig. 3.6.

From an operational point of view, our locking procedure is the following. To

lock a Raman laser at a desired frequency, we first check the laser frequency on a wavemeter (Bristol Instrument 621 series). The wavemeter is internally frequency referenced to a HeNe laser. We found that the long-term drift of our wavemeter is < 30 MHz and the short-term stability is $\sim \pm 5$ MHz. The absolute frequency of our wavemeter reading as compared to the frequency referenced to a well-characterized comb is usually about 30-50 MHz too high. Since our comb has a repetition frequency that is relatively high at ~ 756 MHz, our 10 MHz wavemeter stability is more than sufficient for us to determine the closest comb tooth that our laser beats with. Knowing the closest comb tooth's absolute frequency (from f_{rep} and f_{co}) allows us to lock our laser to a desired frequency by setting the specific comb-to-diode beat using a synthesizer (Fig. 3.6). The diode laser frequency is coarsely tuned by a piezoelectric transducer controlling the grating laser feedback and is finely tuned by the diode current feedback.

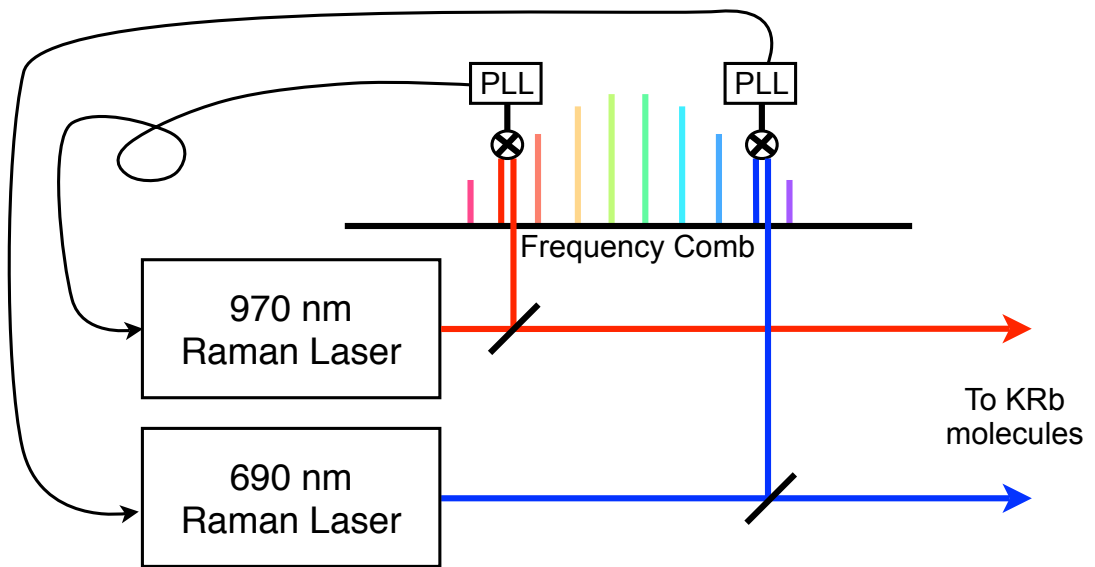


Figure 3.5: Our Raman lasers, which we use to manipulate molecular internal states, are phase-locked to a stable frequency comb. PLL stands for phase-lock loop.

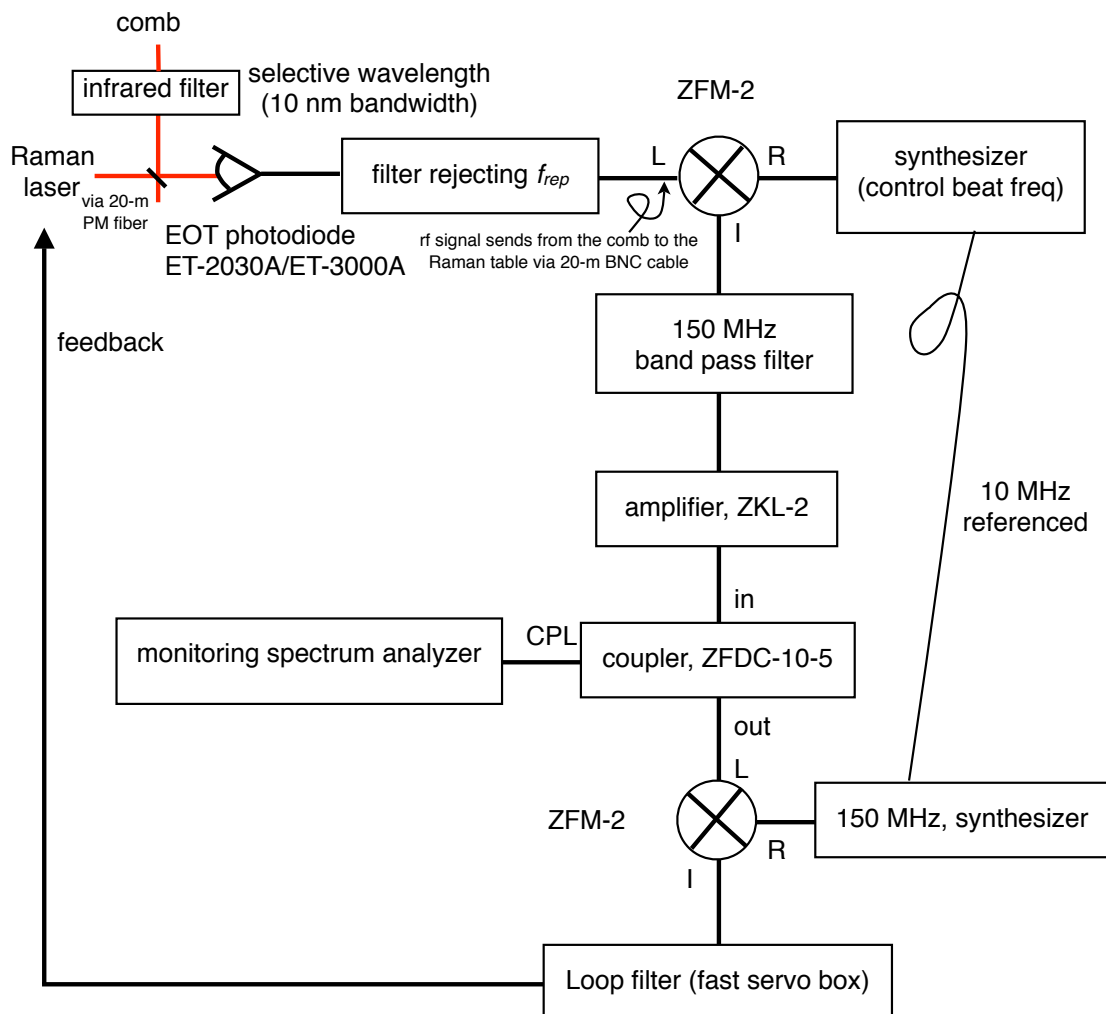


Figure 3.6: Layout of our Raman laser phase lock electronics. Rf components are labelled by MiniCircuits part numbers.

Our coherent transfer manipulation of molecular internal states requires time-varying couplings between internal states. These are accomplished by intensity ramp of the Raman lasers. To control the laser intensity (shown in 3.7), we send the laser through an acousto-optic modulator (AOM). We use the -1 diffracted order of the beam and control the rf power that goes into the AOM in the following way: We first directly program our desired intensity ramps (usually linear ramps) into an arbitrary waveform generator. The generator gives a dc voltage signal and is then mixed with an rf frequency source of 98.5 MHz before the mixed rf signal is amplified and sent to drive the AOM. This varying rf power directly control the intensity of the Raman laser that is seen by our molecules.

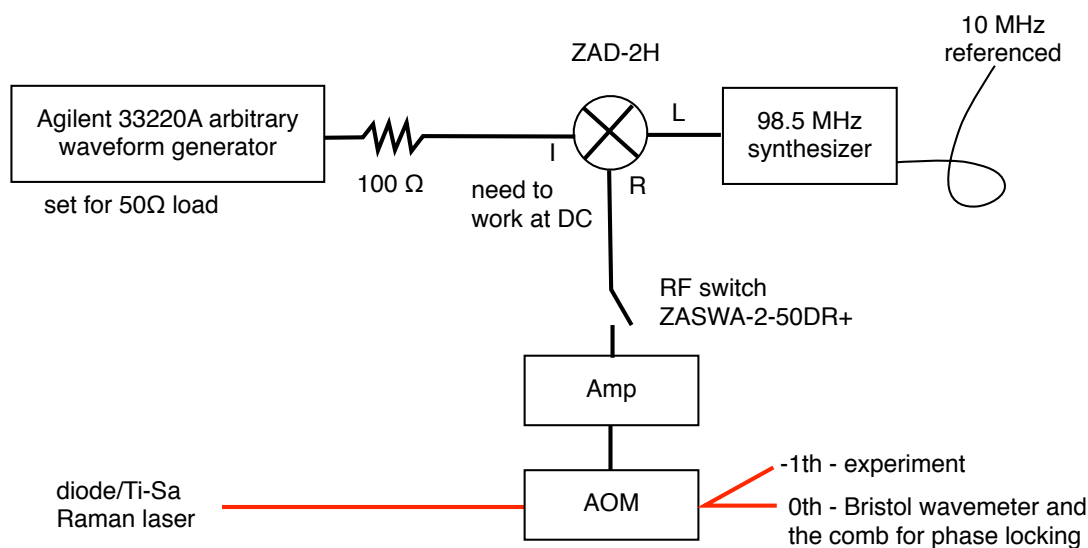


Figure 3.7: Layout of electronics for our Raman laser intensity ramp. Rf components are labelled by MiniCircuits part numbers.

Chapter 4

Feshbach Molecules

As was first introduced in Chapter 2.4, pairing atoms to form Feshbach molecules was the crucial first step to making a quantum gas of polar molecules. Feshbach molecules are exotic, extremely loosely bound molecules that only exist near a Fano-Feshbach resonance. These are scattering resonances that allow experimenters to control interactions in a quantum gas of atoms [78, 79, 80, 81]. This powerful tool has played a key role in a number of exciting developments in ultracold atom gases, such as realization of the BCS-BEC crossover in Fermi gases [82], the controlled collapse of a BEC [83], and the observation of bright matter wave solitons [84]. Here I will discuss one particular application, namely creation of Feshbach molecules, which is relevant to our experiment. As illustrated in Fig. 4.1(a), these resonances occur when the energy of a pair of atoms in one hyperfine scattering (open) channel is the same as the energy of a molecular bound state in a different hyperfine (closed) channel. Because the molecule and the pair of free atoms can have different magnetic moments, atom scattering can be tuned in and out of resonance using precisely controlled magnetic fields. This allows atom pairs to be converted into weakly bound molecules through an adiabatic magnetic-field sweep across a resonance (Fig. 4.1(b))[85]. This technique of magneto-association has been used for creation of homonuclear Feshbach molecules in studies of atomic Bose-Einstein condensates and quantum degenerate Fermi gases [16, 86]. Creation

of these homonuclear Feshbach molecules can be very efficient and has been shown to depend on only a single parameter, the phase-space density of the initial gas [87].

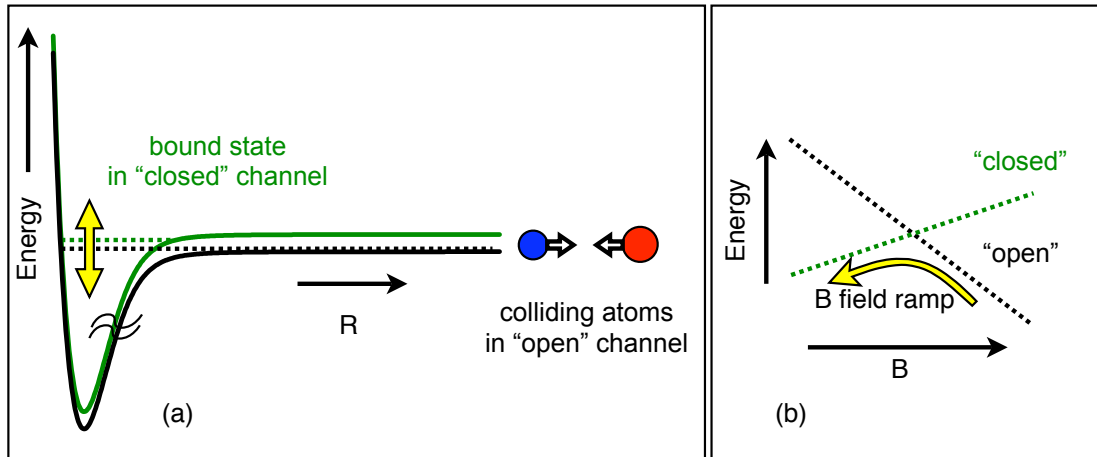


Figure 4.1: (a) A Fano-Feshbach resonance occurs when the energy of a pair of atoms in one hyperfine (“open”) channel is the same as a molecular bound state in a different hyperfine (“closed”) channel. The system can be tuned into and out of resonance by changing the strength of an applied external magnetic field. (b) An appropriate magnetic-field ramp across a Fano-Feshbach resonance can adiabatically convert pairs of atoms into weakly bound Feshbach molecules.

4.1 Heteronuclear Feshbach Molecules

To make polar molecules in the end, the starting Feshbach molecules have to be heteronuclear. Heteronuclear $^{40}\text{K}^{87}\text{Rb}$ Feshbach molecules were first created by rf-association in an optical lattice [23]. Subsequently, we characterized their properties [88] and made collisional measurements [24] using the same rf association technique but in a single-beam optical dipole trap. The details of these measurements can be found in J. Zirbel’s thesis [18]. One of the difficulties with rf association in our system is that the strong rf field can couple into our electronics. In particular, we find that the rf affects our magnetic field servos and cause

the magnetic field to change slightly. This makes the number of created Feshbach molecules irreproducible. Therefore, for all the experiments discussed in this thesis, we instead used a time-varying magnetic-field sweep across resonance to adiabatically convert pairs of atoms to Feshbach molecules. This method produces a few 10^4 molecules similar to the rf association technique, but is more robust day to day.

The Fano-Feshbach resonance we use for molecule creation has for its open channel the $K|F = 9/2, m_F = -9/2\rangle + \text{Rb}|1, 1\rangle$ state (labeled “*aa*” using P. Julienne’s convention [89]) while the closed channel is dominated by the $K|7/2, -7/2\rangle + \text{Rb}|1, 0\rangle$ state (labeled “*rb*”) at a resonant field of 546.7 G [90, 91, 92]. P. Julienne’s labeling convention is simply to label hyperfine states at a high magnetic field according to their energies. The lowest energy state is labelled “*a*” and the second lowest energy state is labelled “*b*”, etc. Since we work with molecules composed of K and Rb, the first label refers to the hyperfine state of K and the second label refers to Rb. The Feshbach molecule has a total angular momentum projection along the magnetic-field axis $m_F = -7/2$.

Before molecule creation, we first prepare an ultracold mixture of Rb and K atoms, with each species having on the order of a few 10^5 atoms, at a temperature around 200 nK in a single-beam optical dipole trap. A description of preparing the ultracold mixture can be found in Chapter 3. A few 10^4 Feshbach molecules are then created using a single linear field ramp from 8 G above the resonance to a field around 545.90 G in 4 ms. The field is provided by a set of Helmholtz coils (~ 9 cm in diameter). Because of imperfections in the current servo, the magnetic field immediately after the ramp overshoots 100 - 200 mG too low before the field settles to the final value (stable to 20 mG) within 2 ms. The molecule binding energy at 545.90 G is $h \cdot 240$ kHz. The molecular size is about $300 a_0$, and the closed channel fraction is $\sim 35\%$ [88]. The mean distance between atoms in an initial gas

density of 10^{13} cm^{-3} is a factor of 3000 bigger than the molecule size. The gas of Feshbach molecules typically has an expansion energy corresponding to 350 nK, while the initial atom gas temperature is ~ 200 nK. We have never investigated the heating systematically. However, it could be due to an “anti-evaporation” process from strong three-body loss near the Fano-Feshbach resonance. As we varied the initial atomic gas conditions and changed optical dipole trap waist many times over the years in which this thesis work was conducted, the Feshbach molecule expansion energy varied in the range between 150 nK to 700 nK.

4.1.1 Conversion Efficiency

Making a large number of Feshbach molecules is a prerequisite for our subsequent experiments, and here I share some experience of optimizing heteronuclear Feshbach molecule creation. As has been mentioned, in the case of homonuclear Feshbach molecule creation, the phase-space density of the initial atomic gas is a single parameter that determines the saturated conversion efficiency for a slow ramp[87]. For a degenerate Fermi gas, up to 90% conversion efficiency from atoms to molecules has been demonstrated [87]. For heteronuclear $^{85}\text{Rb}^{87}\text{Rb}$ molecules where the constituent atoms are both bosons [93], it has been shown that only the phase-space density of one gas determines the efficiency provided that the cloud spatial overlap is good.

For $^{40}\text{K}^{87}\text{Rb}$ Feshbach molecules, the best efficiency demonstrated so far in a single-beam optical trap is 25% using rf association [88]. According to a phenomenological model that fits our data well, the relatively low efficiency comes from two competing factors, namely, the phase-space density and the spatial overlap of the ^{40}K and ^{87}Rb clouds. There is a mismatch in the cloud sizes for the fermionic K gas and bosonic Rb gas when the gases are well in the quantum degeneracy regime due to Pauli pressure for the fermions. In addition, the equilibrium

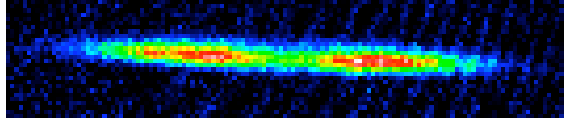


Figure 4.2: An image of an expanded cloud of Feshbach molecules that shows a low density region in the center of the cloud. Since the trap frequency is low in the horizontal direction, we probe the in-trap position of the cloud in the horizontal direction after a short time-of-flight expansion. The hole in the density profile is due to large inelastic loss in the region of high Rb density.

positions of the two clouds in a weak optical trap are displaced in the vertical direction due to the balance of the optical trapping force and the gravitational force, which is larger for the heavier Rb atoms. The best molecular conversion efficiency was found close to $T/T_c = 1$ experimentally with our parameters, where T_c is the temperature of the onset of a Bose-Einstein condensation [88].

In addition to phase-space density and spatial overlap of the clouds, KRb Feshbach molecules suffer strong inelastic collisions, especially with Rb atoms [24]. This becomes an important issue when using a long duration adiabatic field ramp to make molecules. In Fig. 4.2, I show an example of Feshbach molecules with a large loss at the center due to a high Rb density gas. To avoid strong loss due to Rb, we choose to operate at higher gas temperature where the Rb density is lower. In the end, we typically work with a conversion efficiency of 10-20%.

4.1.2 Lifetime

Feshbach molecules are in a high vibrationally excited (high- v) state and can be vibrationally quenched in ms time scales from collisions with residual Rb and K atoms in our trap. Each inelastic collision results in a large energy release and subsequently, the molecule is lost from our trap. To prolong the lifetime

of Feshbach molecules, we remove residual atoms using a combination of rf or microwave fields to transfer these atoms to a state with (quasi-)cycling transition followed by resonant light pulses to heat the atoms out of the optical trap [18].

The Rb($|1, 1\rangle$) removal procedure is the following. We first spin flip Rb from $|1, 1\rangle$ to $|2, 2\rangle$ using a pulse of microwave near 8 GHz and then apply a short light pulse that drives the $|2, 2\rangle$ to $|F' = 3, m'_F = 3\rangle$ cycling transition. Because $|1, 1\rangle$ to $|2, 2\rangle$ has a large magnetic field sensitivity (2.3 MHz/G at 546 G) and our field ramp usually takes 2 ms to settle after reaching the final field, we use an Adiabatic Rapid Passage(ARP) of duration 200 μ s where we sweep the microwave frequency to perform the spin flip. Each ARP has an efficiency higher than 95%. We perform the procedure (ARP + blast light pulse) three times in a 1 ms time span starting at 1 ms after the field ramp.

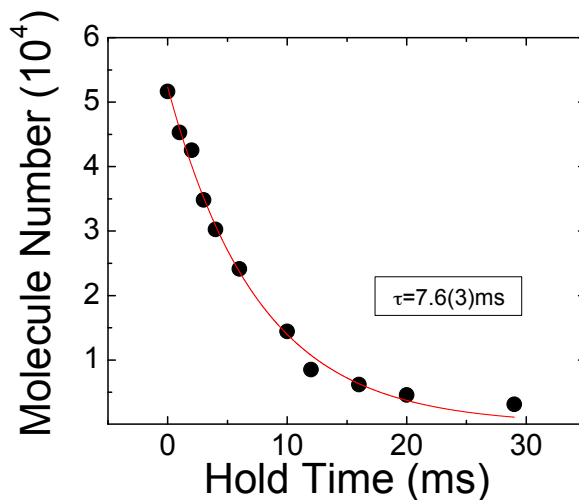


Figure 4.3: A typical KRb Feshbach molecule lifetime. Looking at the KRb lifetime v.s. field behavior (not shown here) as compared to [24], we believe the lifetime is limited by residual undetected K atoms. However, this is sufficiently long to perform state transfer to more deeply bound molecular state.

The $K(|9/2, -9/2\rangle)$ removal involves two spin flips and an optical transition. The two spin flips drive $|9/2, -9/2\rangle$ first to $|9/2, -7/2\rangle$ and then to $|9/2, -5/2\rangle$ both using rf- π -pulses with durations on the order of $10 \mu\text{s}$. Finally, a light pulse of $50 \mu\text{s}$ resonant with the $|9/2, -5/2\rangle$ to $|11/2, -5/2\rangle$ transition is applied to remove K from the trap. This is a 96%-closed cycling transition. The light is 140 MHz red-detuned from the Feshbach molecule-free atom ($K |F' = 11/2, m'_F = -11/2\rangle$) transition.

An alternative of K removal in the later experiments, we “hide” molecules in a deeply bound vibrational state and then turn on the 100%-closed cycling light on the $|9/2, -9/2\rangle$ to $|11/2, -11/2\rangle$ transition to directly remove residual K atoms.

After the K and Rb removal procedures, the number of residual atoms is less than the minimum number we can detect with our absorption imaging (< 3000 in the single-beam optical trap and < 1000 in the crossed-beam optical trap). A typical lifetime for trapped Feshbach molecules is then 7 ms at 545.88 G as shown in Fig. 4.3 (using the first K removal procedure), which is more than sufficient for further internal state manipulation of the molecules.

4.1.3 Electric Dipole Moment

We can create a high phase-space-density gas of heteronuclear Feshbach molecules. However, because the average separation of the two nuclei in each molecule is relatively large, on the order of $300 a_0$, the two valence electrons are only extremely weakly shared by the nuclei; therefore, the molecular electric dipole moment is negligible. *Ab initio* calculations of the permanent electric dipole moment (Fig. 4.4) as a function of the internuclear separation from Kotochigova *et al.* [94] give a dipole moment of $5 \cdot 10^{-11}$ D for KRb Feshbach molecules. Only when the internuclear separation is smaller than $10 a_0$, does the dipole moment

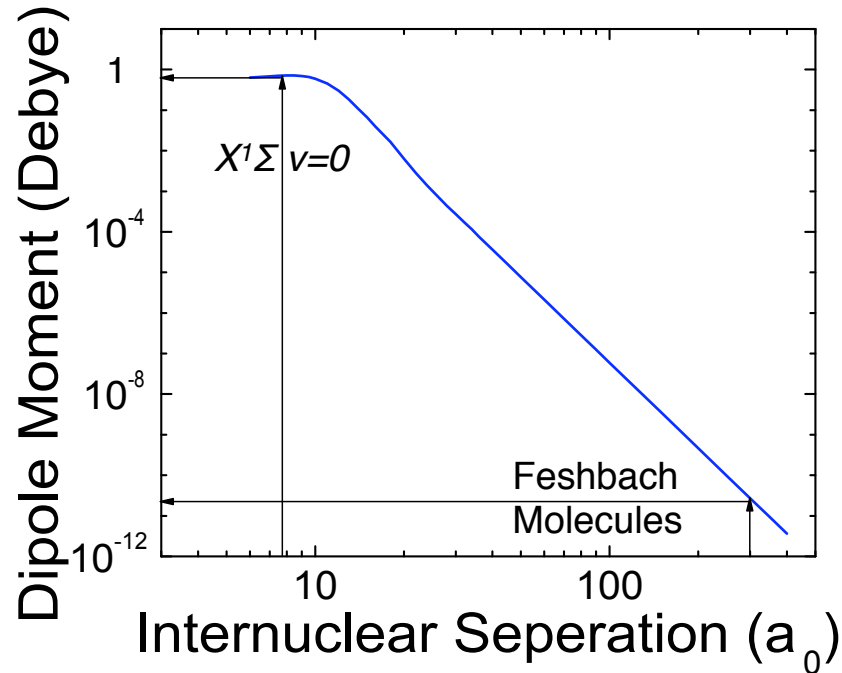


Figure 4.4: Calculated KRb permanent electric dipole moment as a function of internuclear separation [94]. Feshbach molecules have a size of the order $\sim 300 a_0$ and a negligible dipole moment of $\sim 10^{-11}$ D. To make molecules polar, we need to shrink the the internuclear separation, e.g. absolute ground-state molecules have a dipole moment of ~ 1 D.

approach its maximum value of nearly 1 D. Therefore, to make polar molecules in the next step we want to manipulate the molecules' internal state to reach a deeply bound level where the molecule is small and has a significant electric dipole moment. In thinking about this next step, it should also be noted that in spite of the fact that Feshbach molecules are unusually large dimers, the magneto-association step nevertheless reduces the internuclear separation from a few tens of thousand a_0 in the initial atom gas to a few hundred a_0 in the molecules. This facilitates further molecule state manipulation by providing a much larger wavefunction overlap to deeply bound states.

4.2 Enhancement Factor

The importance of this first step of magneto-association can be seen in a measured enhancement of the optical excitation rate to a KRb^* (KRb electronically excited) state. Here, I present measurements of this enhancement not only for a near-threshold KRb^* state, but also for a deeply bound KRb^* state. This is relevant to the use of optical transitions to bring Feshbach molecules either to a lower vibrational state near the atomic threshold in one case (see Chapter 6) or finally to the lowest ro-vibronic ground state (Chapter 8). The comparison, as illustrated in Figure 4.5, is to apply a light pulse to drive a bound-bound transition from Feshbach molecules or a free-bound (photo-association) transition from atoms to an electronically excited state to make KRb^* molecules. The excited-state molecules then subsequently decay, with the rate Γ , and are lost from the corresponding Feshbach molecule or atom signal. This KRb^* molecule creation rate can be characterized by an exponential time scale τ relevant to the transition Rabi frequency Ω as $\tau = \Gamma/\Omega^2$. To back out the transition-dipole-included Franck-Condon factor (FCF) of the bound-bound or free-bound transition, we normalize the coupling Rabi frequency by the laser intensity, Ω^2/I .

In Figure 4.6, we compare the FCF enhancement of bound-bound to free-bound transitions for a near-threshold excited state ($v' = -9$ of the $2(1)$ potential, $E_b = h \cdot 43$ GHz). In Figure 4.7, the FCF enhancement comparison is done for the same *deeply* bound excited state that we use for the coherent optical transfer to the absolute ground state, as described in Chapter 8. In Figure 4.6, the enhancement factor is $\frac{\Omega_m^2/I_m}{\Omega_a^2/I_a} \approx 500$; while in the case of a deeply bound excited state (Figure 4.7), the enhancement factor is even higher, ≈ 5000 ! This large enhancement factor reveals several orders of magnitude advantage when initiating the final population transfer step from a weakly bound vs free atom precursor state.

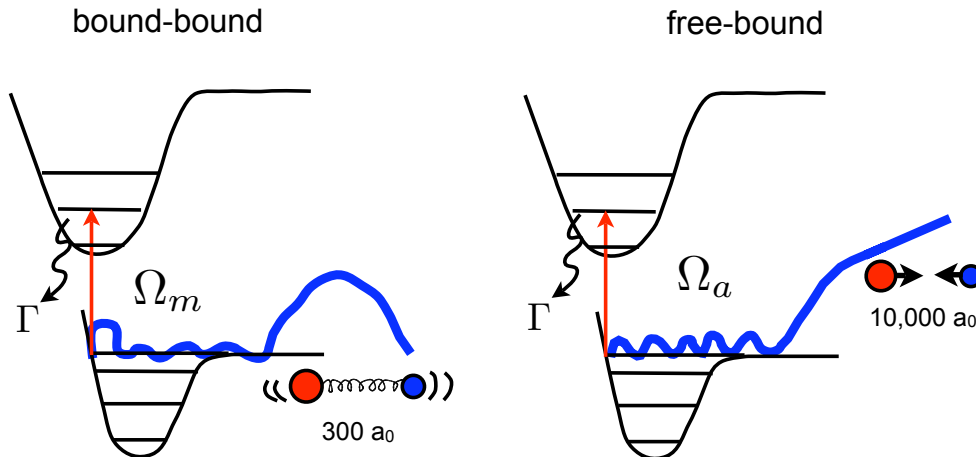


Figure 4.5: Schematic of the comparison of optical excitation rates for bound-bound and for free-bound transitions. In both cases, the target bound state is the same. The transition strengths are characterized by a Rabi frequency Ω . Once molecules are in KRb excited electronic state, they decay spontaneously with a common rate Γ . The depletion of molecules/atoms can be characterized by an exponential time scale, $e^{-t/\tau}$, where $\tau = \Gamma/\Omega^2$. By measuring the time scale, we can compare Ω for the two cases.

4.3 Detection

Finally, before discussing the next step in creating absolute ground-state molecules (or any deeply bound ground-state molecules), we need to consider molecule detection. To detect molecules, we use a method that is very standard in an ultracold atom experiment but may not be the most intuitive method for people who work with “chemist’s molecules”.

To probe atoms, we use time-of-flight (TOF) absorption imaging. Here, the gas is suddenly released from the trap and then imaged after an expansion time (TOF) that is typically a few to a few tens of ms. For the imaging, a pulse of resonant laser light illuminates the expanded gas and a CCD camera records the shadow image of the cloud. The total number of atoms and their momentum distribution can be obtained from these images.

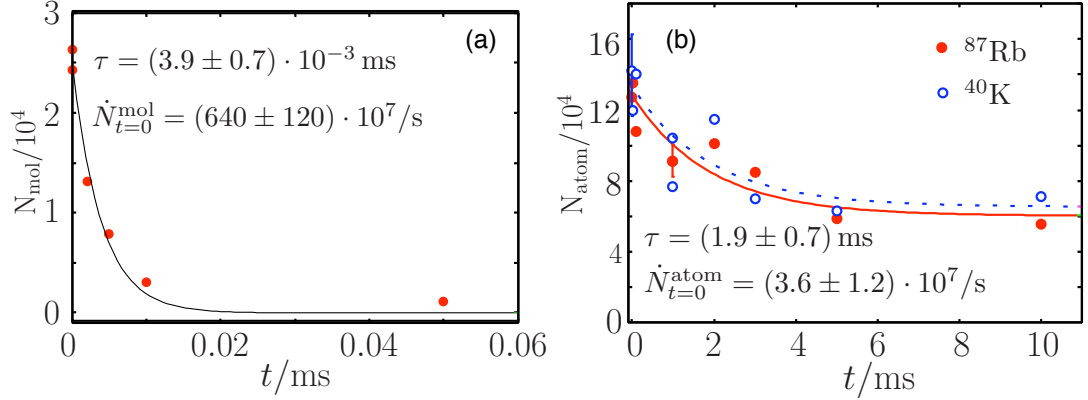


Figure 4.6: Comparison of the optical excitation rates for (a) Feshbach molecules and (b) atoms to an excited state near the atomic threshold, $v' = -9$ of $2(1)$ (the notation that labels the molecular state will be introduced in Chapter 5). This comparison was taken using the same laser power in both cases. From the time scale, we see the enhancement factor for starting with Feshbach molecules as compared to starting with atoms is $\propto \frac{\Omega_m^2}{\Omega_a^2} = \frac{\tau_a}{\tau_m} \approx 500$.

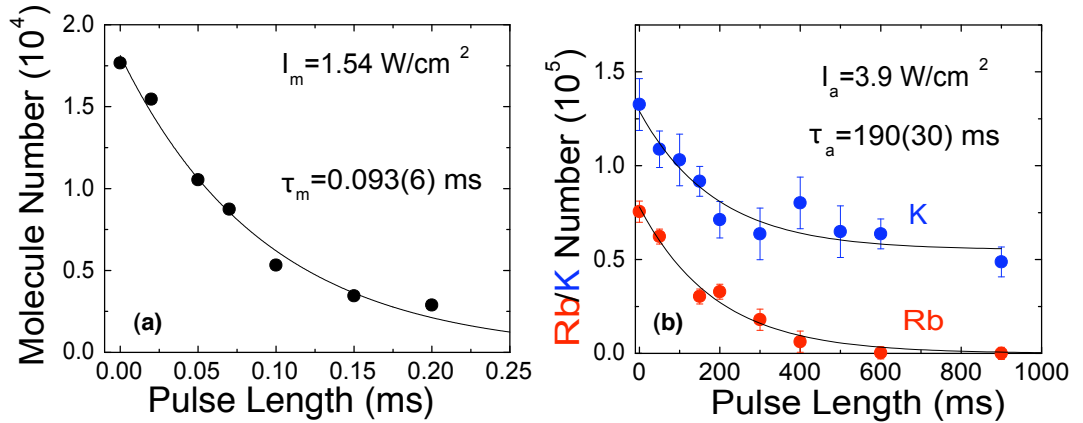


Figure 4.7: Comparison of the optical excitation rates (a) from Feshbach molecules to a deeply bound excited state ($v' = 23$ of the excited $2^3\Sigma^+$ potential) and (b) from atoms to the same excited state. The measured depletion of the molecule/atom population is due to excited KRb^* formation followed by spontaneous decay and loss from the system. The KRb^* formation rates were characterized by the exponential time scales, τ_m and τ_a , respectively. The enhancement factor for starting from Feshbach molecules instead of atoms near the Fano-Feshbach resonance is $\frac{\tau_a/I_a}{\tau_m/I_m} \approx 5000$.

For molecules, however, imaging, or even just detecting molecules, with light absorption is much more challenging by the complicated internal state structure and lack of a clean two-level cycling transition. An extremely useful feature of heteronuclear Feshbach molecules, which have a tiny binding energy at magnetic fields near resonance, is that they can be imaged using light resonant with an atomic cycling transition [23]. At an applied magnetic field of 546 G, which is less than 1 G detuned from a K-Rb resonance, KRb Feshbach molecules can be imaged using light resonant with the K atom cycling transition. When a molecule absorbs a photon, it dissociates, after which subsequent photons can scatter off the resulting free K atom. This gives a strong absorption signal, but does not distinguish between Feshbach molecules and any leftover unbound K atoms. To image only the Feshbach molecules, we remove selectively unbound K atoms ($|9/2, -9/2\rangle$) using rf transition as described in section 4.1.2. In our system, we typically image Feshbach molecules with an efficiency of 85% as compared to K atoms at the same magnetic field. In Figure 4.8, we show a series of TOF absorption images of the Feshbach molecule gas. For each absorption image of the gas, we fit the optical depth (OD) of the gas as two gaussians in the horizontal and the vertical directions,

$$OD(x, z) = OD_{peak} \cdot e^{-x^2/2\sigma_x^2} \cdot e^{-z^2/2\sigma_z^2}. \quad (4.1)$$

The cloud sizes, σ_x and σ_z , give information of the expansion energy of the gas:

$$\sigma_x^2 = \frac{k_b T}{m\omega_x^2} [1 + (\omega_x t)^2] \text{ and } \sigma_z^2 = \frac{k_b T}{m\omega_z^2} [1 + (\omega_z t)^2], \quad (4.2)$$

where ω_x and ω_z are the trap frequencies in the x- and the z-directions. In the case when the expansion time is long compared to the trap period, the expansion energy can be directly extracted from $k_b T = (m \sigma^2 / t^2)$. The cloud size and its

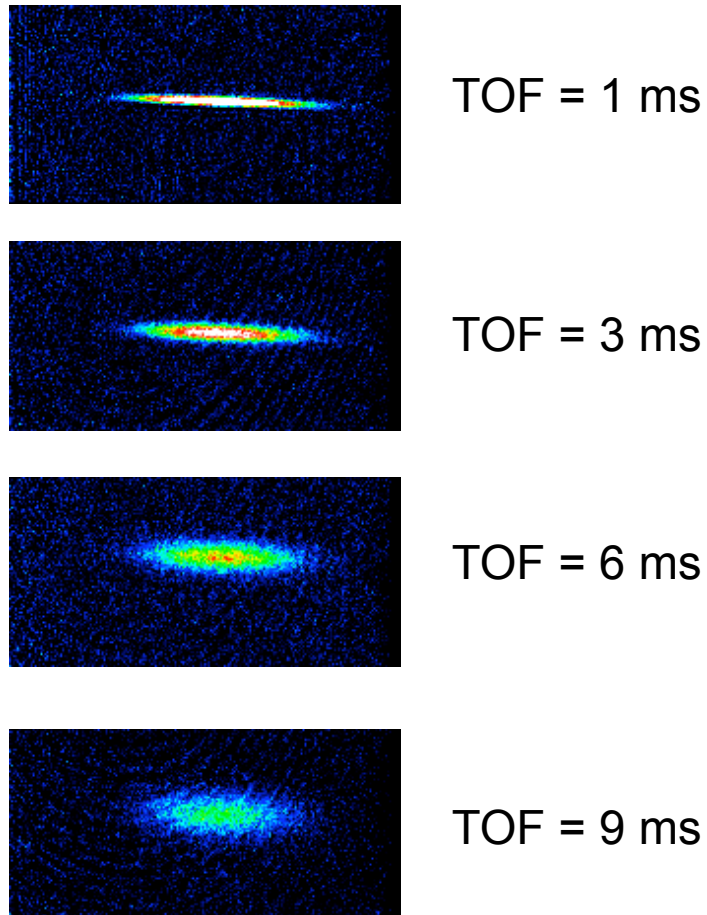


Figure 4.8: A series of time-of-flight images for KRb Feshbach molecules created within 1G of the resonance field. From these images, we can extract the total number of molecules ($5.3 \cdot 10^4$) and the expansion energy ($k_b \cdot 330$ nK) of the molecular gas.

peak optical depth give information of the total molecule number,

$$N = \sigma_x \sigma_z O D_{peak} (1 + 4(\frac{\Delta}{\Gamma})^2) / \sigma_0 / (\text{eff}), \quad (4.3)$$

where Δ is the laser detuning, Γ is the natural linewidth of the transition, σ_0 is the scattering cross section, and eff is the detection efficiency. From these images (Fig. 4.8), we determine that we create $5.3 \cdot 10^4$ Feshbach molecules, at an expansion energy corresponding to a temperature of 330 nK.

This detection technique cannot be directly applied to deeply bound molecules. However, by combining detection of Feshbach molecules with efficient manipulation of the molecules' internal states, we can bring ground-state molecules back to the Feshbach state and then image. This give us information of molecule number and their momentum distribution. This technique is very powerful for studying the quantum behavior of a gas of polar molecules.

Chapter 5

KRb* Potentials

Producing a large number of ultracold heteronuclear KRb Feshbach molecules with T/T_F as low as 1.4 is only the first step toward the creation of ultracold polar molecules. This is because the internuclear separation of Feshbach molecules is still too large to have any significant electric dipole moment (Fig. 4.4). To make ultracold polar molecules, we need to shrink the size of the Feshbach molecules significantly. We achieved this by transferring KRb molecules into a tightly bound internal state using a two-photon Raman technique (discussed in the next chapter). The success of such a technique relies on the identification of one or more suitable electronically excited intermediate states that bridge the very different size wavefunctions for the initial and final molecular states. To look for a suitable intermediate state, we started by understanding and spectroscopically probing the KRb excited electronic potentials (KRb*). This chapter contains relevant information concerning particular excited states and is not a comprehensive study of KRb*.

5.1 Hund's Coupling Cases

To study KRb excited potentials, we first need to be acquainted with some molecular notation. Because molecules have rich internal structure, molecular states are often described by a large set of quantum numbers. Figuring out a set of

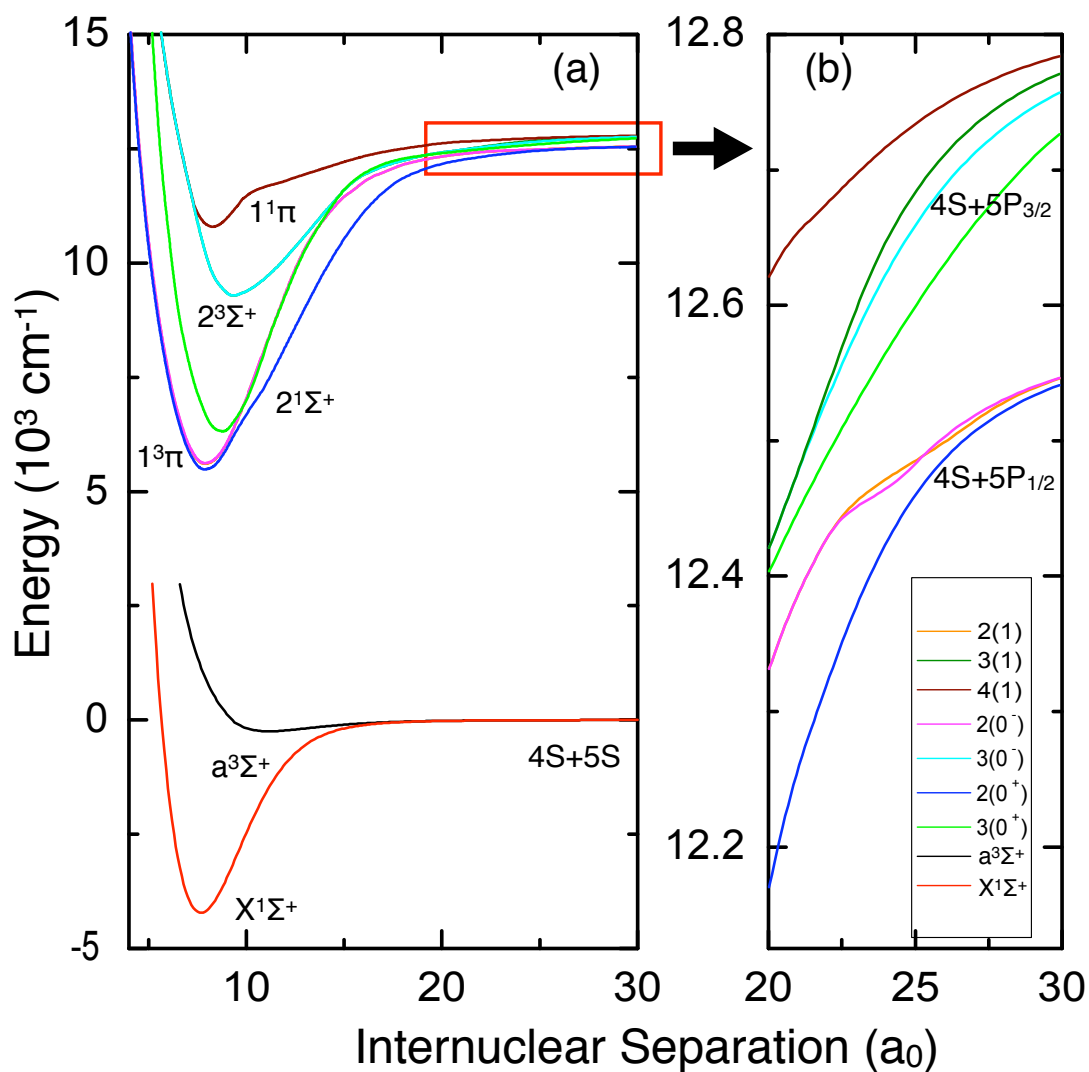


Figure 5.1: KRb electronic potentials (from *ab initio* calculations in [94]). (a) The potentials are shown for electronic ground-state potentials that asymptotically go to the $4S+5S$ atomic threshold and electronic excited potentials that connect to the $4S+5P$ threshold. Molecular potentials in the short range are labelled by molecular spectroscopic notations described in the section of Hund's case a. (b) A zoomed diagram of the excited potentials at large internuclear separations. Due to strong spin-orbit coupling in this regime, the potentials are labelled by their total angular momentum projection onto the internuclear axis, Ω , Hund's case c.

the “good” quantum numbers is essential for understanding molecular potentials and their spectra. A very useful and general guideline is the Hund’s cases based on couplings between electronic and rotational motions [95]. Here, I will only mention the relevant Hund’s cases for this work, namely case (a), (b), and (c).

5.1.1 Hund’s Case (a)

The most commonly encountered Hund’s case is Hund’s case (a). In this case, molecular electronic orbital angular momentum L is strongly coupled to the internuclear molecular axis and the electronic spin S in turn is strongly coupled to L through spin-orbit coupling. Projections of L and S onto the molecular axis are Λ and Σ . $\Lambda + \Sigma = \Omega$ is the total angular momentum projection onto the molecular axis. Heteronuclear molecular potentials at a small internuclear separation are usually Hund’s case (a) (Fig. 5.1(a)) and can be labelled using molecular spectroscopic notation as $^{2\Sigma+1}\Lambda_{\Omega}^{+/-}$, where $+/-$ refers to reflection symmetry of the spatial electronic wave function through the plane containing the internuclear axis. For $\Lambda = 0, 1, 2$, etc, the corresponding spectroscopic notations are Σ, Π, Δ , etc. The spectroscopic notations are sometimes preceded with a letter- or numbered-label such as X, a, b, 1, 2, etc. The potential labelled by X denotes the absolute lowest electronic potential of the molecule. Any higher lying electronic potentials from X are labelled sequentially by a, b, c, etc for the electronic ground potentials (or 1, 2, 3, etc for the electronic excited potentials) that have otherwise the same spectroscopic notation.

5.1.2 Hund’s Case (b)

Hund’s coupling case (b) describes molecules with $\Lambda = 0$, e.g. $X^1\Sigma^+$ and $a^3\Sigma^+$ of KRb. $X^1\Sigma^+$ described the lowest (X) electronic state of KRb that has $S = 1, \Lambda = 0$. In this case, rotations of molecular nuclei, N , are decoupled from

S and the nuclear spin (I).

5.1.3 Hund's Case (c)

Hund's case (c) usually describes molecules with a large internuclear separation, where strong spin-orbit coupling between L and S dominates over their coupling to the molecular axis individually. In this case, Ω is a good quantum number but Λ and Σ are not. Therefore, potentials near the dissociation limit (Fig. 5.1(b)) are labelled by Ω . This notation can also be used to label potentials at short range (Fig. 5.1(a)) when Ω is emphasized (Ω is always a good quantum number for Hund's case (a) molecules), however, additional quantum numbers will be required.

5.2 Near-Threshold States

Molecular spectra, although complex, usually have some regularities in the spacing between spectra lines. The largest periodic spacing between lines of the excited potentials near the atomic threshold $4S+5P$ corresponding to the spacing of vibrational states. At this large internuclear distance, vibrational series follow potentials that are labelled in the Hund's case (c). These potentials, $2(1)$, $3(1)$, $4(1)$, $2(0)^+$, $2(0)^-$, etc, shown in Fig. 5.1(b) are characterized by their total angular momentum projection, Ω . The first number 2, 3, 4 labels the progression of the potentials according to their energy for the same Ω in the parentheses and +/- labels the reflection symmetry of the total electronic wave function, including spin, through a plane containing the internuclear axis. Excited molecular states near threshold are expected to have a decent Franck-Condon overlap (apart from considering wavefunction nodal patterns) with Feshbach molecule wavefunctions even when their size is about 10 times smaller than the Feshbach molecules.

To look for these vibrational series, we scanned a tunable Ti-Sa laser (Chap-

ter 3.3.1) to drive bound-bound transitions from Feshbach molecules. After transitions to KRb^* , molecules spontaneously decay and are lost from our absorption signal. Using loss spectra, we located excited vibrational series. All the frequencies of the levels obtained are referenced to the transition from the $4\text{S}+5\text{S}$ atomic threshold with K in $|9/2, -9/2\rangle$ and Rb in $|1, 1\rangle$ to $4\text{S}+5\text{P}_{1/2}$ threshold with K in $|9/2, -9/2\rangle$ and Rb in $|2, x\rangle$ at 546 G. Empirically, this “reference” transition was observed at 377111.684(4) GHz which was measured using a wavemeter. We performed a scan from ~ 30 GHz below the $4\text{S}+5\text{P}_{1/2}$ atomic threshold to ~ 800 GHz ($\sim 25 \text{ cm}^{-1}$) below.

To identify which of the observed vibrational levels are associated with the $\Omega = 1$ or the $\Omega = 0$ potentials, we looked at the hyperfine structure of the levels. Because we conducted our search at a high magnetic field, for each $\Omega = 1$ level, we expected to see rich hyperfine structure that has spacings comparable to that of rotational structure; while for each $\Omega = 0$ level, we expected a much simpler spectrum. A typical structure-rich spectrum of a $\Omega = 1$ vibrational level ($v' = -9$, where the minus sign refers to counting the vibrational quantum number from the atomic threshold) is shown in Fig 5.2. Each line dip corresponds to loss of Feshbach molecules due to the laser driving a bound-bound transition. A typical spectrum of $\Omega = 0$ ($v' = -14$) is shown in Fig. 5.3 where both 0^+ and 0^- are seen. The structure associated with $\Omega = 0^+/0^-$ are rotational lines.

To identify the particular potential, e.g. 2(1) but not 3(1), we compared our observed vibrational spectra to S. Kotochigova’s prediction based on her potentials in [94]. Although the exact location of the calculated series may not be accurate, the spacings between vibrational levels are usually good. To confirm our assignment, we analyzed the vibrational spacings further. LeRoy and Bernstein [96] and Stwalley [97] had independently shown that vibrational spacings near the dissociation limit (i.e. near the atomic threshold) are determined only by the

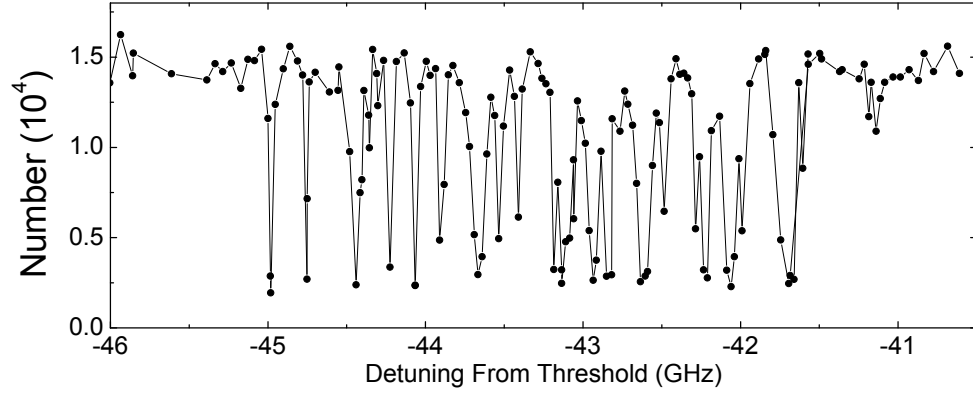


Figure 5.2: A typical hyperfine-rich spectrum of a vibrational level of the 2(1) potential near the atomic threshold. The spectrum is shown for the $v' = -9$ level, where the minus sign refers to counting the vibrational quantum number from the atomic threshold, using π -polarization laser light.

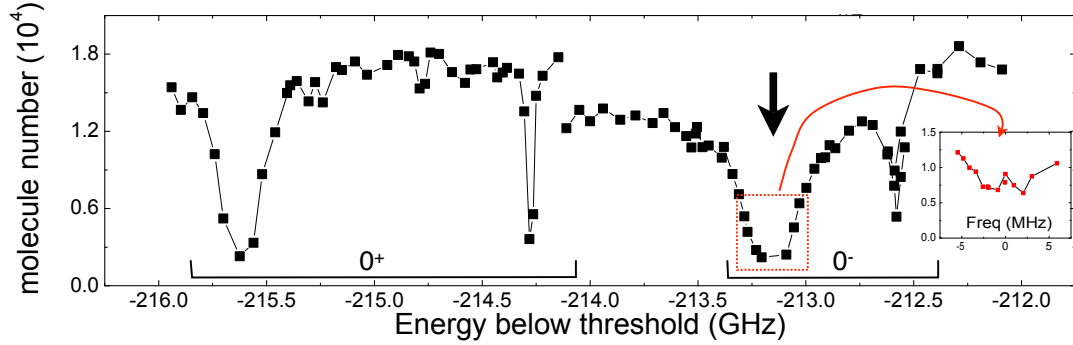


Figure 5.3: A Typical spectrum a 2(0) vibrational level ($v' = -14$). Here we observe both the 0^+ and the 0^- components. Since their structure is similar, we identified them through their difference in vibrational spacing with adjacent levels (Fig. 5.4(b)). (Inset) Detailed scan of the 0^- component that reveals a doublet structure.

long-range potential. Therefore, we can relate the vibrational quantum number v' (counting from the threshold) to their binding energy, E'_v , by a semiclassical equation [96, 97, 98]

$$v' = -\frac{2\sqrt{\pi}}{h(n-2)} \frac{\Gamma(1/2 + 1/n)}{\Gamma(1 + 1/n)} \sqrt{2\mu} C_n^{1/n} E_{v'}^{(n-2)/2n} + v'_0 \quad (5.1)$$

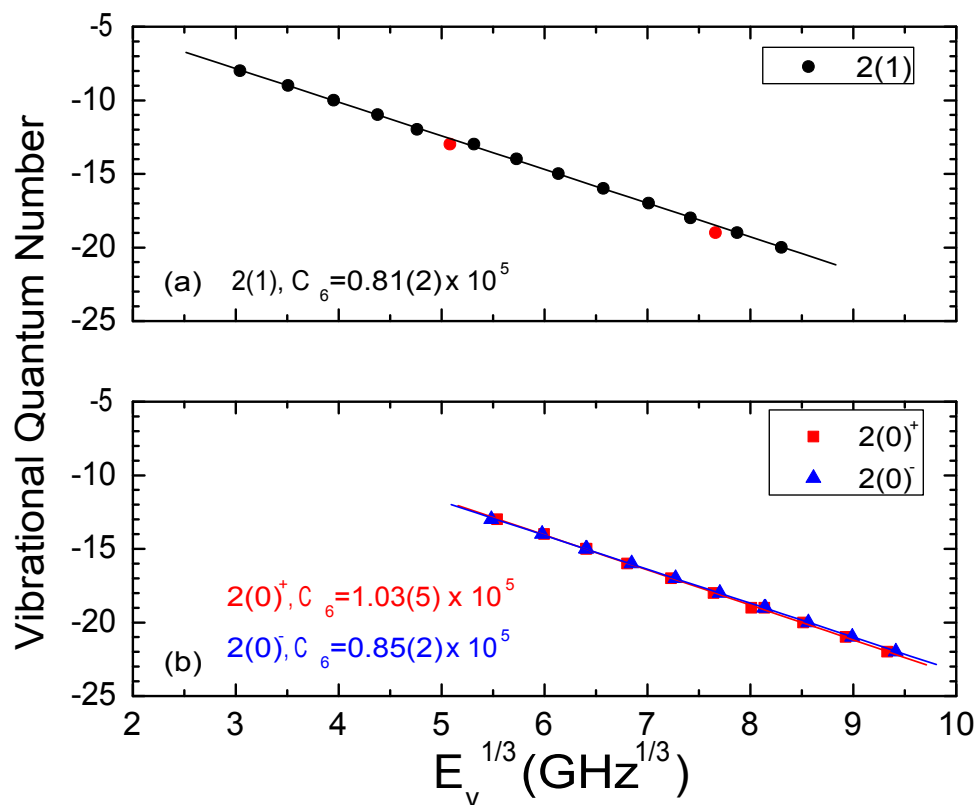


Figure 5.4: Vibrational series of (a) $2(1)$, (b) $2(0^+)$, and $2(0^-)$. By fitting with equation 5.1, we can extract the C_6 coefficient that describes the potentials in the near-dissociation regime. In addition, for (a), we distinguished two levels (in red) that have $\Omega = 1$ structure but belong to a different potential, $3(1)$.

where $n = 6$ for our van der Waals long-range potential, h is the Planck's constant, Γ denotes the Gamma function, μ is the reduced mass, and v'_0 is a fitting offset. In Fig. 5.4, we plot the $2(1)$, $2(0)^+$, and $2(0)^-$ vibrational series v' vs $E_{v'}^{1/3}$ and see that our data rarely deviating from the linear fit. We also extracted C_6 from the fit using equation 5.1. This extracted C_6 is about 10-20% lower from the theory calculations. A more accurate long-range potential is characterized by C_6 , C_8 , and perhaps C_{10} . To get a better potential in the long-range, S. Kotochigova adjusted her values for C_6 and C_8 (C_{10} was set to zero) by fitting our data. Moreover, deviations from the linear relation in Fig. 5.4(a) allowed us to distinguish vibrational levels (red points, 131.25 GHz- and 450 GHz-detuned) that have $\Omega = 1$ structure but belong to the $3(1)$ potential, which asymptotically goes to the $4S+5P_{3/2}$ threshold. All observed levels and their assignments are summarized in Table 5.1.

v'	2(1) (GHz)	2(0) ⁻ (GHz)	2(0) ⁺ (GHz)
-8	28.2		
-9	43.3		
-10	61.8		
-11	83.9		
-12	108.1		
-13	150.3	165	170
-14	188	213.4	215.7
-15	231	262.5	263.3
-16	284	321.2	314.7
-17	345.2	385	377.8
-18	408.5	457.08	446.7
-19	488.0	541.0	514.0
-20	572.8	628.2	616.9
-21		726.9	711.4
-22		833.9	812.6

Table 5.1: Summary of vibrational levels observed near the atomic threshold of $4S+5P$. The frequencies are given for the line center of power-broadened lineshapes and were measured using a wavemeter.

5.2.1 $v' = -14$ of $2(0^-)$

In the last section, we identified different vibrational series in the excited electronic states near the dissociation limit. From these data, we picked $v' = -14$ of $2(0^-)$ as an intermediate state for two-photon transfer to near-threshold ground states. In particular we chose a strong feature (indicated with an arrow) that is isolated from other lines by ~ 1 GHz. The isolation of the line is crucial for working with a clean three-level system for an efficient population transfer. A detailed scan of the feature indicated by the arrow reveals a doublet substructure.

5.3 Bridging to Deeply Bound Molecules

Performing spectroscopy near the dissociation limit of the electronic excited states enabled us to choose a suitable intermediate state for near-threshold molecular state transfer (Chapter 6). However, these near-threshold excited states are not suitable for bridging the large difference in the molecular wavefunction of Feshbach molecules and deeply bound states of the electronic ground potentials. In Fig. 5.5, we plot the square of the total transition dipole moment (this includes the electronic transition dipole moment square and the wavefunction overlap) for transitions from vibrational levels of the $2(0)^+$ (Fig. 5.5a) and $3(1)$ (Fig. 5.5b) potentials to both the near-threshold $v = -1$ and the deeply bound $v = 0$ of $a^3\Sigma^+$, and the deeply bound $v = 0$ of $X^1\Sigma^+$. For the deeply bound levels, we no longer number v from threshold, and $v = 0$ is in fact the lowest energy level of the potential. The transition dipole moments are calculated by S. Kotochigova and are plotted as a function of their detuning energy from threshold. As we can see, the near-threshold excited states are only good for near-threshold ground states, e.g. the $v = -1$ state. Therefore, to find an appropriate molecular state that can bridge $v = -1$ and $v = 0$ simultaneously, we have to choose a deeply

bound excited state. (In fact, our initial molecular state will be weakly bound Feshbach molecules, which would have an even weaker transition dipole moment to the excited state as compare to the $v = -1$ case.) In the deeply bound regime (where the position of the inner turning point of $v = -1$ has good amplitude), we found several excited-state potentials that could serve as the bridge. To pursue molecule internal state transfer from Feshbach molecules to the triplet or the singlet rovibrational ground state, we chose to go through deeply bound vibrational levels of the $2^3\Sigma^+$ potential (also labeled as $3(1)$ and $3(0)^-$ according to their Ω components).

5.4 $2^3\Sigma^+$ and the $\Omega = 0^-$ and $\Omega = 1$ Components

Looking at the full set of electronic potential curves (Fig. 5.1), it is not difficult to see that there are certain “coincidences” where inner and outer turning points of an excited state vibrational level could line up well to overlap both the Feshbach molecule state (basically at $E_{energy} = 0$) and the $v = 0$ state of either $a^3\Sigma^+$ or $X^1\Sigma^+$. Our choice was the vibrational levels associated with $2^3\Sigma^+$, which have relatively large calculated transition dipole moments to our desired molecular ground states and have transition frequencies that are conveniently covered by our widely tunable Ti-Sa laser as well as commercial diode lasers. To experimentally identify these states, since potentials in this region are usually constructed by *ab initio* calculations, where there could be a large uncertainty in the predicted energies of vibrational levels, we looked for available experimental spectroscopy data as a guideline. The $v' = 0$ to $v' = 13$ of $2^3\Sigma^+$ for $^{39}\text{K}^{85}\text{Rb}$ has been reported by [27]. Our search was guided by Kotochigova’s *ab initio* calculation fitted to experimental data from $^{39}\text{K}^{85}\text{Rb}$ [27], with the appropriate mass scalings.

The $2^3\Sigma^+$ potential has two components in the short range that are distinguished by their quantum number $\Omega = 0^-$ or 1, which in turn can be used

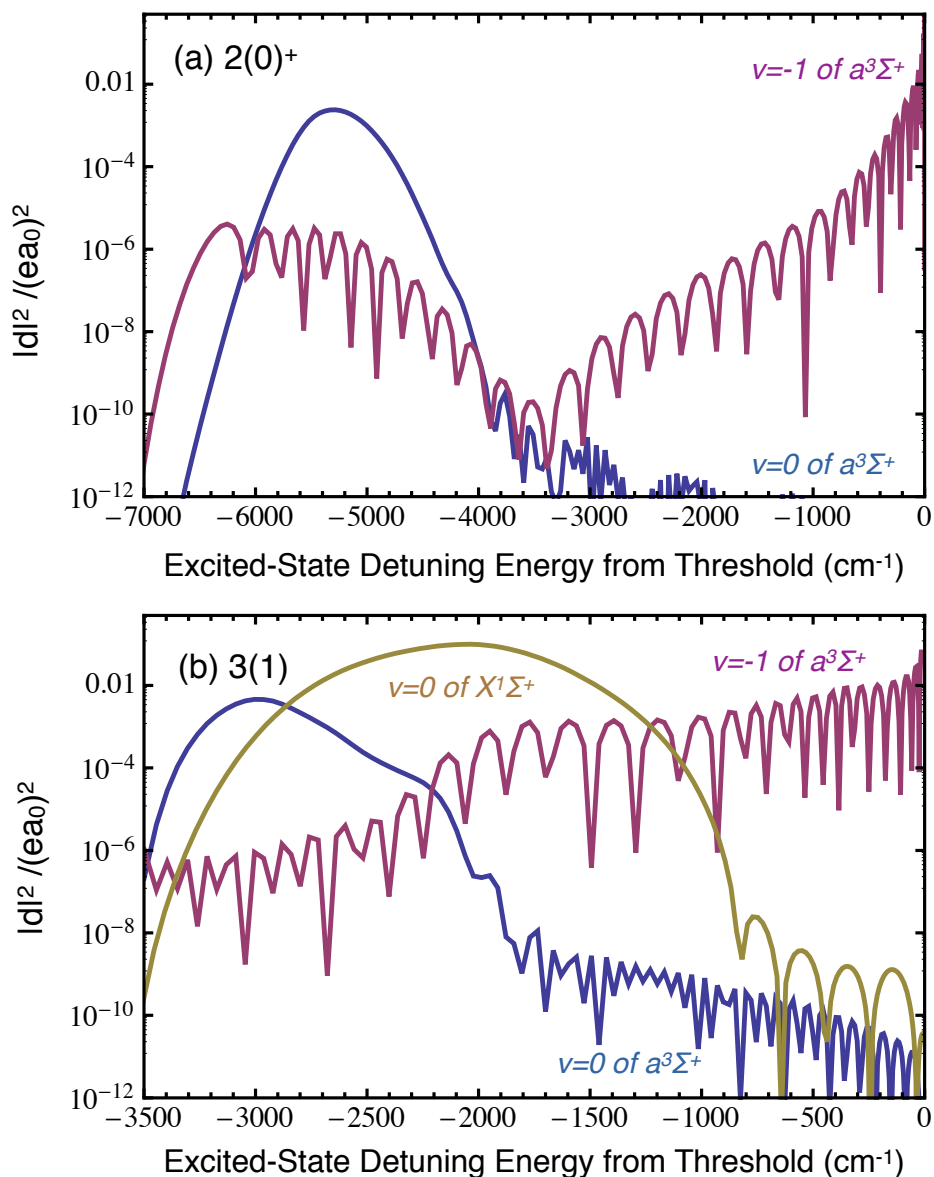


Figure 5.5: Predicted transition dipole moments from vibrational level in the electronically excited potentials (a) $2(0)^+$ and (b) $3(1)$ to $v = -1$ and $v = 0$ of the triplet ground-state potential $a^3\Sigma^+$ and $v = 0$ of the singlet ground-state potential $X^1\Sigma^+$ (not shown for $2(0)^+$). The near-threshold excited states have good transition dipoles only to the near-threshold electronic ground state, e.g. $v = -1$, not $v = 0$. Therefore, to transfer from $v = -1$ to $v = 0$, we need to choose an excited state in the deeply bound regime. For transfer to both the singlet and the triplet rovibrational ground state, we chose two different vibrational levels that are associated with $3(1)$ (or associated with $3(0)$, which is the same potential but characterized by $\Omega = 0$). The larger transition dipole moment from $3(1)$ to $v = 0$ of $X^1\Sigma^+$ seems too good to be true. It turned out to be a factor of 20 smaller (400 smaller in d^2), but still had the same qualitative pattern as a function of excited-state energy. However, the reduced magnitude was still sufficient to enable efficient transfer (Chapter 8)! All transition dipole moments shown here were calculated by S. Kotochigova.

to label the potentials as $3(0)^-$ and $3(1)$ (Fig. 5.1). Since the two components share the same potential, their vibrational level spacings and their wavefunction overlap to the electronic ground states are similar. However, their electric dipole transitions are not the same because of angular momentum selection rules. For molecular state transfer to the triplet electronic ground state, both $\Omega = 0^-$ and $\Omega = 1$ will work. However, for transfer to the singlet electronic ground state, only the $\Omega = 1$ component will have singlet-triplet mixing due to perturbations that come from the $1^1\Pi$ ($\Omega = 1$) potential [99]. Since $1^1\Pi$ lies above $2^3\Sigma^+$, we expect that the $\Omega = 1$ component of $2^3\Sigma^+$ to be pushed toward lower energy relatively to the $\Omega = 0^-$ component. The splitting between $\Omega = 0^-$ and 1 is the second-order spin-orbit coupling that was calculated in [99]. Because only the $\Omega = 1$ component will couple to the singlet electronic ground state, it is crucial to spectroscopically distinguish the two components. Again by using loss spectra of Feshbach molecules after driving bound-bound transitions, we can identify these series. Table 5.2 summarizes all of our observed levels of $2^3\Sigma^+$.

5.4.1 $v' = 10$ of $2^3\Sigma^+$ ($\Omega = 0^-$)

During our first search for $2^3\Sigma^+$ levels, we identified $v' = 8 - 12$ of $2^3\Sigma^+$ ($\Omega = 0^-$). Because the Feshbach molecule wavefunction has lots of oscillations in the small internuclear separation region, we observed strong variations in the transition dipole moment as shown in Fig. 5.6. We chose the $v' = 10$ level as our intermediate state for transfer to the triplet rovibrational ground state (Chapter 7). We have also scanned in more detail the $v' = 10$ level and observed several hyperfine lines that served as intermediate states to access different hyperfine states of the triplet rovibrational ground state (Fig. 5.7). For the triplet rovibrational ground-state molecules, we measured their permanent electric dipole moment by measuring the level Stark shift when applying an electric field (Chapter 7.3). The

v'	$\Omega = 1$ (GHz)	$\Omega = 0^-$ (GHz)
8	290359.5	290406.764
9	291709.7	291758.052
10	293049.5	293099.603
11		294431.403
12		295753.57
13	297012	297066
14		
15	299604	
16	300890	
17	302158	
18	303425	
19	304685	304756
20	305949	306033
21		
22	308352	308438
23	309601.4	309707.6

Table 5.2: Summary of observed vibrational levels for both the $\Omega = 0^-$ and 1 components of $2^3\Sigma^+$.

KRb* states are also Stark shifted with electric fields. In Fig. 5.8, the measured Stark shifts of the line that has a transition frequency ~ 293104.055 GHz from Feshbach molecules are listed.

Finally, we calibrated the transition dipole moment from Feshbach molecules to $v' = 10$ of the $2^3\Sigma^+$ electronically excited potential by using both power-broadened lineshapes and a measured one-photon excitation rate. We consider our system as an open coupled two-level system shown in the cartoon drawing of Fig. 5.9(b). Feshbach molecules are driven to KRb* by a laser with Rabi frequency Ω and KRb* then subsequently spontaneously decays with a rate γ . This decay is assumed to populate levels that are outside of the two-level system, hence is lost. We describe our system mathematically by $H = \frac{\hbar}{2} \begin{bmatrix} 0 & \Omega/2 \\ \Omega/2 & \Delta - i\gamma/2 \end{bmatrix}$.

We first measured power-broadened lineshapes (Fig. 5.9(a)) by scanning

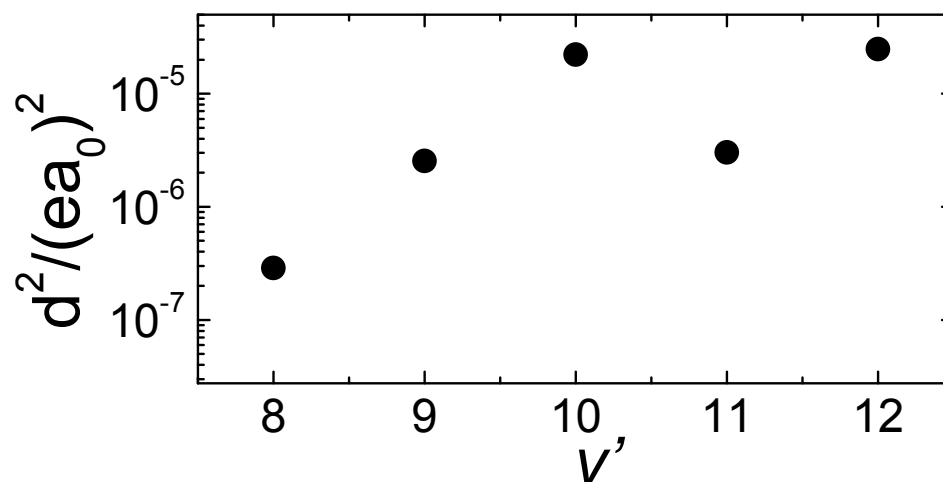


Figure 5.6: Nodal pattern of the transition from Feshbach molecules to different vibrational levels, v' , of the $2^3\Sigma^+$ ($\Omega = 0$) potential.

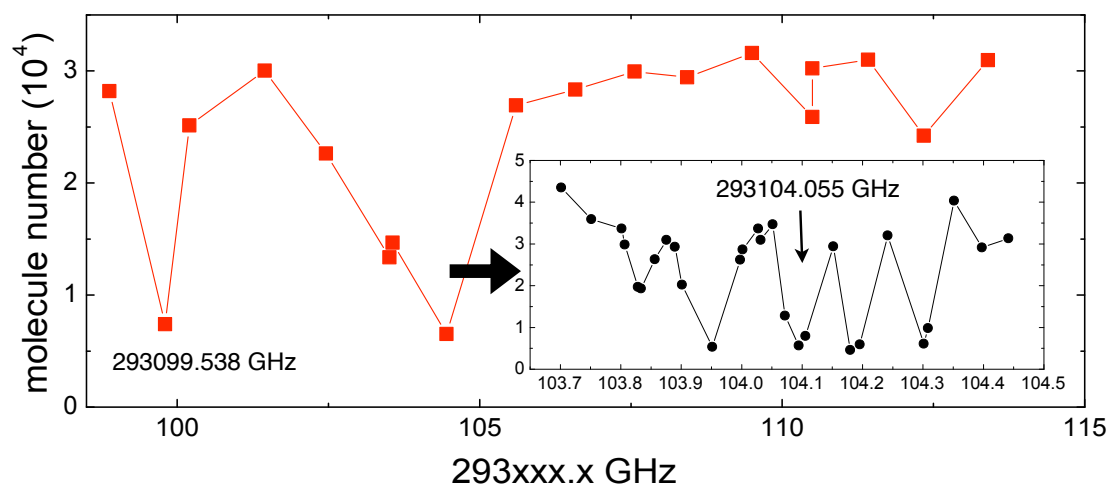


Figure 5.7: Detail of the structure of $v' = 10$ of $2^3\Sigma^+$ ($\Omega = 0$). The two lines we used to accessed different hyperfine states of the triplet rovibrational ground states are the ones with transition frequencies of 293099.538 GHz and 293104.055 GHz from Feshbach molecules. These specific frequencies are derived from referencing the Ti-Sa laser to a stable optical frequency comb. The coarse frequency scale on the y-axis were reading from a wavemeter. (Inset) Detailed structure of the strong line centered at 293104 GHz.

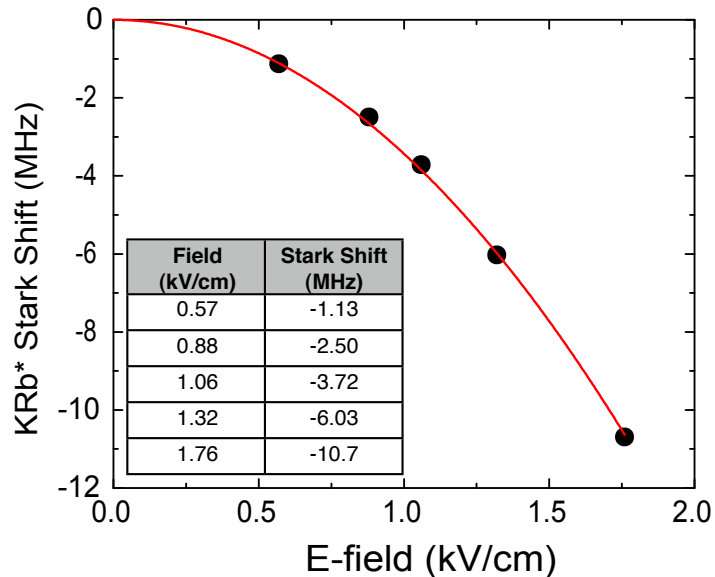


Figure 5.8: Stark shift of the $v' = 10$ of $2^3\Sigma^+$ ($\Omega = 0^-$) state of KRb^* . This line that has a transition frequency ~ 293104.055 GHz from Feshbach molecules at zero electric field.

the laser detuning Δ from the resonance. For these measurements, we used three different laser intensities (corresponding to three different Rabi frequencies Ω , with $\sqrt{I} \propto \Omega$) and a light pulse duration of $20 \mu\text{s}$. The power-broadened lineshapes for an open system is different from a closed system in that when $\Omega > \gamma$, the lineshape is not Lorentzian but rather has a flat bottom loss spectrum (see the red curve in Fig. 5.9(a)). This can be exactly modeled by solving the given Hamiltonian for an open two-level system. The lineshapes give us information about $\frac{\Omega}{\Gamma}$. To get Ω and Γ independently, we fixed $\Delta = 0$ and pulsed on the laser for various times to watch the Feshbach molecule signal decay due to KRb^* creation (Fig. 5.9(b)). The exponential time scale is $\propto \frac{\Gamma}{\Omega^2}$. Together, we obtain $\Gamma = 6.7$ MHz (real frequency and not angular frequency) and Ω . Knowing the laser intensity that corresponding to a specific Rabi frequency Ω and $(\text{dipole moment}/(ea_0)) = \Omega/(10^9)/(0.22068)/\sqrt{I}$, where Ω is in angular frequency, and I is in W/cm^2 , we obtained that the transition dipole moment to be $0.004(2) ea_0$.

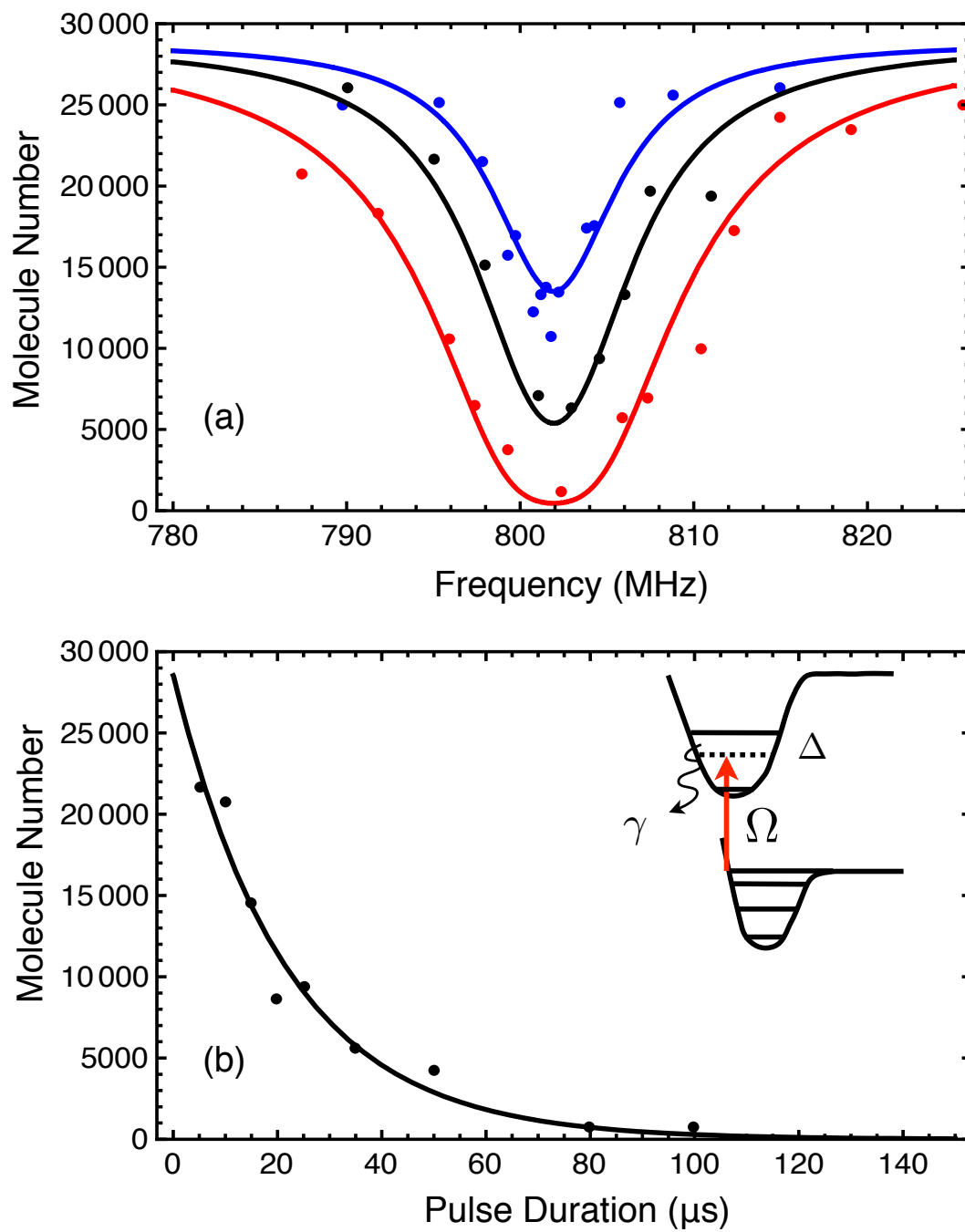


Figure 5.9: Calibration of transition dipole moment from (a) power-broadened lineshapes and (b) one-photon molecular loss time scale.

5.4.2 $v' = 23$ of $2^3\Sigma^+$ ($\Omega = 1$)

For two-photon transfer from Feshbach molecules to the singlet rovibrational ground state, we chose $v' = 23$ of $2^3\Sigma^+$ ($\Omega = 1$). Originally, we wanted to use a higher level, $v' \sim 34$, for the state transfer because the predicted transition dipole moment to the singlet rovibrational ground-state was the largest. However, since the vibrational levels become quite irregular in this regime due to perturbations from three different potentials, we decided to cease the search for higher v' and to try $v' = 23$. This worked!

Again this level has hyperfine structure. We have characterized three of the states and these are summarized in Table 5.3. Each line can only be driven from Feshbach molecules using a specific circular polarization. We do not identify or assign their hyperfine quantum number. In addition, we have calibrated the transition dipole moment from Feshbach molecules using the method described in the last section. This was performed using Raman lasers with 50/50 mixture of σ^+ and σ^- light. We measured the transition dipole moment of the line corresponding to transition frequency of 309602.851 GHz to be $0.005(2) ea_0$. Finally, the Stark shift of the same line is shown in Fig. 5.10.

Transition freq from Feshbach Molecules	polarization	ground hyperfine-state coupling
309602.753 GHz	σ^+	$ -4, 1/2\rangle$
309601.737 GHz	σ^-	$ -4, 1/2\rangle, -3, -1/2\rangle, -4, -3/2\rangle$
309600.656 GHz	σ^-	$ -4, 1/2\rangle, -3, -1/2\rangle, -4, -3/2\rangle$

Table 5.3: Summary of three hyperfine lines of the $v' = 23$ level of the $2^3\Sigma^+$ ($\Omega = 1$) potential. Each state can only be driven from Feshbach molecules using a specific circular polarization light. In addition, each state can couple to specific hyperfine states (hyperfine state labeling notation is discussed in Chapter 9) of the ro-vibronic ground state through a two-photon transition from Feshbach molecules.

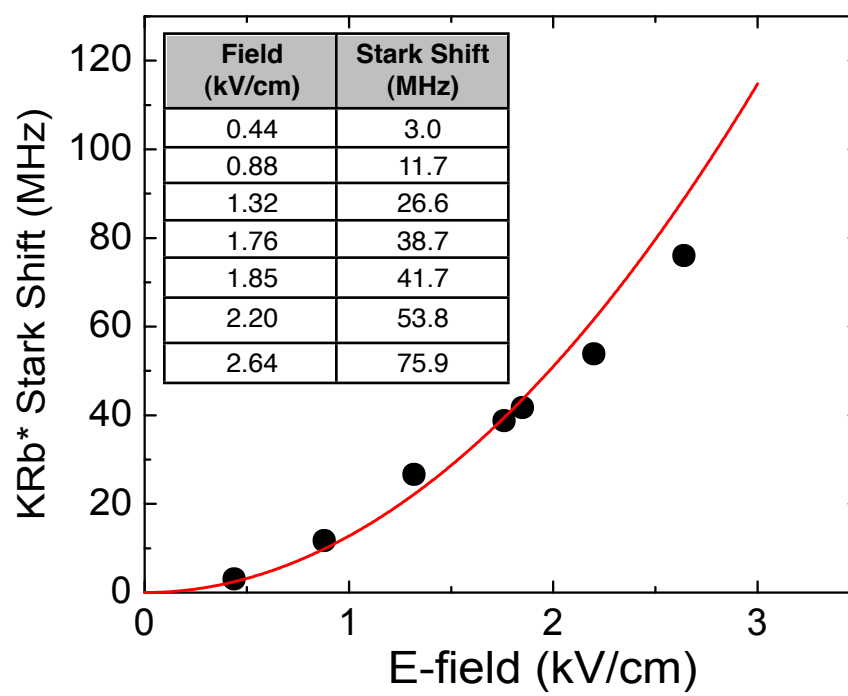


Figure 5.10: Stark shift of the $v'=23$ of $2^3\Sigma^+$ ($\Omega = 1$). This specific line has a transition frequency ~ 309602.753 GHz from Feshbach molecules at zero electric field. The line is for guides of the eyes.

Chapter 6

Coherent Two-Photon Raman Transfer

Using coherent methods to transfer atoms to tightly bound molecules has the advantage that the transfer is state-selective, efficient, and can take away the binding energy through the applied transfer fields (either magnetic fields, electric fields, or laser fields). In Chapter 4, I have already introduced the first coherent transfer method, which creates Feshbach molecules from atoms through an adiabatic magnetic-field ramp across a Fano-Feshbach resonance. In this chapter, I will introduce the second coherent method, which we use to shrink the molecule size. The discussion follows work in [26, 100].

Making high vibrational level (high- v) molecules from a BEC of atoms using a coherent Raman transition was first demonstrated with Rb_2 by Wynar *et al.* in 2000 [101]. Using a molecular signal that came from loss of atoms immediately after the Raman pulse transfer, they were able to determine the binding energy of the molecules along with the condensate mean-field energy precisely. In 2007, Winkler *et al.* [25] had extended the coherent transfer idea to a more robust method, namely, STImulated Raman Adiabatic Passage (STIRAP) [102], and transferred Rb_2 Feshbach molecules to the $v = -2$ level ($h \cdot 637$ MHz bound) with 87% efficiency. Here, the minus sign on the vibrational level refers to counting the level from the atomic threshold, e.g. $v = -1$ would be the least bound level.

As STIRAP having been demonstrated for efficient state transfer for homonu-

clear molecules to $v = -2$, we were certain that the same would work for our heteronuclear molecules, KRb. However, the final goal was to make polar molecules, which means that the KRb molecules would have to be tightly bound. Furthermore, the $v = 0$ level (counting v here from the bottom of the potential) seems special, since it is the lowest energy level and should be maximally stable. The big challenge would then be applying the STIRAP technique to transfer molecules between vibrational levels with very different sizes.

Here, I will introduce the two-photon Raman transfer technique by first discussing transfer from Feshbach molecules to a high- v level, in particular $v = -3$. In subsequent chapters, I will describe how we extend the technique to reach the absolute ground state.

6.1 Three-level System

Fully coherent manipulation is the key to efficient transfer molecules between different vibrational levels. Our transfer technique uses three molecular states, labelled $|i\rangle$, $|e\rangle$, and $|g\rangle$, that are coupled together by two laser fields, Ω_1 and Ω_2 , as shown in Fig. 6.1. Since the excited state $|e\rangle$ is usually lossy and short-lived, we introduce a decay rate γ for the state $|e\rangle$. In general, states $|i\rangle$ (the Feshbach molecule state) and $|g\rangle$ (the target vibrational state) can also decay, but this will be ignored since the time scale is usually much longer than the transfer process in consideration. The simplified Hamiltonian of the system, after making the rotating-wave approximation, in the basis of $|i\rangle$, $|e\rangle$, and $|g\rangle$ is

$$H = \frac{\hbar}{2} \begin{bmatrix} 0 & \Omega_1(t) & 0 \\ \Omega_1(t) & 2\Delta - i\gamma & \Omega_2(t) \\ 0 & \Omega_2(t) & 2\delta \end{bmatrix}, \quad (6.1)$$

where Δ denotes the one-photon detuning and δ denotes the two-photon detuning shown in Fig. 6.1. When the Raman resonance condition is met, namely $\delta = 0$, one of the eigenstates of the system is $\cos\theta |i\rangle + \sin\theta |g\rangle$ where $\theta = \tan^{-1}(\frac{\Omega_1(t)}{\Omega_2(t)})$. This state is dark in that it does not couple to the lossy $|e\rangle$ level. This dark state is important because it allows, with an appropriate time dependence of the applied coupling fields $\Omega_1(t)$ and $\Omega_2(t)$, the full population of $|i\rangle$ to be converted to $|g\rangle$ without ever populating the lossy excited state $|e\rangle$. This process is called STIRAP and it provides fully coherent transfer between states $|i\rangle$ and $|g\rangle$ [102]. It is important to note that we have assumed that there is a well-defined phase relation between the two coupling fields. This assumption sets a challenging requirement for lasers that couple states that are very different in binding energy.

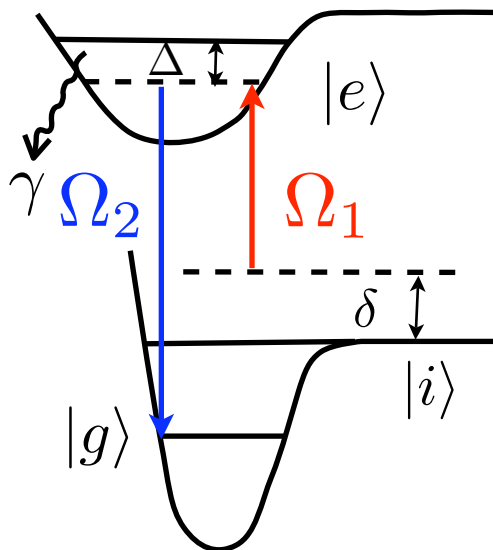


Figure 6.1: Open three-level system. The three states labelled by $|i\rangle$, $|e\rangle$, $|g\rangle$, are coupled by two laser fields, Ω_1 and Ω_2 . The two laser frequencies are detuned from $|e\rangle$ by Δ (one-photon detuning). The frequency difference between two lasers is detuned from the energy difference of $|i\rangle$ and $|g\rangle$ by δ (two-photon detuning). The excited state $|e\rangle$ is short-lived with an decay rate γ that corresponds to a loss rate from the three-level system.

For the first experiment, we demonstrated transfer of weakly bound Feshbach molecules with a size of the order $300 a_0$ (binding energy $\sim h \cdot 240$ kHz) to another weakly bound state, $v = -3$, that has a size of $34 a_0$ and a binding energy of $\sim h \cdot 10$ GHz. To do this, we identified an intermediate state that bridges the wavefunction difference. As we have already seen in Chapter 5.2, the vibrational level structure for the KRb excited molecular potentials near the atomic 4S+5P threshold is very complicated. In particular, the level that associated with $\Omega = 1$, e.g. $2(1)$, have rich hyperfine structure within a 3 GHz-span around each vibrational level at a magnetic field of 546 G. These nearby lines will make it difficult to find an isolated three-level system and allow off-resonance excitations. Therefore, we pick an intermediate state that is associated with a potential that has $\Omega = 0$, which greatly simplifies the hyperfine structure. The particular intermediate state we chose was $v' = -14$ of $2(0^-)$, which has a very simple structure (see Fig. 5.3) with individual lines that are spaced by at least ~ 1 GHz.

To transfer population from Feshbach molecules to a high- v level via the chosen excited intermediate state, some knowledge of selection rules is helpful. First, our Feshbach molecules are 80% triplet (total electronic spin $S = 1$) in character [89], therefore, it is more favorable for transferring them into vibrational levels of the triplet electronic ground potential, $a^3\Sigma^+$. In addition, molecules in a high- v level are expected to have a hyperfine structure similar to the atomic hyperfine structure at the same magnetic field (Fig. 6.2). Therefore, we label the high- v levels by the same atomic hyperfine quantum numbers. For example, KRb in $v = -3$ with $K|9/2, -9/2\rangle + Rb|1, 1\rangle$ character is labelled $aa(-3)$ (using the same notation introduced in Chapter 4.1.1. or [89]). KRb in $v = -4$ with $K|7/2, -7/2\rangle + Rb|1, 0\rangle$ character is labelled $rb(-4)$. Since our Feshbach molecules are $\sim 65\%$ in the “ aa ” open channel and $\sim 35\%$ in the “ $rb(-2)$ ” closed channel, the two-photon Raman transition will mostly likely only couple strongly to high- v levels with “ aa ” or “ rb ”

character [88]. Therefore, we only looked for vibrational states associated with $aa(v)$ and $rb(v)$. In addition, the hyperfine quantum numbers of the intermediate state can impose additional selection rules. Since the intermediate state hyperfine quantum number is harder to assign, we test the intermediate states empirically.

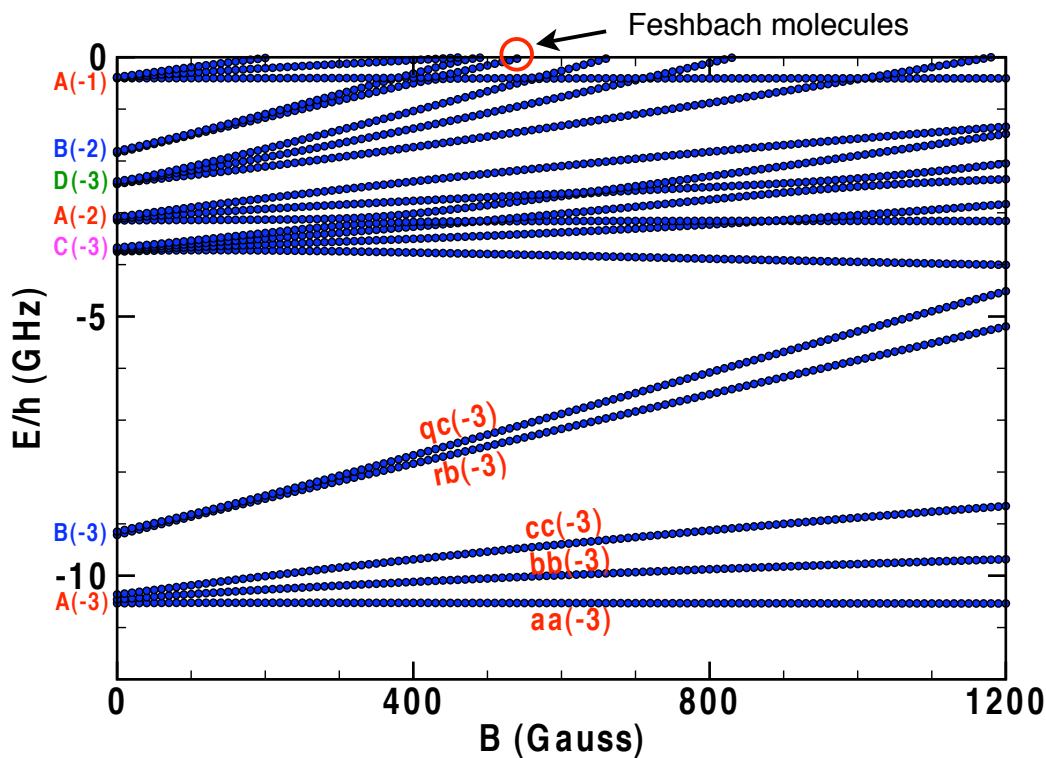


Figure 6.2: KRb high- v molecular levels vs magnetic field. Molecular vibrational levels near the atomic threshold have a hyperfine structure derived from atomic ones. Here all energy are referenced to the atomic threshold of $K|9/2, -9/2\rangle + Rb|1, 1\rangle$. Each molecular level can be labelled by its hyperfine quantum numbers and its vibrational quantum number. For example, KRb in $v = -3$ with $K|9/2, -9/2\rangle + Rb|1, 1\rangle$ character is labelled by $aa(-3)$. Figure courtesy of P. Julienne (2007).

6.2 Dark Resonance

Before performing STIRAP to coherently transfer population from the Feshbach molecule state to a desired target vibrational level, we first need to precisely

determine the energy of the target vibrational state. We did this using two-photon dark resonance spectroscopy. Recall that there exists a dark state, as discussed above, $\cos\theta |i\rangle + \sin\theta |g\rangle$ where $\theta = \tan^{-1}(\frac{\Omega_1(t)}{\Omega_2(t)})$, when the two-photon Raman resonance condition is fulfilled. In the limit of $\Omega_2 \gg \Omega_1$, the dark state becomes $|i\rangle$, and therefore no loss is expected for $|i\rangle$ when $\delta = 0$.

To search for a particular near-threshold vibrational level in the electronically ground potential, we fixed the frequency of the laser corresponding to Ω_1 to resonantly drive Feshbach molecules to the electronically excited intermediate state. Then we scanned the Ω_2 laser frequency and monitored the population of the Feshbach molecules, after pulsing on both lasers. For this case of near-threshold transfer, the beat frequency of the two Raman lasers is measured using a photodiode and then phase-locked to a stable microwave source. In the absence of Ω_2 , the Feshbach molecules disappear because they are resonantly excited by the Ω_1 laser field. These excited molecules will decay by spontaneous emission into a large number of molecular and atomic states and are lost from our signal, which comes exclusively from the weakly bound Feshbach molecules. However, when the second laser field, Ω_2 , fulfills the Raman resonance condition, $\delta = 0$, the Feshbach molecules remain due to the formation of the dark state. Measuring this dark resonance position then gives the energy difference between the initial state $|i\rangle$ and the target state $|g\rangle$. However, strictly speaking, the exact binding energy is determined only when the Raman condition is fulfilled in the limit of $\Omega_1 \ll \Omega_2$. When Ω_1 is not $\ll \Omega_2$, the dark resonance position will be slightly Stark-shifted by the corresponding to laser field Ω_1 . Therefore, to precisely determine the binding energy, we performed dark spectroscopy with various Ω_1 laser powers and extrapolated the energy corresponded to zero Ω_1 laser power. From this measurement, the binding energy of $aa(-3)$ was precisely determined to be $h \cdot 10.49238(15)$ GHz at $545.88(5)$ G [26]. We have also probed other states, such

as $aa(-2)$ and $rb(-3)$, and summarize their binding energies in Table 6.1.

v	binding energy/ h	theoretical prediction/ h
$aa(-2)$	3.1504(10) GHz	3.1510 GHz
$rb(-3)$	7.31452(15) GHz	7.3187 GHz
$aa(-3)$	10.49238(15) GHz	10.4976 GHz
$rb(-4)$	21.547(1) GHz	21.5661 GHz

Table 6.1: Summary of the observed high- v levels and a comparison with the theoretical predicted values from P. Julienne. ($rb(-4)$ was measured using a different phase-locked Raman laser system involving referencing the two lasers to a frequency comb).

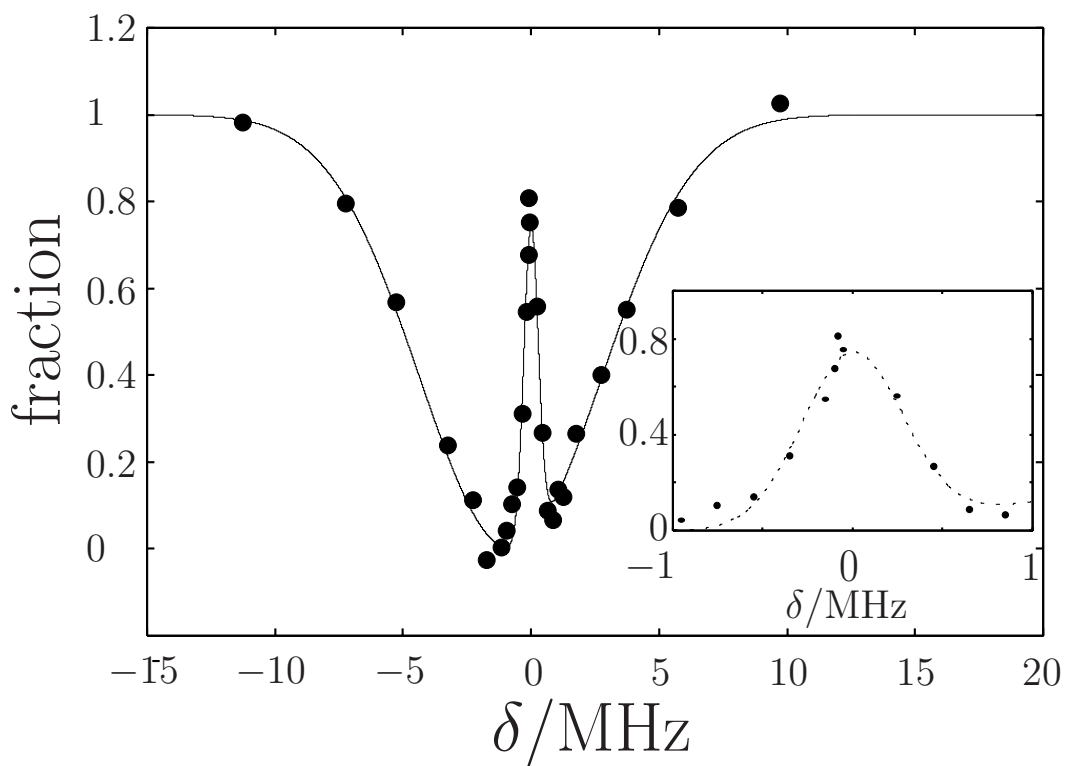


Figure 6.3: A typical dark resonance spectrum, shown for $rb(-3)$. The asymmetry of the lineshape comes from the one-photon detuning not being exactly zero. (Inset) A zoomed in of the dark resonance feature.

The two-photon dark resonance can also be used to characterize the transition coupling strength. Here, we take a scan of $rb(-3)$ as an example. The dark-resonance scan (Fig. 6.3) was achieved by scanning the Ω_1 laser frequency while

fixing the laser frequency of Ω_2 on resonance ($\Delta = 0$). We observed a one-photon loss feature with a Lorentzian width of ~ 6 MHz and a narrow dark-resonance feature by definition at $\delta = 0$. The splitting of the two minima corresponds to the Rabi frequency Ω_2 .

6.3 Detuned STIRAP, $v = -3$

Once the precise location of $aa(-3)$ was determined, we used STIRAP [102] to transfer KRb Feshbach molecules into $aa(-3)$. As discussed above, when the two-photon detuning $\delta = 0$ is maintained, the population of $|i\rangle$ can be adiabatically transferred to $|g\rangle$ by an appropriate choice for the time dependence of the coupling laser fields with corresponding Rabi frequencies $\Omega_1(t)$ and $\Omega_2(t)$. Figure 6.4(a) shows the counter-intuitive STIRAP pulse sequence used in the experiment. First, we turned on Ω_2 (corresponding laser intensity I_2) to couple $|e\rangle$ and $|g\rangle$. While the intensity of I_2 is ramped down from I_2^{max} to 0 within $\tau_p = 20 \mu\text{s}$, the intensity of I_1 (corresponding Rabi frequency Ω_1) is ramped up from 0 to I_1^{max} , thereby adiabatically transferring Feshbach molecules to the target state, without ever populating the lossy intermediate state $|e\rangle$. At the end of the STIRAP transfer, I_1 can be turned off. Reversing the pulse sequence in time reverses the transfer process from $|g\rangle$ to $|i\rangle$.

Figure 6.4(b) shows STIRAP transfer of KRb from the weakly bound Feshbach molecule state to $aa(-3)$ using the pulse sequence in Fig. 6.4(a). Since we only detect population in the initial Feshbach molecule state, we also perform a reverse STIRAP pulse sequence to bring the deeply bound molecules back to the Feshbach molecule state for detection. For the data in Fig. 6.4(b), the round-trip transfer has an efficiency of 71%. Assuming equal efficiency each way, the one-way STIRAP transfer efficiency is 84%.

So far, we have emphasized that efficient STIRAP transfer requires main-

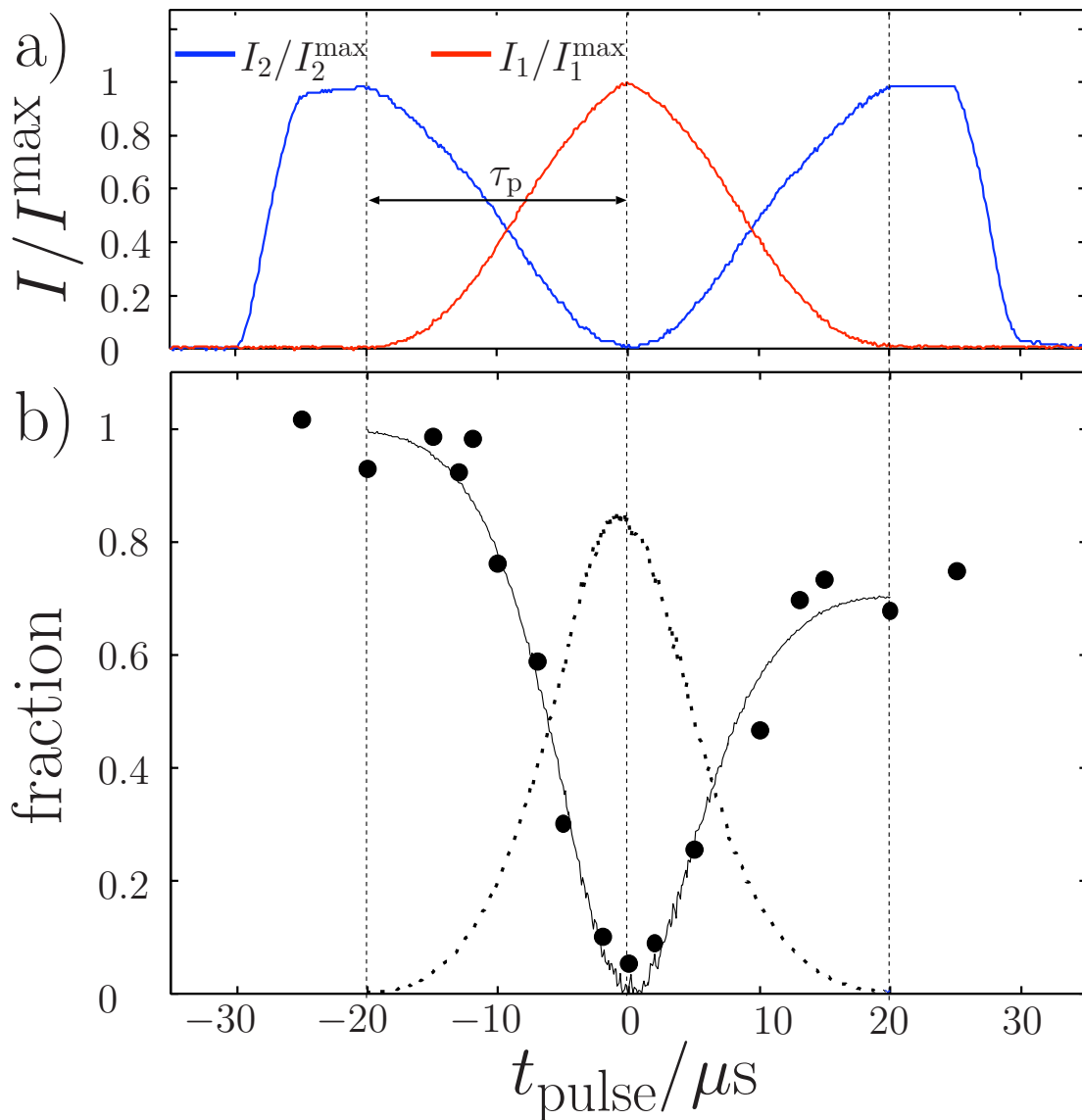


Figure 6.4: Population transfer from Feshbach molecules to $aa(-3)$ using a coherent two-photon STIRAP transfer technique. (a) Laser intensity pulse sequence normalized to their individual intensity maximums. The counter-intuitive sequence is to turn I_2 on first, ramp it down while ramping I_1 up. The second half of the sequence is for a reversed STIRAP process. (b) Population transfer corresponding to the pulse sequence in a. The data is shown as the fraction of population in the Feshbach molecule state. The dashed line is the corresponding population in the target state, $aa(-3)$. The lines are fits to the data using the model based on equation 6.1.

taining $\delta = 0$. But we have not yet discussed the one-photon detuning, Δ . Using a transfer model based on equation 6.1, it is easy to show that any Δ works provided that Δ is not so large such that the laser coupling strengths between states drop significantly for accessible laser powers. The most straightforward thing is to perform STIRAP at $\Delta = 0$. However, there are certain advantages of performing STIRAP at $\Delta \neq 0$. For example, since a STIRAP lineshape is in general much narrower than a dark resonance lineshape and we look for loss of initial-state population in our one-way STIRAP signal, performing detuned STIRAP (Fig. 6.6) enables us to find the target state location more precisely. (In the case when $\Delta = 0$, one-way STIRAP lineshape will show loss which could be either real loss or transfer to a “dark” state for the entire scanned range of δ .)

One interesting feature of detuned STIRAP is that the resonant position can move depending on imbalanced Stark shifts from the coupling laser fields and the sign of the detuning. These can all be understood in a model based on the Hamiltonian given equation 6.1. Therefore, by performing detuned STIRAP with both positive and negative Δ and various intensity ratios of the coupling lasers, we can determine the unperturbed $\delta = 0$ location along with the laser powers that give the coupling ratio $\Omega_1/\Omega_2 = 1$ (Fig. 6.5). Using the model, we extracted $\Omega_2/\Omega_1 = 1.7 \pm 0.1$ and $\Delta = 50 \pm 5$ MHz for the lineshape shown in Fig. 6.6. Together with the previous measurement of Ω_2 and $I_1^{max}=3.7(1.5)$ W/cm², $I_2^{max}=1.0(0.4)$ W/cm², we obtained the effective transition dipole moments of $d_1=0.050(15)$ ea_0 and $d_2=0.17(4)$ ea_0 .

6.4 Extending STIRAP to Deeply Bound States

With coherent transfer from Feshbach molecules to a near-threshold vibrational state demonstrated for a heteronuclear system, we moved on to finding a way to reach a deeply bound state that has a large permanent electric dipole

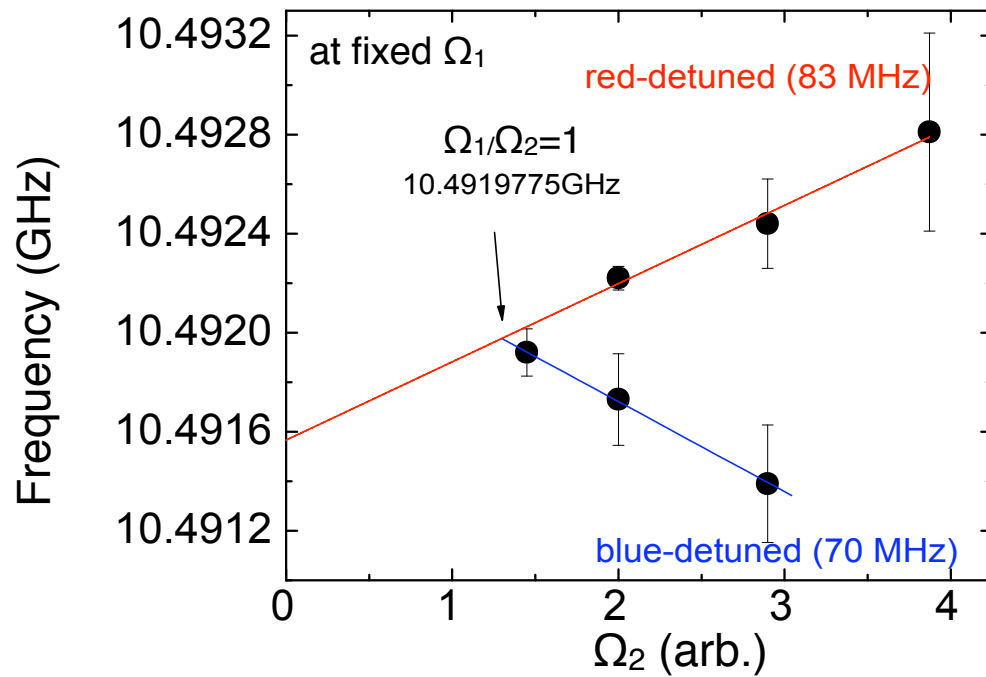


Figure 6.5: AC stark shift measured for the detuned STIRAP resonance. The resonant frequency difference of the two Raman lasers depends on the coupling field strength Ω_2 due to imbalanced laser Rabi frequency. By measuring the STIRAP resonance using blue-detuned and red-detuned STIRAP, we can determine the exact energy difference of the initial and the target state energy (where the lines crosses). The crossing point happens when the two-photon Rabi frequency ratio $\Omega_1/\Omega_2 = 1$, which allows us to extract the transition dipole moment ratio very accurately. To get the binding energy of $aa(-3)$, we add the beat frequency plotted here with the Feshbach molecule binding energy.

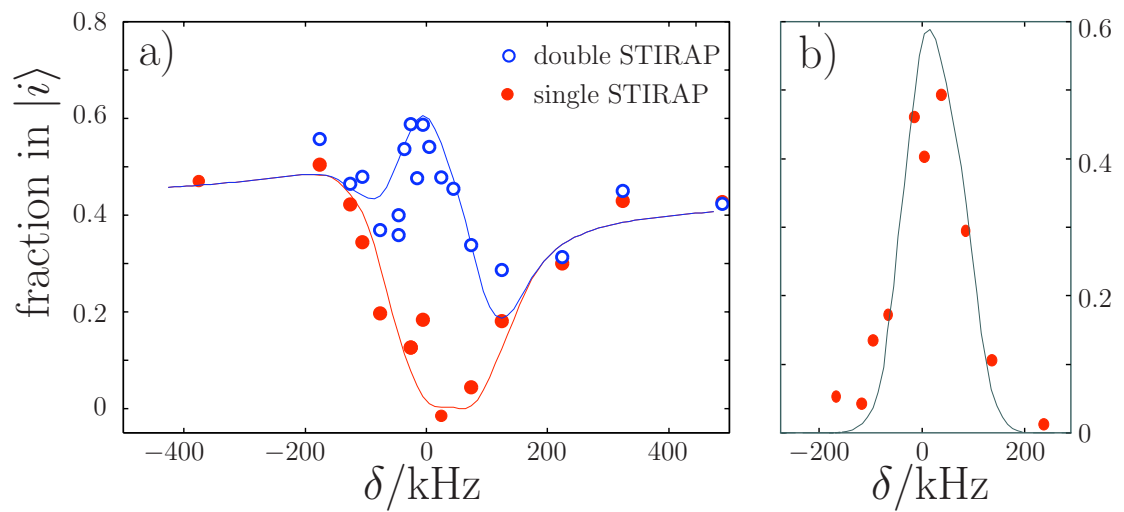


Figure 6.6: Detuned-STIRAP lineshape (a) Fraction of total population in the initial Feshbach molecule state v.s. two-photon detuning after both single STIRAP and round-trip STIRAP. (b) The corresponding population in the $aa(-3)$ state after a single STIRAP.

moment. There were three major challenges. The first was a technical challenge. A “technical” limitation of our first demonstration experiment was that the two Raman lasers were compared using a photodiode to record their beat, which was then phase-locked to a microwave source. This technique is only applicable over a limited frequency range. For example, the bandwidth of the photodiode was limited to 20 GHz. To stabilize two lasers with a large frequency difference, even one in the optical domain, one needs to have a stable reference that can bridge the large difference. Of course, we also need to have new lasers with the desired wavelengths. We used a home-built stable optical frequency comb for our reference. The relevant comb parameters and its setup are described in Chapter 3.3.3.

Once the comb was implemented, we looked for the next vibrational level, $rb(-4) \approx h \cdot 21\text{GHz}$, and found it right away. However, using the same excited intermediate state ($v' = -14$ of $2(0^-)$), the transition dipole moment to deeply bound states decreases by orders of magnitude. The second challenge, as was described in Chapter 5, was then to choose an intermediate state that can bridge the large wavefunction mismatch between Feshbach molecules and a target low- v state. The identification of a suitable intermediate state began with our theoretical collaborators, S. Kotochigova and P. Julienne, who calculated transition dipoles for the vibrational levels of different excited-state potentials to all the vibrational levels in the ground electronic state. We were especially interested in the transition dipole moments from a single excited state to both $v = -1$ (counts down from threshold) and $v = 0$ (counts up from absolute ground state). Based on this, they made suggestions of a few possible “routes” to the low- v levels. We chose a route that used a similar intermediate state as the one used in the photoassociation work by Sage *et al.* [22]. One main reason for this choice was there were some spectroscopic data available in the relevant range for KRb of different isotopes [27]. These relevant vibrational levels are the low- v levels associated

with the $2^3\Sigma^+$ potential and are expected to have good wavefunction overlap to the low- v levels of the electronic ground potentials. Our biggest concern was if we could drive weakly bound Feshbach molecules directly to these low- v levels of $2^3\Sigma^+$ using our experimentally available laser power. Although being slightly skeptical of the relatively large calculated dipole moments for these transitions, we were optimistic because of an observation we made [18] when first trying to create Feshbach molecules. We had seen a “lucky” coincidence where our 1075 nm (linewidth of 1 nm) optical trap laser was causing loss of the Feshbach molecules. This could be because the light was driving Feshbach molecules to perhaps $v' = 0$ of the $2^3\Sigma^+$ potential [18]. Now, we have experimentally identified the low- v series of $2^3\Sigma^+$ as described in Chapter 5.

The final challenge was the potentially large uncertainty of the locations of relevant low- v levels of the electronic ground potential. Our experiment, although it has a high sensitivity and an unprecedented resolution for molecular spectroscopy, has a cycle time of a minute. Therefore, it is not suitable for a large spectroscopy scan. For this reason, we have to understand the uncertainty of the potential in different regions of internuclear separations. (We also care about the same thing for electronic excited-state potentials, which is discussed in Chapter 5.) For the near-threshold region that was accessed in the last section, the uncertainty of the vibrational levels is 1%. If we scale this uncertainty directly to $v = 0$ of $a^3\Sigma^+$ ($h \cdot 7$ THz) or $v = 0$ of $X^1\Sigma^+$ ($h \cdot 125$ THz), it would be 70 GHz or 1 THz (half of the vibrational spacing)! Luckily, Pashov *et al.* [28] constructed very accurate KRb ground-state potentials for both the triplet and the singlet potentials using conventional spectroscopy of $^{39}\text{K}^{85}\text{Rb}$ low- v states and matching this with comprehensive Feshbach resonance data near the atomic threshold. After using mass-scaling to calculate the vibrational series for $^{40}\text{K}^{87}\text{Rb}$, the uncertainty is expected to be ~ 7 GHz for the triplet ground state and ~ 10 GHz for the

singlet ground state. One side note is that since not all the “intermediate”- v were mapped out, the uncertainty in the intermediate region would be much higher.

After understanding the uncertainties of all v -states and solving the first two challenges, we decided that instead of following a vibrational series from the near-threshold region to the low- v region, we would directly jump to searching for a $v = 0$ state. In particular, since going to the singlet $v = 0$ level requires additional singlet-triplet mixing of the excited electronic state, we went for $v = 0$ of the $a^3\Sigma^+$ potential first.

Chapter 7

Triplet Rovibrational Ground-State Molecules

($N = 0, v = 0$ of $a^3\Sigma^+$)

After demonstrating molecular state transfer to near-threshold vibrational levels, we decided to move quickly toward attempting to transfer Feshbach molecules to a low- v state directly. In this chapter, I will show that by carefully choosing an intermediate excited state, we can coherently transfer Feshbach molecules to the rovibrational ground state of $a^3\Sigma^+$ in a *single*-step of STIRAP. The discussion here is based on our publication in [15].

7.1 Scheme

Our goal here is to coherently transfer molecules from the initial Feshbach molecule state, $|i\rangle$, to the triplet rovibrational ground state, $|g\rangle$ ($N = 0, v = 0$ of $a^3\Sigma^+$) (Fig. 7.1). The strength of the transition dipole moment between states comes from both the electronic transition dipole moment and the wave function overlap, i.e. Franck-Condon Factor (FCF). Since both the initial and the final states are predominately triplet in character, we chose a triplet intermediate excited state, $|e\rangle$ ($v' = 10$ of the electronically excited potential $2^3\Sigma^+$), with a favorable wave function overlap. To choose such a state from a “forest” of excited-state potentials is not an easy task. However, there are guidelines one can follow. When driving electronic transitions, it is typically a good approximation to assume that

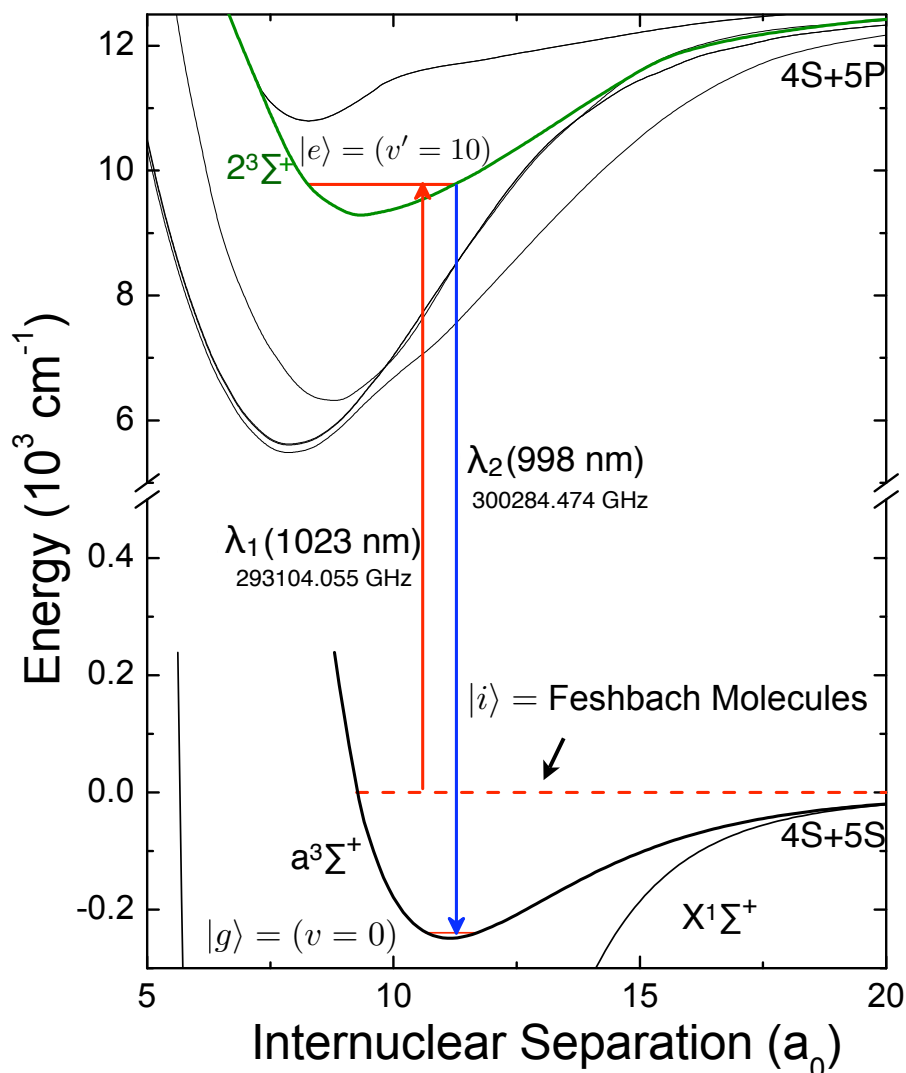


Figure 7.1: Diagram of the KRb electronic ground and excited molecular potentials and the vibrational levels involved in the two-photon coherent state transfer to the triplet ground state. Here, the intermediate state $|e\rangle$ is the $v' = 10$ level of the electronically excited $2^3\Sigma^+$ potential. The vertical arrows are placed at the respective Condon points of the up and down transitions. Note the different energy scales for the excited and the ground potentials. The intermediate state has favorable transition dipole moments for both the up leg ($|i\rangle$ to $|e\rangle$) and the down leg ($|e\rangle$ to $|g\rangle$), where the initial state $|i\rangle$ is a weakly bound Feshbach molecule state and the final state $|g\rangle$ is the rovibrational ground state ($v = 0$, $N = 0$) of the triplet electronic ground potential, $a^3\Sigma^+$. This listed frequencies for the up and down transitions are the most common transitions we used. (These frequencies are the Raman laser frequencies to the molecules and are 98.5 MHz lower from our laser locking point due to an AOM frequency shift, see Chapter 3.3.4. for an operational note.)

the heavy nuclei do not move during the transition (Born-Oppenheimer approximation). Therefore, to estimate the strength of the transition dipole moment, we look at the wave function amplitude at the same internuclear separation. Nuclei in a vibrationally excited state molecule spend most of their time at their inner and outer turning points, thus the wave function amplitude is the largest at these positions. In contrast, nuclei in a vibrationally ground state molecule have the largest amplitude at the center of the potential well. More rigorously, we find favorable transitions using the classical Condon point argument. The Condon point is the internuclear distance where the photon energy matches the difference between the excited and ground-state potential energy curves. Following these guidelines and calculations from our theoretical collaborators, S. Kotochigova and P. Julienne, we began our experimental search and identified $v' = 10$ of $2^3\Sigma^+$ as a suitable intermediate excited state. In our scheme (Fig. 7.1), the first laser field, λ_1 (1023 nm) connects our initial Feshbach molecule state, $|i\rangle$, to the excited intermediate state, $|e\rangle$, and the second laser field, λ_2 (998 nm), drives the down transition to the ground vibrational level of the electronic ground $a^3\Sigma^+$ potential ($|g\rangle$).

7.2 Hyperfine-rich Ground-state Structure

To search for the triplet vibrational ground state ($a^3\Sigma$, $v = 0$), we performed two-photon dark resonance spectroscopy as was introduced in Chapter 6.2 in the limit of a strong Ω_2 and a weak Ω_1 . Based on the KRb potential published by Pashov *et al.* [28], P. Julienne calculated the triplet $v = 0$ binding energy with a predicted uncertainty of 0.1% (7 GHz). Even this small uncertainty made the experimental search challenging since our dark resonance features in the past were at most tens of MHz wide. Nevertheless, we began our search by first fixing the laser frequency of the λ_1 to resonantly drive the transition from the initial

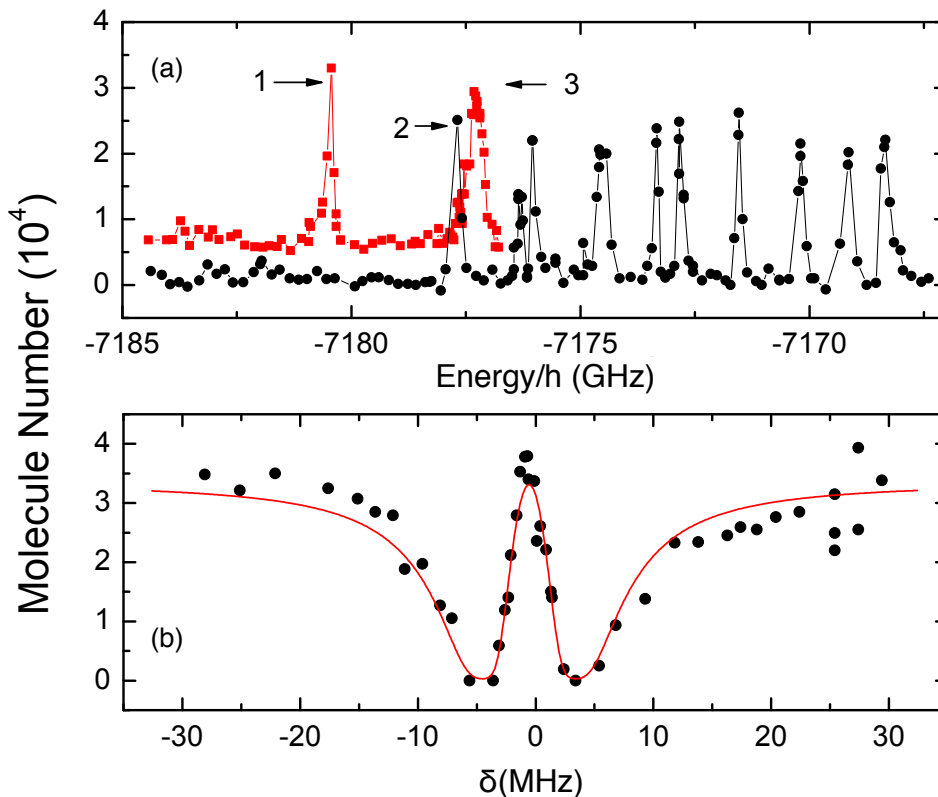


Figure 7.2: The $v = 0$ ground-state level of the triplet electronic ground potential, $a^3\Sigma^+$. (a) Hyperfine and rotational states of the $a^3\Sigma^+$ $v = 0$ ground-state molecule at a magnetic field of 546.94 G, observed using two-photon spectroscopy and scanning the down leg frequency. The measured number of Feshbach molecules is plotted as a function of the frequency difference of the two laser fields. We show two sets of data, vertically offset for clarity, obtained using two different intermediate states, which are ro-hyperfine states of the $v' = 10$ level of the electronically excited $2^3\Sigma^+$ potential. Peaks label 1 and 2 correspond to hyperfine states in the rotational ground-state, while peak 3 corresponds to a rotationally excited state. (b) We precisely determine the energy and the transition dipole moments for individual states using the two-photon spectroscopy where we scan the up leg frequency. The measured number of Feshbach molecules is plotted as a function of the two-photon detuning. The dark resonance shown here is for the triplet rovibrational ground state corresponding to peak 2 in (a).

Feshbach molecule state to the $v' = 10$ intermediate state. The λ_1 laser by itself causes complete loss of all the Feshbach molecules. We then varied the laser frequency of the strong coupling laser (λ_2), and monitored the initial state population after pulsing on both laser fields simultaneously. When the Raman

condition is fulfilled, the initial state population reappears (Fig. 7.2a). To our surprise, pretty much on our first shot, we saw a signal corresponding to the $v = 0$ of the $a^3\Sigma^+$ potential. It turns out that this is because the down transition dipole moment is strong and there is rich hyperfine structure that broadens the $v = 0$ line to be 30 to 50 GHz wide.

The measured binding energy of the triplet $v = 0$ molecules is $h \times 7.18$ THz (corresponding to 240 cm^{-1}) at 545.94 G. We find that the $v = 0$ level has rich hyperfine plus rotational structure at this magnetic field (see Fig. 7.2(a)). Because the accessible final states are influenced by selection rules of the two-photon transition and the quantum number of the intermediate state, we have performed the two-photon spectroscopy using different states of the $v' = 10$ intermediate level (more details on the structure of the intermediate state can be found in Fig. 5.7). In Fig. 7.2(a), the measured hyperfine spectrum of the $v = 0$ triplet ground state is shown for two-photon spectroscopy going through two different states of the $v' = 10$ electronically excited level. The feature labelled peak 1 is the lowest energy state we observed in the $v = 0$ manifold, this state is about 15 GHz less deeply bound than the prediction using potentials from [28]. Interestingly, the construction of the potential [28] comes from mass scaling experimental data of $^{39}\text{K}^{85}\text{Rb}$ starting only at $v = 3$ and higher. Therefore, it is conceivable that the extrapolation to $v = 0$ could introduce some error.

In addition to triplet $v = 0$ molecules, we have also observed similar ground-state hyperfine structure for the $v = 1$ and $v = 2$ levels of the $a^3\Sigma$ state, with $v = 1$ having a binding energy of $h \times 6.675587(1)$ THz and $v = 2$ having a binding energy of $h \times 6.188766(1)$ THz (Here, I give binding energy corresponding to the lowest energy state that we observed.) Combining this information with [28], one should be able to construct the most accurate KRb $a^3\Sigma$ potential to date.

The quantum numbers (hyperfine and rotational) of the states of $v = 0$ could

v	binding energy	$v' = 10$ to v transition dipole moment
0	7.180420(1) THz	0.004(2) ea_0
1	6.675587(1) THz	$\sim 0.004 ea_0$
2	6.188766(1) THz	$\sim 0.004 ea_0$

Table 7.1: Summary of the lowest observed hyperfine state for $v = 0, 1, 2$.

in principle be identified by a careful comparison to theories, e.g. [99]. Here, I identify the rotational quantum numbers of the three lowest energy triplet $v = 0$ states seen in the two-photon spectrum. The peaks labeled 1, 2, and 3 in Fig. 7.2(a) occur at a binding energy of $h \times 7.180420(1)$ THz, $h \times 7.177688(1)$ THz, and $h \times 7.177263(1)$ THz, respectively. Peak 1 corresponds to the lowest hyperfine state in the rotational ground-state ($N = 0$), peak 2 is a different hyperfine state with $N = 0$, and peak 3 is the lowest energy hyperfine state with $N = 2$, where N is the rotational quantum number. This identification is based on Hund's coupling case (b), where spin and molecular rotation are essentially decoupled and the molecular hyperfine structure can be understood from calculations using a separated atom basis with the rotational progression appearing as a constant shift to all hyperfine levels. Because of parity selection rules for optical transitions, we observe only states with even N . The calculated rotational constant is $B = 0.5264$ GHz, which gives a predicted splitting between the $N = 0$ and $N = 2$ levels of $6B = 3.158$ GHz, while the observed splitting of peak 1 and 3 is 3.155 GHz. This assignment will be verified in the next section using Stark spectroscopy.

Finally, using a dark resonance measurement such as shown in Fig. 7.2(b), we have measured the strength of the $|e\rangle$ to $|g\rangle$ transition. Here, we fix the down leg (λ_2) laser frequency and scan the up leg (λ_1) laser frequency. From the width of the dark resonance for the rovibrational triplet ground state (peak 2), we find that we can drive the transition from $v' = 10$ to the triplet $v = 0$ state with a Rabi frequency of $2\pi \cdot 8$ MHz. This measurement used an exceedingly low laser power of

60 μW focused to a beam waist of 55 μm . The transition dipole moment derived from this measurement is 0.20(2) ea_0 , which is only *one* order of magnitude weaker than a typical atomic optical transition!

7.3 Stark Spectroscopy

A quantum gas made of heteronuclear molecules in a low- v state has many exciting new features - one of them is that the particle possesses a significant permanent electric dipole moment that offers new possibilities for control of the quantum gas. KRb molecules in the triplet rovibrational ground state are predicted to have an electric dipole moment of 0.05(3) Debye (D) [94]. This is nine orders of magnitude larger than the calculated $5 \cdot 10^{-11}$ D dipole moment of the initial Feshbach molecules and only about one order of magnitude smaller than a typical polar molecule dipole moment of 1 Debye. To measure the dipole moment, we performed DC Stark spectroscopy on the three lowest energy states observed in the two-photon spectrum (Fig. 7.2(a)). We applied a uniform DC electric field in the range from 0 to 2 kV/cm using a pair of transparent electric-field plates that are separated by 1.35 cm outside the glass-cell based vacuum chamber. A detailed description of the field plates is provided in Chapter 3.2. We measured the Stark shift using the dark resonance spectroscopy discussed above. This two-photon spectroscopy measures the energy splitting between the initial and final states, and because the initial state has a negligible dipole moment, any frequency shift of the dark resonance can be attributed to the final-state Stark shift. For these measurements we lowered the laser powers to give a dark resonance width of 500 kHz. The measured Stark shifts vs electric field are shown in Fig. 7.3.

The effect of a DC electric field is to couple states of opposite parity. For the $a^3\Sigma^+$ $v = 0$ molecules, the opposite parity states are even- N and odd- N rotational states. In Fig. 7.3 we see that the two lowest energy states, which are

the rotational ground state $N = 0$, exhibit similar Stark shifts. From the measured Stark shift, we fit the data by considering rotational state mixing up to $N = 5$ (similar and more detailed analysis can be found in Chapter 8.3 for the singlet vibrational ground state). This yields the molecules' electric dipole moment to be 0.052(2) D. The Stark shift of the third energy state, corresponding to peak 3, is measured to be about 10 times smaller than that for the peak 1 and peak 2 states. This smaller Stark shift for the $N = 2$ state is consistent with an electric dipole moment of 0.052 D.

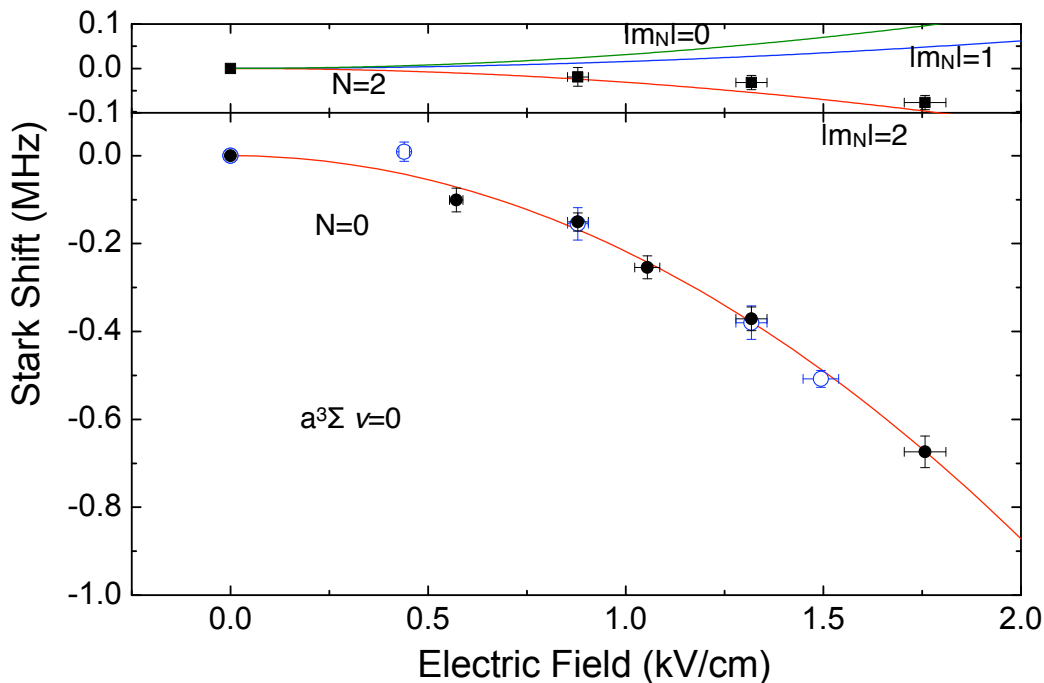


Figure 7.3: Stark spectroscopy of triplet $v = 0$ molecules. Stark shifts of the lowest three states in the triplet $v = 0$ manifold in Fig. 7.2(a) are measured for a DC electric field in the range from 0 to 2 kV/cm. The bottom panel shows the Stark shifts of the two lowest energy states which are $N = 0$. A combined fit to the shifts of peak 1 (solid circles) and peak 2 (open circles) with our main systematic error from a 3% uncertainty of the electric field calculation give an electric dipole moment of 0.052(2) D. The top panel shows the Stark shift of peak 3 (squares) and the expected $N = 2$ curves calculated for an electric dipole moment of 0.052 D and different $|m_N|$ projections.

7.4 Transfer

After our spectroscopy studies of the triplet rovibrational ground state, we performed population transfer. We used peak 2 as the rovibrational ground-state target for our coherent state transfer, which is performed using the counter-intuitive pulse sequence of STIRAP[102] that I have introduced in Chapter 6. The STIRAP beams are co-propagating in order to minimize photon recoil. The measured time evolution of the initial-state population during a double STIRAP pulse sequence is shown in Fig. 7.4(a). The roundtrip transfer efficiency of 31% implies a one-way transfer efficiency of 56%, which corresponds to $3 \cdot 10^4$ triplet $v = 0$ $N = 0$ polar molecules at a peak density of 10^{12} cm^{-3} . This transfer technique allows us to reach a single quantum state without heating. The STIRAP efficiency is limited by the final-state molecule lifetime, which we measured to be $170 \mu\text{s}$ as shown in Fig. 7.4(b). We believe the lifetime is most likely limited by collisions with background atoms, which can induce spin flips and cause molecules to decay into lower lying states in the singlet electronic ground potential. (Collisions and lifetimes of a simpler system, the absolute rovibrational ground-state molecules, will be discussed in Chapter 10.) If so, the collisional decay rate could be reduced either by perfecting the removal of the remaining atoms or by starting the molecule production with atom pairs tightly confined in individual sites of an optical lattice.

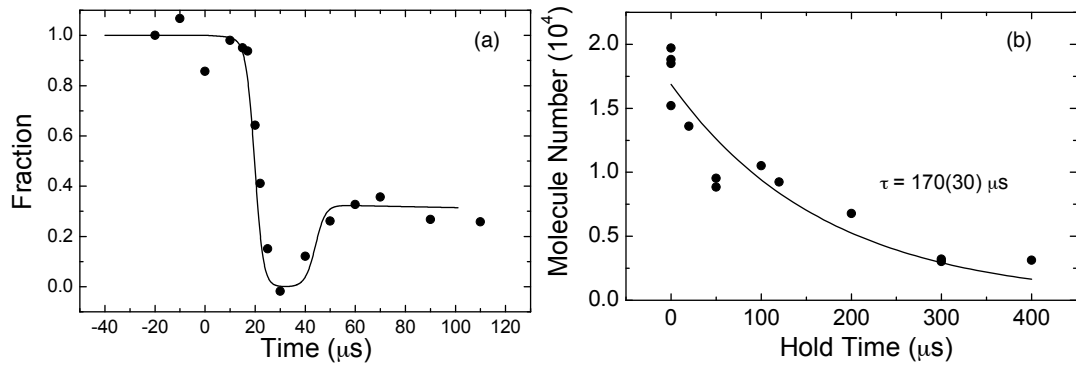


Figure 7.4: Time evolution of the initial state population during STIRAP state transfer and a measurement of the triplet rovibrational ground-state molecule lifetime. (a) Here we monitor the Feshbach molecule population as we apply the STIRAP pulse sequence. Weakly bound Feshbach molecules are coherently transferred into the triplet rovibrational ground state after a 25 μs one-way STIRAP pulse sequence. The measured population completely disappears since the deeply-bound molecules are dark to the imaging light. After a 10 μs hold, we then perform the reversed STIRAP pulse sequence that coherently transfers the ground-state molecules back to Feshbach molecules. The molecule number after the roundtrip STIRAP is $1.8 \cdot 10^4$. Assuming equal transfer efficiency for the two STIRAP sequences, we obtain one-way transfer efficiency of 56% and an absolute number of triplet rovibrational ground-state polar molecules of $3.2 \cdot 10^4$. (b) We measure the triplet $v = 0$ lifetime by varying the hold time after one-way STIRAP before transferring them back to Feshbach molecules for imaging. The lifetime is measured to be 170(30) μs .

The triplet work presented in this chapter provides not only a conceptual but also a physical leap from where we started (see comparison Table 7.2). For a long time, we doubted the feasibility of a *single* transfer step to efficiently bring near-threshold molecules to a low- v state, such as the triplet rovibrational ground state. However, looking back, although the experiment was very challenging, there should have been no conceptual surprise of the result! Propelled by this success, we hoped that transferring molecules to the absolute rovibrational ground state would be a rather straightforward extension. The key is again to identify a suitable intermediate state that not only bridges the larger wave function mismatch but also allows the electronic spin state to change.

	Feshbach molecules	$a^3\Sigma(v = -3)$	$a^3\Sigma(v = 0)$	$X^1\Sigma(v = 0)$
Binding Energy (GHz)	0.00024	10.49238	7180	125313
Size (a_0)	~ 300	34	11.2	7.7
Dipole Moment (Debye)	5×10^{-11}	1×10^{-4}	0.052(2)	0.57(2)
Thesis Chapter	4	6	7 (current)	8 (next)

Table 7.2: Summary of KRb ground-state vibrational level transfers we have demonstrated. The work in this chapter showed a leap in the molecular binding energy and the size (and the corresponding electric dipole moment) from the previous demonstration of near-threshold transfer.

Chapter 8

Absolute Ro-Vibronic Ground-State Polar Molecules

($N = 0, v = 0$ of $X^1\Sigma^+$)

The success of using a *single* step of STIRAP to transfer a large fraction of molecules to the triplet rovibrational ground state motivated us to pursue our long-standing goal – making a high phase-space-density gas of absolute ro-vibronic ground-state molecules ($N = 0, v = 0$ of $X^1\Sigma^+$). The additional challenges were i) to identify one or more intermediate states to bridge the even larger wavefunction mismatch between the Feshbach molecule state and the singlet rovibrational ground state, ii) to have a non-trivial singlet-triplet mixing in the intermediate excited state, iii) to build new lasers at the appropriate wavelengths, and iv) to phase-reference and stabilize the two continuous-wave coupling lasers, which have a much larger frequency difference.

Before our work, most people believed that multiple transfer steps would be required to bridge the large wavefunction mismatch between Feshbach molecules and the absolute ground state. However, as we demonstrated for KRb [15], this turned out not to be necessary. For other bi-alkali heteronuclear molecules, we also expect that a single excited electronic state can be identified that has relatively strong transition strengths to both the initial Feshbach molecule state and the absolute ground state [103]. This chapter follows discussions in [15, 104, 100].

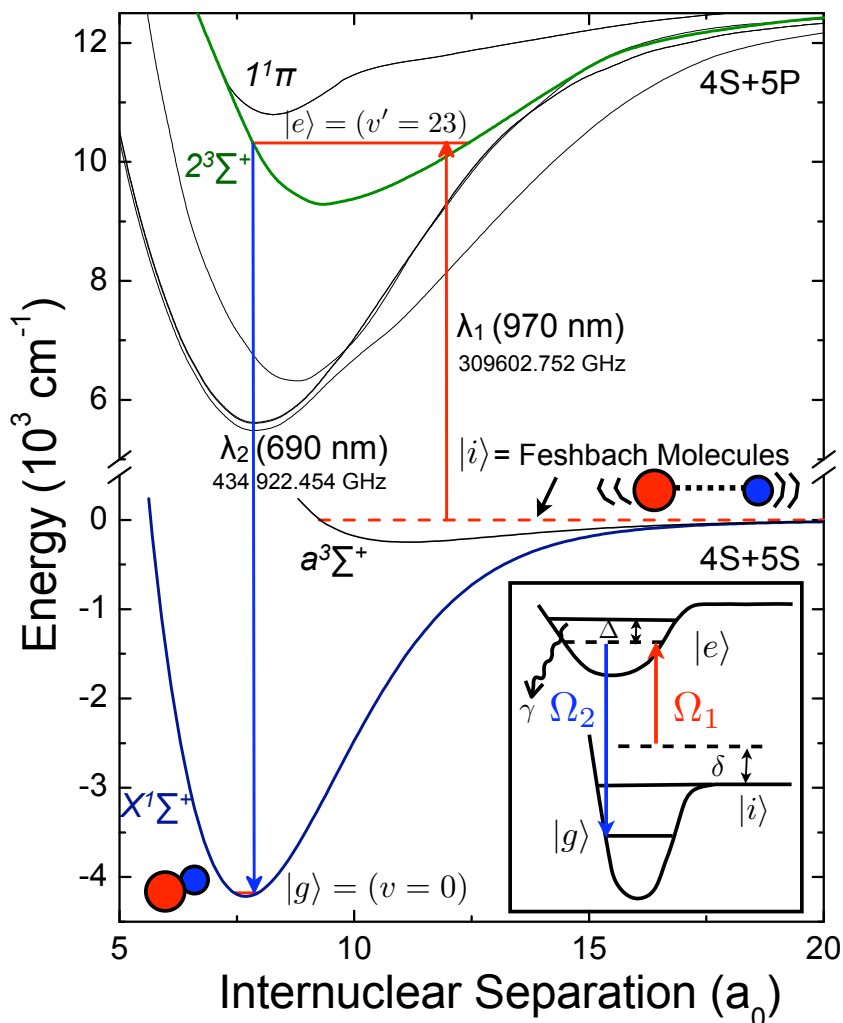


Figure 8.1: Schematic of the transfer from KRb Feshbach molecules to the absolute rovibrational electronic ground state. The intermediate state was chosen to be the $v' = 23$ state of the nominally $2^3\Sigma^+$ electronically excited potential for its good wavefunction overlap to both the Feshbach molecules and the absolute ground-state molecules. The three levels are coupled by two lasers, λ_1 (970 nm) and λ_2 (690 nm), that are both referenced to a stable optical frequency comb. The exact frequencies are given for our most commonly used pair of up and down transitions. (These frequencies are the Raman laser frequencies to the molecules and are 98.5 MHz lower from our laser locking frequency due to an AOM shift, see Chapter 3.3.4.) (Inset) Schematic of a three-level system with relevant notations introduced.

8.1 Transfer Scheme

An appropriate choice of the electronically excited molecule state allows a pair of cw lasers to be used for a single-step STIRAP that directly accesses the molecule's absolute ground state. Once the two lasers are properly stabilized, the long lifetimes of the initial and final states ensure that the transfer process is very efficient and reaches a single rovibrational state ($N = 0, v = 0$ of $X^1\Sigma^+$). Furthermore, the fully coherent nature of the optical transitions, which effectively drive the weakly bound Feshbach molecules directly to the deepest bound electronic ground state, avoids any heating due to random photon recoils.

For the creation of absolute ground-state KRb molecules, our scheme is shown in Fig. 8.1, where the wavelengths of the cw coupling lasers are 970 nm (λ_1) and 690 nm (λ_2). In our experiment, the two-photon beat can be maintained to a few kHz linewidth by referencing each laser to a stable optical femtosecond comb [105]. We used the vibrationally excited $v' = 23$ level of the nominally $2^3\Sigma^+$ electronically excited molecular potential [15, 99]. This state has a small mixing with a nearby $1^1\Pi$ state, which make it possible to couple this excited state to the $1^1\Sigma$ absolute ground state. The upward transition dipole moment from the Feshbach molecule state to this intermediate state was determined to be $0.005(2)ea_0$ (in Chapter 5.4.2).

8.2 Two-photon Spectroscopy

Before performing STIRAP to coherently transfer from the Feshbach molecule state to the absolute ground state, we precisely determined the energy of the absolute ro-vibronic ground state. We did this using two-photon Raman spectroscopy as was introduced in Chapter 6 and 7. To search for the absolute ground state, we fixed the laser frequency λ_1 to resonantly drive Feshbach molecules to the

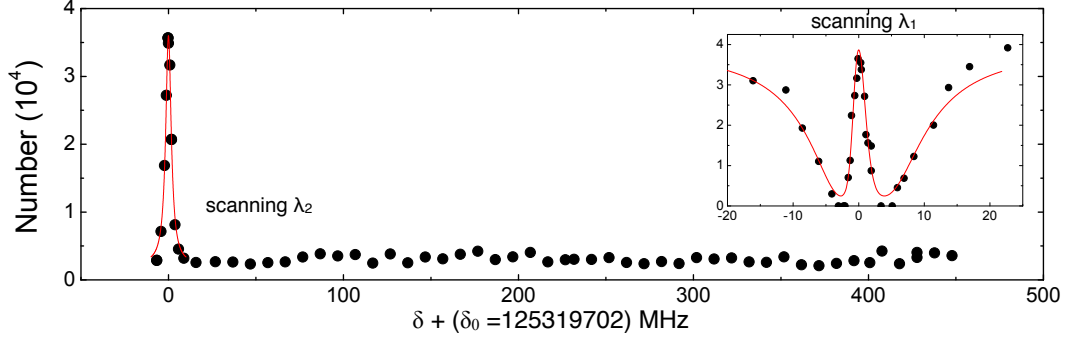


Figure 8.2: Finding the absolute ground-state level ($N = 0$, $v = 0$ of $X^1\Sigma^+$) of KRb. The binding energy of the absolute ground state was identified using two-photon dark resonance spectroscopy where the laser frequency λ_1 was fixed and the frequency λ_2 was scanned. The absolute ground state was found to be ~ 400 MHz less bound than the predicted location using potential in [28]. (Inset) The coupling strength of the λ_2 transition (corresponding Rabi frequency Ω_2) was determined by measuring the dark resonance with fixed λ_2 laser frequency while λ_1 was scanned. The dark resonance fit that allowed us to extract Ω_2 is shown as the red line.

electronically excited intermediate state. Then we scanned the laser frequency λ_2 and monitored the population of the Feshbach molecules, $|i\rangle$, after pulsing on both lasers. When the second laser field fulfills the Raman resonance condition, $\delta = 0$, the Feshbach molecules remain due to the formation of a dark state. Fig. 8.2 shows the two-photon spectroscopy results. We found the ro-vibronic ground state only ~ 400 MHz less bound than the prediction based on the KRb potential from [28]! Our measurement precisely determined the binding energy of the absolute ground state to be $h \cdot 125.319702$ THz (4180.22 cm^{-1}) at 545.88G [15].

Knowing the energy of the absolute ground state, $|g\rangle$, we can characterize the coupling strength Ω_2 (Rabi frequency) by fixing the laser frequency of λ_2 on the one-photon resonance ($\Delta = 0$) and scanning the laser frequency λ_1 . The inset of Fig. 8.2 shows the measured population of the Feshbach molecule state, $|i\rangle$, after the two-photon laser pulse. The frequency splitting between the two minima corresponds to the Rabi frequency (Ω_2) of the $|g\rangle$ to $|e\rangle$ transition. For this data,

the 7 MHz Rabi frequency was obtained using 6 mW of laser power focused to a 40 μm beam waist; this yields a transition dipole moment of 0.012(3) ea_0 for the intermediate to the ground state transition.

8.3 Stark Spectroscopy Analysis

The same form of two-photon spectroscopy in the last section can also be used to map out the energy splitting of states $|i\rangle$ and $|g\rangle$ as a function of an applied electric field. In the case where the initial state $|i\rangle$ has a negligible dipole moment, such as a Feshbach molecule, the measured Stark shift comes solely from the final state $|g\rangle$. This allows us to measure one of the most exciting properties of the ro-vibronic KRb molecules – their permanent electric dipole moment! It is worth mentioning that many theoretical efforts went into calculating the KRb permanent electric dipole moment over the last decade. However, these calculations are extremely difficult and each theoretical group gives a different result ranging from 0.5 Debye to 1.2 Debye. (A summary of theoretical results can be found in [106].)

To understand the effect of an applied electric field, I wish to first point out the difference between a magnetic dipole moment and an electric dipole moment. A magnetic dipole moment is an intrinsic property of a spin. Even in the presence of a miniscule magnetic field, magnetic dipole moments exist and take a fixed value. Electric dipole moments, on the other hand, are usually an induced dipole whose magnitude depends on the strength of the electric field. Let us take KRb molecules as an example. The electric dipole moment, pointing from the K nucleus to the Rb nucleus, comes from the fact that the two valence electrons in KRb prefer to be near the K nucleus. Without an external electric field, we could not fix the orientation of the molecular axis and the averaged electric dipole moment is therefore zero.

KRb singlet ($^1\Sigma$) molecules have no electronic spin or orbital angular mo-

mentum. Their total angular momentum apart from the nuclear spin comes solely from their rotational quantum number, N , which describes the rotation of the molecule about the molecular axis. The external electric field couples states of opposite parity and thereby polarizes molecules along the field direction. For singlet KRb molecules, these opposite parity states are rotational states. The Hamiltonian in the basis of $|N m_N\rangle$, where m_N is the projection of the rotational state along the field direction, has two terms. The first term is the rotational energy without the presence of an electric field and the second is the Stark effect:

$$\begin{aligned} & \langle N m_N | H | N' m'_N \rangle \\ &= B \cdot N(N+1) \delta_{N N', m_N m'_N} \\ & - d \cdot \varepsilon \cdot \sqrt{(2N+1)(2N'+1)} (-1)^{m_N} \begin{pmatrix} N & 1 & N' \\ -m_N & 0 & m'_N \end{pmatrix} \begin{pmatrix} N & 1 & N' \\ 0 & 0 & 0 \end{pmatrix} \end{aligned}$$

where B is the rotational constant, d is the permanent electric dipole moment, and ε is the magnitude of the external electric field. The factor that modifies $d \cdot \varepsilon$ is a geometric factor came from rotating from the molecular fixed-frame to the laboratory frame. The geometric factor, in the three-j symbols form, ensures that electric field only mixes states with the same m_N and that $|N m_N\rangle$ and $|N -m_N\rangle$ are degenerate.

Since our molecules are in the ro-vibronic ground state, we are mainly interested in the Stark effect of the rotational ground state, $|00\rangle$. In principle, this state will mix with all $|N0\rangle$ states and therefore we have to diagonalize an infinitely large matrix. However, the dominant contribution of the Stark effect comes from the $|10\rangle$ state, so in practice we only need to consider up to a finite maximum rotational quantum number, N_{max} . To evaluate what N_{max} will be sufficient, I calculate the saturated value for the electric dipole moment vs N_{max} (Fig. 8.3). For this calculation, the saturated dipole moment is considered at an

electric field that is much larger than we can achieve experimentally, 100 times the critical electric field (ε_0 is defined when $B/(d \cdot \varepsilon) = 1$. For singlet rovibrational ground-state molecules, $\varepsilon_0 \approx 4\text{kV/cm}$). From Fig. 8.3, we see that the saturated value stops growing for $N_{max} > 5$ and is around 92% of the “permanent electric dipole moment.”¹ Therefore, for the subsequent analysis, I consider mixing of states up to $N = 5$.²

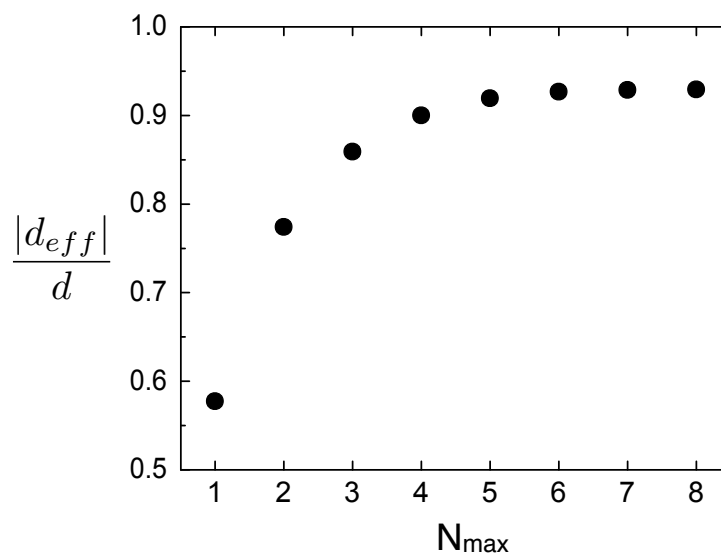


Figure 8.3: Calculation of the saturated electric dipole moment of the $N = 0$ state vs the maximum rotational state that is included in the calculation. For $N_{max} = 1$, the saturated value $|d_{eff}| = \frac{d}{\sqrt{3}} E_{stark} = d/\sqrt{3}$. As N_{max} increases, the saturated polarization approaches a value $\gtrsim 90\%$, but never reaches 100% at $100 \varepsilon_0$. The dipole moment will reach 100% only in the limit of infinitely large electric field. For further Stark spectroscopy analysis, we diagonalized the Stark Hamiltonian with $N_{max} = 5$.

¹ The saturated dipole moment will reach the full “permanent electric dipole moment” only in the limit of $\varepsilon \rightarrow \infty$ and $N \rightarrow \infty$.

² It is worth mentioning that for $\varepsilon < 2\varepsilon_0$, which is what we can achieve experimentally, the saturated dipole moment is 10% lower if considering $N_{max} = 1$ and 0.2% lower if considering $N_{max} = 2$ as comparing to considering $N_{max} = 5$.

Figure 8.4 shows the measured Stark shifts (relative to the zero electric field case) for the $N = 0$ and the $N = 2$ states of the $v = 0$ level of KRb. The splitting of $N = 0$ and $N = 2$ state at zero electric field measures $2 \cdot (2 + 1) B$. From the splitting, we extracted a rotational constant of $B = 1.1139(1)$ GHz. Finally, with the measured rotational constant, we fit the $N = 0$ Stark shift data to the Stark effect calculated including the mixing of rotational states up to $N = 5$ and extract that the permanent electric dipole moment is $0.566(17)$ D[15].³ The 3% error bar is a systematic error from our estimated uncertainty in the external electric field (see Chapter 3.2). We have also measured the Stark shift for the $N = 2$ state. This data is consistent with the dipole moment of 0.566 D that we extracted from the $N = 0$ Stark shift.

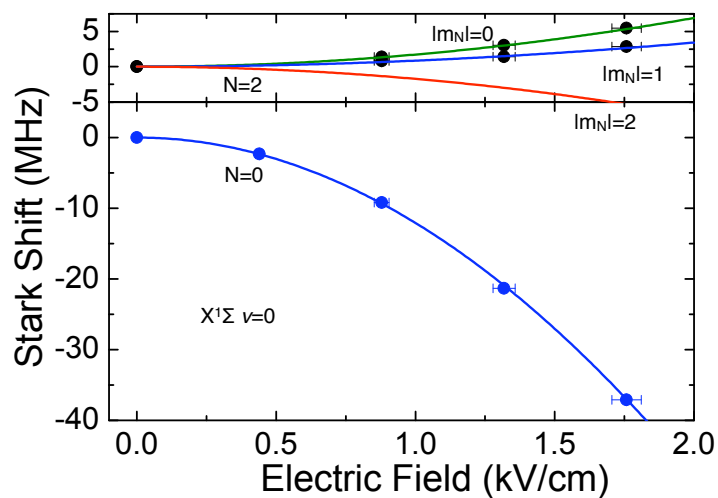


Figure 8.4: Stark spectroscopy. The measured Stark shift of the rovibrational electronic ground state of KRb is shown. From the measured Stark shift, and using the rotational constant extracted from the measured energy difference between the $N = 0$ and $N = 2$ levels at zero field, we found the $v = 0$ KRb permanent electric dipole moment to be 0.566 D. [15]

³ Since [15], we found a small error for the measurement of the separation of the E-field plates. This changes our calculated electric field and hence our measured KRb dipole moment. The updated dipole moment is $0.574(17)$ D. The E-field plates dimensions given in Chapter 3.2 are the updated values.

8.4 Population Transfer

Having determined detailed spectroscopy information of the ro-vibronic ground state, we were ready to use STIRAP [102] to transfer KRb Feshbach molecules into the absolute ground state (Fig. 8.1). As discussed in Chapter 6 and 7, the population of $|i\rangle$ can be adiabatically transferred to $|g\rangle$ by an appropriate choice for the time dependence of the coupling laser fields characterized by Rabi frequencies $\Omega_1(t)$ and $\Omega_2(t)$. The counter-intuitive STIRAP pulse sequence is to turn on the coupling Ω_2 first, and then ramp down the coupling Ω_2 (by lowering the laser intensity) while ramping up Ω_1 (see Fig. 8.5(a)). The time when Ω_2 and Ω_1 are both > 0 is when the transfer actually occurs. At the end of the STIRAP transfer, Ω_1 can be turned off.

Fig. 8.5(b) shows STIRAP transfer of KRb from the weakly bound Feshbach molecule state to the absolute ground state. More specifically, the figure shows the measured time evolution of the initial state (Feshbach molecule) population during the pulse sequence shown in Fig. 8.5(a). The disappearance of the Feshbach molecules between the time of 15 to 47 μs corresponds to transfer into the absolute ground state. To confirm this within the constraint that we can only detect Feshbach molecules, we add a reverse STIRAP pulse sequence to bring the deeply bound molecules back to Feshbach molecules for detection. For the particular dataset in Fig. 8.5(b), the round-trip transfer has an efficiency of 67%. Assuming equal efficiency each way, the one-way STIRAP transfer efficiency to the absolute ground state is 81%. Our detection method is perhaps non-standard in that it does not use direct detection of the ground-state molecules. However, this method works well because the STIRAP transfer is efficient and because absorption imaging of the Feshbach molecule gas has good signal-to-noise, similar to that typically obtained for ultracold atom gas imaging. Furthermore, this de-

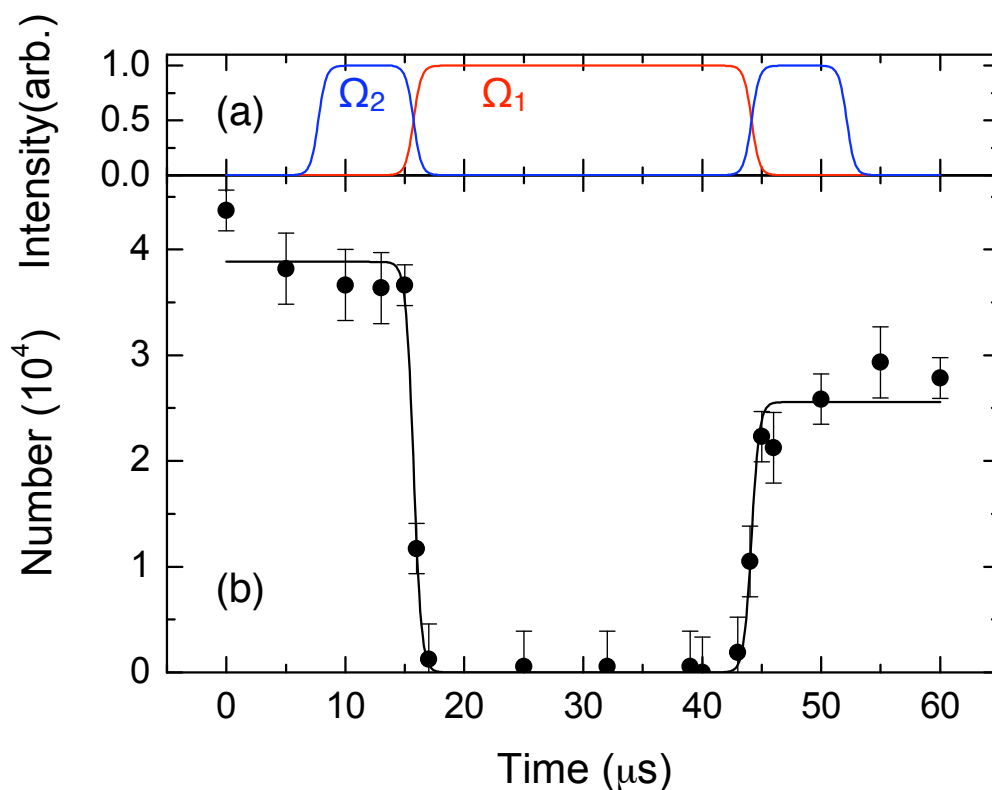


Figure 8.5: (a) Intensity vs. time for the round-trip STIRAP pulse sequence. The actual transfer step (ramping down the intensity of one laser field while ramping up the other) takes $4\mu\text{s}$. (b) Initial state (Feshbach molecules) population during the STIRAP pulse sequence. The initial state population vanishes after being transferred to the absolute ground state in the first $4\mu\text{s}$ period when both coupling laser fields are on. To detect the ground-state molecules, a reversed STIRAP transfer (the second $4\mu\text{s}$ period when both coupling laser fields are on) is used to bring these molecules back to Feshbach molecules. Assuming equal transfer efficiency each way, the one-way STIRAP efficiency is 81% [104, 100].

tection is convenient in that it is completely compatible with our ultracold gas apparatus. The reverse STIRAP step (which takes $\sim 4 \mu\text{s}$) can be viewed simply as an internal state manipulation that is part of the detection sequence for probing the ro-vibronic ground-state molecules.

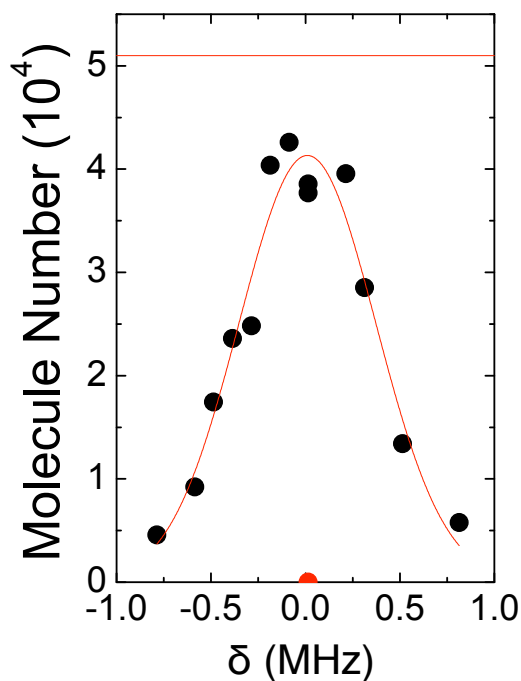


Figure 8.6: STIRAP lineshape after round-trip STIRAP (the axis of molecule number shown here has to be scaled up by 30% due to Feshbach molecule detection efficiency (85%) and imaging OD saturation (90%) that were not accounted for). We optimize STIRAP transfer by varying the two-photon detuning of the two Raman lasers, δ . Here we achieved one-way transfer efficiency $> 90\%$. The single red point is measured after one-way STIRAP. The line is only for the guide of the eyes.

The data shown in figure 8.5 was taken with both the two-photon detuning and the one-photon detuning on resonance ($\delta = 0$ and $\Delta = 0$). We saw in Chapter 6 that maintaining $\Delta = 0$ is not crucial and detuned ($\Delta \neq 0$) STIRAP also works. The usual one-photon linewidth is large (> 10 MHz) compared to other frequency drift in the system, e.g. magnetic field slow drift. However, maintaining the two-

photon resonance $\delta = 0$ is crucial. For $\delta \neq 0$, STIRAP sequence populates the excited state and molecules are lost. Experimentally, we optimize the two-photon detuning by taking a lineshape as shown in Fig. 8.6. The width of the lineshape depends on the Rabi frequency of the two coupling lasers as well as the duration of the STIRAP transfer. The round-trip STIRAP lineshape in Fig. 8.6, which has a linewidth of ~ 700 kHz, was taken using a $4 \mu\text{s}$ one-way transfer pulse and coupling laser fields with Rabi frequencies of a few MHz. This lineshape shows our optimized results with one-way transfer efficiency $> 90\%$, which corresponding to $> 5.4 \cdot 10^4$ KRb polar molecules in their absolute ground state.

8.5 Trapped Molecular Temperature and Density

We have demonstrated that transferring molecular population to the absolute ground state using STIRAP is robust and efficient. In addition, because of the coherent and the efficient nature of the transfer, there should be no heating during the transfer process. However, there can remain a small momentum recoil of the molecules caused by the two-photon Raman process. This is minimized by having the two laser beams for STIRAP be co-propagating. With this configuration for our KRb transfer, the calculated momentum kick corresponds to an energy of only $k_b \cdot 13$ nK. This kick is not random, so it is not heating. Fig. 8.7 shows a measurement of the molecular gas temperature using time-of-flight absorption imaging for Feshbach molecules before and after round-trip STIRAP transfer. We do not observe heating in the transfer process [104]. This is especially crucial because we rely on the reversed STIRAP sequence as part of our detection scheme that gives information about the number and the expansion energy (temperature) of the absolute ground-state molecules.

For data taken with short hold times ($\sim 100 \mu\text{s}$) in the absolute ground state (of course, the reverse STIRAP would provide a reverse recoil kick), we

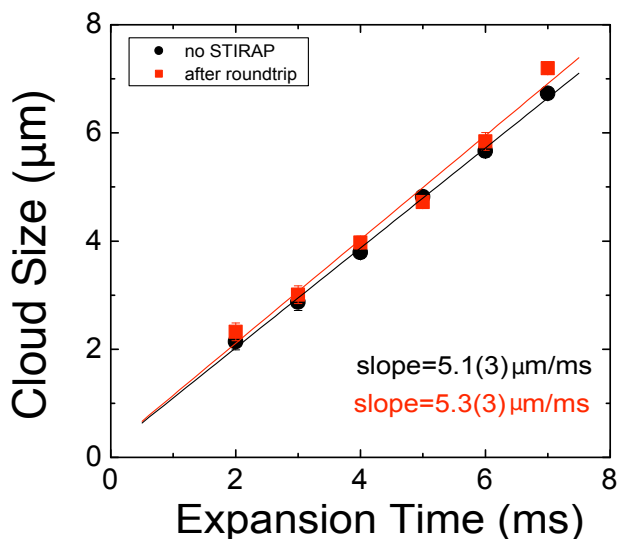


Figure 8.7: We can measure the expansion energy of Feshbach molecules before and after a round-trip transfer to the absolute ground state. The hold time in the absolute ground state was $20 \mu\text{s}$. Within their uncertainty, the two measurements give the same gas expansion velocity, and there is no observable heating during the STIRAP transfer process.

saw that the STIRAP transfer process itself does not introduce heating of the gas. However, since Feshbach molecules and ro-vibronic ground-state molecules have different AC polarizabilities at our optical trap wavelength, they see slightly different optical trapping potentials. Therefore, we observe the excitation of a density oscillation, or a breathe mode, that occurs at twice the trap frequency. The oscillation of the ground-state molecule cloud is seen immediately after the transfer (Fig. 8.8, measured in our crossed-beam dipole trap). The breathing damps out in a timescale of 50 ms most likely due to anharmonicity of the trap and the excitation energy then appears as a heating of the gas.

The AC polarizability, α , can be directly extracted from the breathe frequency at a corresponding optical trap intensity. Another method to extract α is to perturb the equilibrium position of the trap and then measure the fre-

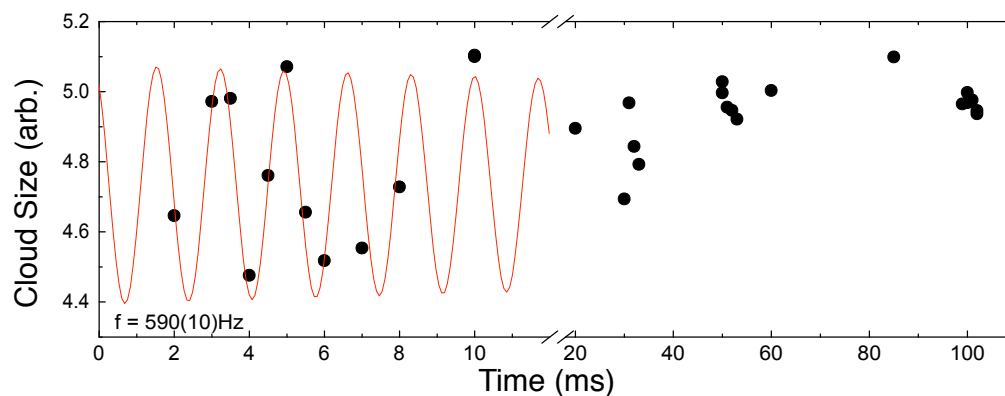


Figure 8.8: The molecular cloud exhibits a breathe motion as a function of time after the STIRAP internal state transfer from Feshbach molecules to the ro-vibronic ground state. Molecules in these two internal states have different AC polarizabilities, and therefore see an optical trapping potential with different strengths. The breathe motion damps out on a time scale of 50 ms. (This was measured in our crossed-beam optical trap.)

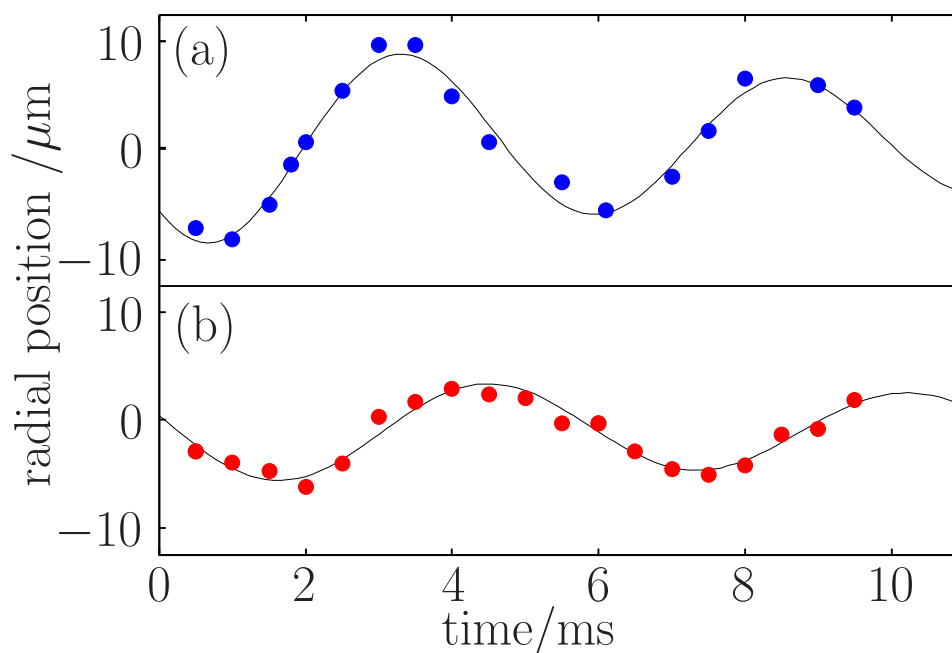


Figure 8.9: Molecule cloud center-of-mass motion after perturbing optical dipole trap by shutting it off for 0.5 ms [104]. (a) Feshbach molecules slosh frequency is $\nu_{Feshbach} = 190(3)$ Hz and (b) Ro-vibronic ground-state molecule slosh frequency is $\nu_{X^1\Sigma} = 175(5)$ Hz. (This was measured in our single-beam optical trap.)

quency of the resulting cloud slosh. Fig. 8.9(a) and (b) (measured in a single-beam optical trap) are slosh measurements for Feshbach molecules and ro-vibronic ground-state molecules, respectively, at the same trap intensity. The optical trap here uses a multi-mode 1090 nm laser. The measured slosh frequencies are $\nu_{Feshbach} = 190(3)$ Hz for the Feshbach molecules and $\nu_{X^1\Sigma} = 175(5)$ Hz for the ro-vibronic ground-state molecules. The AC polarizability ratio $\alpha_{X^1\Sigma}/\alpha_{Feshbach} = \nu_{X^1\Sigma}^2/\nu_{Feshbach}^2 = 0.85(5)$, where the Feshbach molecules have an AC polarizability $\alpha_{Feshbach} = 5.7 \cdot 10^{-5}$ (MHz/W/cm²) that is the sum of the K and the Rb polarizabilities [107].

Combining information of the number (detection efficiencies due to STIRAP transfer efficiency and Feshbach molecule detection efficiency have to be taken into account), the temperature, and the trap frequencies of ro-vibronic ground-state molecules, we can calculate their peak density in the optical dipole trap and the normalized temperature T/T_F , where $T_F = \frac{\hbar\bar{\omega}}{k_b}(6N)^{1/3}$, $\bar{\omega}$ being the geometric mean of the trap frequency, is the Fermi temperature of the gas. Typically, the peak density of the gas is 10^{12} cm⁻³ for a temperature of a few hundreds of nanoKelvins. The coldest gas of absolute ground-state molecules we achieved was at 160 nK with $T/T_F = 1.4$, and was created with STIRAP from the coldest Feshbach molecule gas we could produce. This T/T_F achieved is only a factor of 2 away in temperature and a factor of 15 away in phase-space density from quantum degeneracy.

The realization of a high phase-space-density gas of ro-vibronic ground-state polar molecules opens new and exciting prospects for studying electric-field controlled dipolar interactions in a quantum gas, and modeling exotic many-body physics Hamiltonians. At the same time, from a practical point of view, we have just begun to learn how to work with and manipulate these molecules. These singlet ground-state molecules do not have an electronic magnetic moment since

their total electronic spin is zero. (They do however have a much weaker nuclear magnetic moment.) In our first experiments realizing STIRAP transfer to singlet ground-state molecules [15], we used an atom trap that had a magnetic potential providing additional confinement along the weak direction of the single-beam optical trap. This magnetic confinement was significant for atoms and for Feshbach molecules, but did not affect the ro-vibronic ground-state molecules. This resulted in rapid axial expansion of the ground-state molecular cloud after the STIRAP transfer. In addition, there could be extra potential energy given to the ground-state molecules if the magnetic and the optical trap centers were not exactly overlapped. Eventually, we replaced the single-beam optical dipole trap by a crossed-beam dipole trap (described in Chapter 3.1) to increase the confinement, particular in the weak direction of the original optical trap. On the flip side, one advantage of a small, almost negligible magnetic moment of the molecules is that we can ramp the magnetic field in any time scale and do not have to worry that it affects the molecules.

In the next chapters, I will present experiments concerning manipulation of this tiny nuclear magnetic moment and studying the dependence of collisions of ro-vibronic ground-state molecules in a single hyperfine state.

Chapter 9

Identifying and Manipulating Molecular Hyperfine States

In the last chapter, we discussed the manipulation of KRb molecules' rotational, vibrational, and electronic state quantum numbers. To control the complete internal states of a molecule, we also need to address its hyperfine state. Full control of all the internal state quantum numbers is a prerequisite for further experiments with a quantum gas of polar molecules where collisions and interactions depend on the quantum statistics. The discussion in this chapter follows our work in [108].

Unlike the triplet molecules ($^3\Sigma$, Chapter 7) that have a total electronic spin $S = 1$ and have hyperfine splittings on the order of rotational splittings (\sim GHz), singlet molecules ($^1\Sigma$) have $S = 0$ and a hyperfine structure that comes from their nuclear spins (with energy splitting $<$ MHz). Their hyperfine splittings come from two contributions, with the nuclear Zeeman effect ($\vec{B} \cdot \vec{I}$) dominating over the spin-spin coupling ($\vec{I}_K \cdot \vec{I}_{Rb}$) at magnetic fields $>$ 20 G. In this regime, we can label hyperfine states by the individual nuclear spin projections of the K and the Rb nuclei, $|m_K, m_{Rb}\rangle$. Because K has a nuclear spin $I_K = 4$ and Rb has $I_{Rb} = \frac{3}{2}$, there are a total of 36 hyperfine states (Fig. 9.1(a)) for the ro-vibronic ground state. The hyperfine energy splitting due to $\Delta m_K = \pm 1$ is $\sim h \cdot 130$ kHz and for $\Delta m_{Rb} = \pm 1$ the splitting is $\sim h \cdot 760$ kHz at 546 G. These small energy splittings are a lot more difficult to resolve compared to the hyperfine structure

of triplet molecules. However, their energy scales are still about 10 - 100 times larger than the thermal energy of our gas at a few hundreds of nanoKelvins.

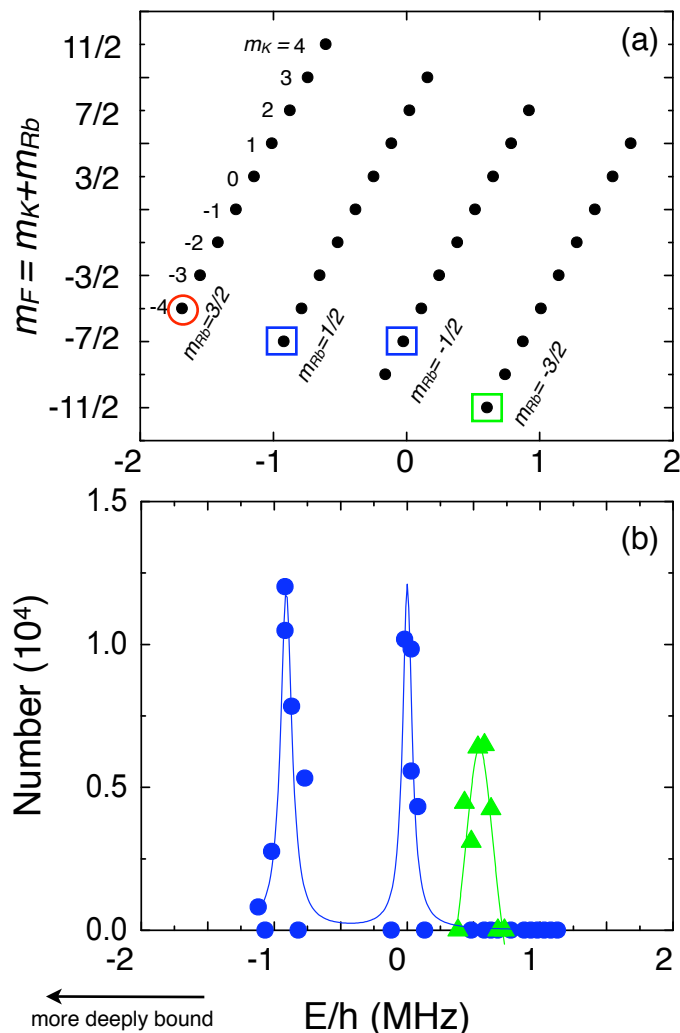


Figure 9.1: Hyperfine structure of ro-vibronic ground-state KRb molecules at 546 G. (a) There are 36 total hyperfine states that can be labelled by their nuclear spin projections $|m_K, m_{Rb}\rangle$. The lowest hyperfine state is $| - 4, 3/2\rangle$, circled in red. The energy splitting between states with $\Delta m_K = \pm 1$ is $\sim h \cdot 130$ kHz, while the splitting for $\Delta m_{Rb} = \pm 1$ is $\sim h \cdot 760$ kHz. (b) Observed hyperfine states in our STIRAP transfer. The blue circles correspond to data taken using a single circular polarization two-photon STIRAP and the green triangles correspond to data taken using mixed polarization. From the selection rules and the energy splitting among features, we can assign the observed final states as having corresponding quantum numbers of $| - 4, 1/2\rangle$, $| - 3, -1/2\rangle$, and $| - 4, -3/2\rangle$. The lines through the data are only guides to the eyes.

9.1 Identify Hyperfine States

We first identified what hyperfine state we populated in our STIRAP transfer to ro-vibronic ground-state molecules. The keys to identifying the specific hyperfine state(s) populated after STIRAP transfer were to understand the selection rules and to spectroscopically resolve different hyperfine states by narrowing down the STIRAP linewidth. In our setup, the Raman lasers for the two-photon STIRAP transition are co-propagating along the magnetic-field direction (see Fig. 3.1) Using a quarter waveplate, we can vary polarization of the two Raman laser beams to both have the same pure circular polarization or to both have a mixture of σ^+ and σ^- . Conservation of angular momentum tells us that the two-photon transition only allows the change of total angular momentum, $\Delta m_F = 0, 2,$ or -2 . Since the Feshbach molecules has $m_F = -7/2$ (see Chapter 4.1), the final molecule state after transfer must have $m_F = -3/2, -7/2,$ or $-11/2$.

Our ability to spectroscopically resolve different hyperfine states depends on the linewidth of the STIRAP transfer, which is in turn set by the STIRAP pulse duration. To resolve different hyperfine states, we narrowed down the linewidth as compared to the one in Fig. 8.6 by applying a longer STIRAP pulse (15 μ s). We observed a total of three different hyperfine states (Fig. 9.1(b)) when we iterated through three different ro-hyperfine states of the electronic excited level (Table 5.3). Two of the final hyperfine states were accessed through the two-photon transition where both photons had the same polarization (blue circles in Fig. 9.1(b)), while one of the final hyperfine states was accessed only when both photons had a mixture of polarizations (green triangles in Fig. 9.1(b)). From selection rules and the relative energies, we identified the three states as $|m_K = -4, m_{Rb} = 1/2\rangle, |-3, -1/2\rangle,$ and $|-4, -3/2\rangle$.

Out of the three intermediate excited states in Table 5.3, the one with the

transition frequency of 309602.753 GHz only couples to $|-4, 1/2\rangle$. The intrinsic selection rule of this intermediate state guarantees that we always populate a single hyperfine state without having to worry about polarization and to narrow STIRAP lineshapes.

9.2 Manipulate Molecular Hyperfine States

Using STIRAP, we can populate ro-vibronic ground-state molecules in a single hyperfine state. However, because our starting Feshbach molecules have $m_F = -7/2$, using a two-photon transition in our setup will not allow us to directly populate molecules in the lowest hyperfine state, $|-4, 3/2\rangle$, which has $m_F = -5/2$. Reaching the lowest hyperfine state of the ro-vibronic ground-state has turned out to be important for studying collisional stability of these molecules.

9.2.1 State Transfer to the Lowest Hyperfine State

To reach the lowest hyperfine state ($|-4, 3/2\rangle$), we can in principle start by populating molecules in $|-4, 1/2\rangle$ and then drive a nuclear spin transition. However, this nuclear magnetic transition ($m_{Rb} = 1/2$ to $m_{Rb} = 3/2$) couples only weakly to external magnetic field. Moreover, this transition is nearly degenerate with the spin flip of $m_{Rb} = 1/2$ to $m_{Rb} = -1/2$, where the energy difference is only about 20 Hz out of 760 kHz. Therefore, the straightforward single nuclear spin flip does not work for us.

To manipulate nuclear spins, we came up with a general scheme that relies on electronic dipole transitions involving the rotational excited state $N = 1$ [108]. Since the transition relies on a large electric dipole moment, this method requires polar molecules with a permanent electric dipole moment.

Before we drive transitions from $N = 0$ to $N = 1$, our theorist friend Goulsen Quéméner first calculated the $N = 1$ hyperfine structure at 545.9 G. This

calculation included states of rotational projection $m_N = 0, 1,$ and -1 onto the magnetic field axis (which usually would be thought to be degenerate in the presence of zero electric field) and the hyperfine states, using the relevant *ab initio* parameters from [109]. Together, there are a total $3 \times 36 = 108$ states. The splittings of states differing only in m_N are about a few hundreds of kHz. These splittings come from interactions of the nuclear electric quadrupole moments of the ^{40}K and ^{87}Rb nuclei and the electric-field gradients created from molecule's electron cloud. This mechanism provides coupling between nuclear hyperfine states and rotation and can serve as a means to manipulate hyperfine states!

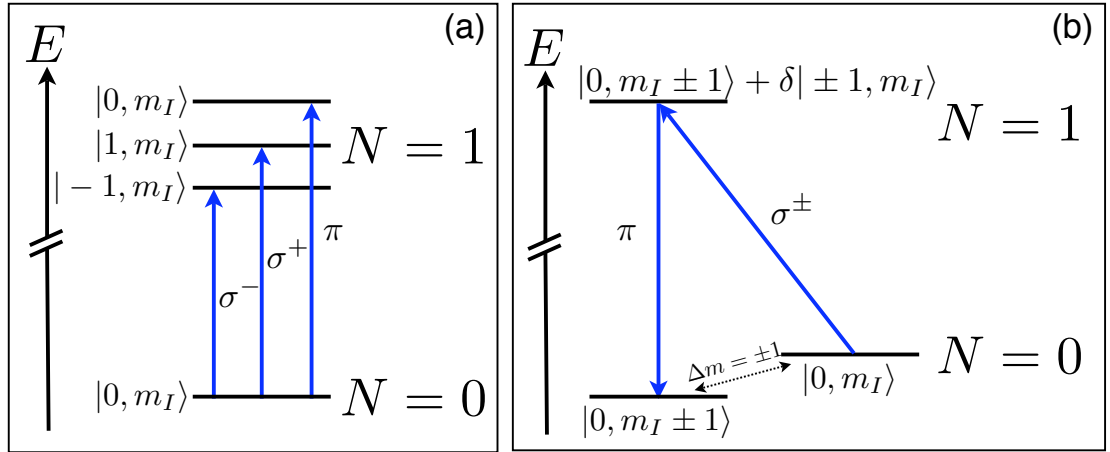


Figure 9.2: A general scheme of hyperfine state manipulation. (a) Electric dipole transitions between $N = 0$ and $N = 1$, which leave the nuclear spin unchanged. (b) Strong nuclear electric quadrupole interactions mix rotations and hyperfine states. Eigenstates considering this interaction become $|0, m_I \pm 1\rangle + \delta |\pm 1, m_I\rangle$, with $|\delta|^2 \ll 1$. This allows an effectively spin changing transition from $N = 0$ to $N = 1$. With an additional non-spin-flip transition from $N = 1$ to $N = 0$, we can effectively manipulate hyperfine states within the ro-vibronic ground-state manifold.

To leading order, an applied microwave field (~ 2 GHz) can drive σ^+ , σ^- , and π electric-dipole transitions from $|N = 0, m_N = 0\rangle$ to $|1, 1\rangle$, $|1, -1\rangle$, and $|1, 0\rangle$ respectively while leaving the nuclear spins unchanged. We drive these transitions using an amplified microwave source ($\sim 5\text{W}$) that is delivered by a wave-

main state	admixed state	$ \delta_{\text{th}} ^2$	$ \delta_{\text{exp}} ^2$
$ 1\ 0\ -4\ 3/2\rangle$	$ 1\ 1\ -4\ 1/2\rangle$	0.045	≈ 0.1
$ 1\ 0\ -3\ 1/2\rangle$	$ 1\ 1\ -4\ 1/2\rangle$	0.0085	≈ 0.0064

Table 9.1: Mixing of different hyperfine states in the rotationally excited state $N = 1$ at $B = 545.9$ G. We compare the theoretically calculated admixture $|\delta_{\text{th}}|^2$ to the experimentally measured admixture $|\delta_{\text{exp}}|^2$.

uide (31-cm long and 20.5×10.4 cm² in cross-section area). The relative strength of these transitions allows us to calibrate the strength of individual polarization component in our microwave field. Now, the nuclear electric quadrupole interactions for $N = 1$ mix states of different hyperfine characters with $m_N + m_K + m_{Rb}$ being the conserved quantity. This mixing results in eigenstates (written in the uncoupled basis) that have the form of $|N, m_N, m_K, m_{Rb} \pm 1\rangle + \delta|N, m_N \pm 1, m_K, m_{Rb}\rangle$ (or $|N, m_N, m_K \pm 1, m_{Rb}\rangle + \delta|N, m_N \pm 1, m_K, m_{Rb}\rangle$), where $|\delta|^2 \ll 1$ characterizes the small admixed state. The small admixture allows us to effectively have a nuclear spin flip when driving between rotational states. Figure 9.3 show the Rabi floppings between $N = 0$ and $N = 1$ hyperfine states. Since the electronic dipole transition only talks to the non-spin-flip part, all transitions here have the polarization of σ^+ . For a given microwave power, we can obtain relative Rabi frequencies that characterize the admixed fractions for Fig. 9.3(b) and (c). The admixture measurement is summarized in Table 9.1.

With a combination of one spin flip transition from $N = 0$ to $N = 1$ and then a non-spin-flip transition from $N = 1$ back to $N = 0$, we can effectively drive population between two hyperfine states within the ro-vibronic ground-state manifold. We demonstrated this general scheme of manipulation by populating molecules in the lowest hyperfine states of the ro-vibronic ground-state (Fig. 9.4). We start with molecules in $|-4, 1/2\rangle$ of the ro-vibronic ground state directly after a STIRAP transfer. We then use a π -pulse to drive a spin-flip transition to

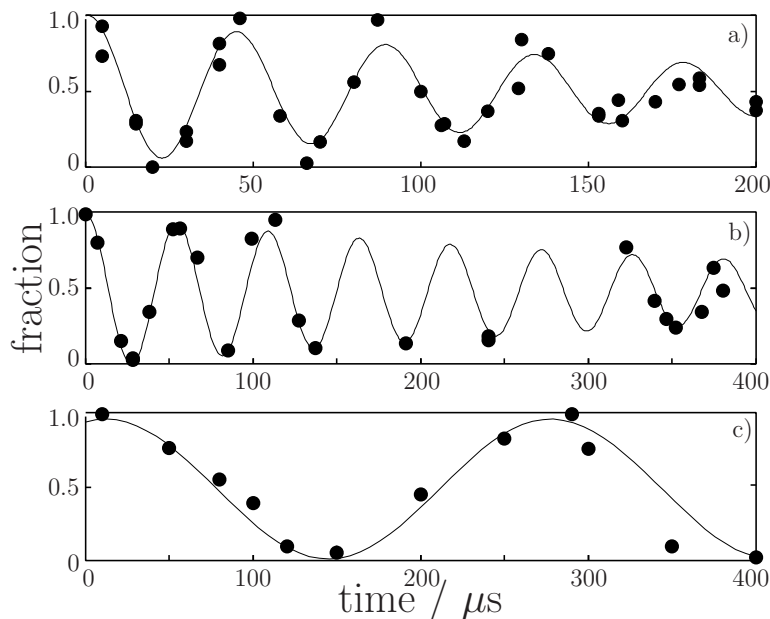


Figure 9.3: Rabi oscillations on a (a) hyperfine preserving microwave transition $|0, 0, -4, 1/2\rangle \rightarrow |1, 1, -4, 1/2\rangle$ (b) Rb nucleus hyperfine changing transition $|0, 0, -4, 1/2\rangle \rightarrow |1, 0, -4, 3/2\rangle + \delta|1, 1, -4, 1/2\rangle$ (c) K nucleus hyperfine changing transition $|0, 0, -4, 1/2\rangle \rightarrow |1, 0, -3, 1/2\rangle + \delta|1, 1, -4, 1/2\rangle$. Note the different time axis in panel (a). The microwave power was reduced by a factor of 4 for the data in (a) resulting in an effective decrease of the Rabi frequency by a factor of 2.

$|1, 0, -4, 3/2\rangle + \delta|1, 1, -4, 1/2\rangle$. The admixture here was measured to be about 10%. A single π -pulse efficiency is typically around 90-95%. Then we perform another π -pulse to drive the non-spin-flip transition to $|0, 0, -4, 3/2\rangle$, and thereby populate the lowest energy state!

9.2.2 More Hyperfine Spectroscopy

The manipulation scheme introduced in the last section is general and can be applied to move population anywhere within the ro-vibronic ground-state manifold. Here we present a summary, Table 9.2, of microwave hyperfine state spectroscopy where we map out all transitions connecting to the initial $|0, 0, -4, 1/2\rangle$ state. One exception was the transition to $|1, -1, -3, 1/2\rangle$, which we were unable to measure because the transition is weak and lies very close to two other strong

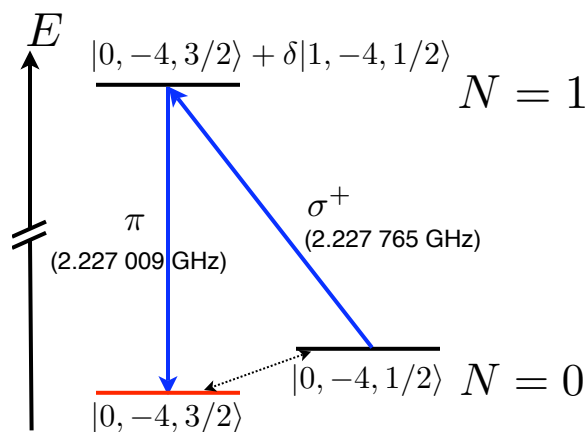


Figure 9.4: The specific scheme we used to transfer molecules from $|0, 0, -4, 1/2\rangle$ to the lowest hyperfine state $|0, 0, -4, 3/2\rangle$ at 546 G.

microwave transitions.

Using all our measured transition frequencies, G. Quéméner had used root-mean-square fit to extract rotational constant $B = 1.113950(5)$ GHz and the electric quadrupole term coefficients $eqQ_K = 0.45(6)$ MHz and $eqQ_{Rb} = -1.41(4)$ MHz. The electric quadrupole moment terms are 10-30% different from the *ab initio* calculations in [109].

The general scheme of manipulation of hyperfine states allowed us to populate molecules in a *single* hyperfine state and the *lowest* energy state. This is the first time that we have the exquisite control of all internal quantum states of ultra-cold molecules, and this is extremely crucial for the collisional studies presented in the next chapter. Moreover, many proposals recently have been exploiting possibilities of using microwave transitions that couples rotational states for shielding inelastic collisions [110] and studying exotic many-body physics [39, 40, 111]. Our detailed hyperfine spectroscopy gave a realistic picture of the rich structure of a “single” rotational line that needs to be taken into consideration for such proposals.

State i	state j	exp. (kHz)	theory (kHz)	abs. diff.
$ 0\ 0\ -4\ 1/2\rangle$	$ 1\ 1\ -4\ 1/2\rangle$	2227 837(5)	2227 835	2
$ 0\ 0\ -4\ 1/2\rangle$	$ 1\ 0\ -4\ 1/2\rangle$	2228 125(5)	2228 119	6
$ 0\ 0\ -4\ 1/2\rangle$	$ 1\ -1\ -4\ 1/2\rangle$	2227 774(7)	2227 776	2
$ 0\ 0\ -4\ 1/2\rangle$	$ 1\ 0\ -4\ 3/2\rangle$	2227 009(2)	2227 008	1
$ 0\ 0\ -4\ 1/2\rangle$	$ 1\ -1\ -4\ 3/2\rangle$	2227 133(20)	2227 128	5
$ 0\ 0\ -4\ 1/2\rangle$	$ 1\ 0\ -3\ 1/2\rangle$	2228 237(10)	2228 225	12
$ 0\ 0\ -4\ 1/2\rangle$	$ 1\ 1\ -4\ -1/2\rangle$	2228 588(5)	2228 593	5
$ 0\ 0\ -4\ 1/2\rangle$	$ 1\ 0\ -4\ -1/2\rangle$	2228 804(1)	2228 805	1
$ 0\ 0\ -4\ 3/2\rangle$	$ 1\ 0\ -4\ 3/2\rangle$	2227 765(10)	2227 761	4
$ 0\ 0\ -3\ 1/2\rangle$	$ 1\ 0\ -3\ 3/2\rangle$	2228 109(16)	2228 091	18

Table 9.2: Spectrum of rotational transitions from hyperfine state $|i\rangle$ within $N = 0$ to hyperfine state $|j\rangle$ within the $N = 1$ manifold. We compare the experimentally measured transition frequencies to the theoretical calculation.

Chapter 10

Ultracold Chemistry and Inelastic Collisions

In the last two chapters, we have demonstrated a complete control over the KRb molecular internal-state quantum numbers, which allows us to probe inelastic collisions one quantum state at a time. Moreover, the possibility of putting molecules into the *lowest* electronic, vibrational, rotational, and hyperfine energy state, raises an immediate question that is “can these molecules still be lost from the trap?” If they can, “what determines the loss rate?” Since molecules are already in the lowest energy state, the only way for them to suffer inelastic collisions, which release energy and cause loss from the trap is through chemical reactions. Here the exiting particles after the collisions are different chemical species. In Table 10.1, we consider the binding energy of various types of molecules that could be made from different combinations of ^{40}K and ^{87}Rb atoms. These energy estimates allow us to assess whether a specific two-body reaction process is allowed (exothermic) or not (endothermic) in the ultracold gas. In the sections below, we will refer back to Table 10.1 to test each “entrant” channel for possible reactions, and show that exothermic reactions take place at universal rates that are determined solely by long-range interactions and the quantum statistics of collisions.

Molecules	$v = 0$ binding energy (D_0)	reference
$^{87}\text{Rb}_2$	3965.8(4) cm^{-1}	[112]
$^{40}\text{K}^{87}\text{Rb}$	4180.417 cm^{-1}	[15]
$^{40}\text{K}_2$	4405.389(4) cm^{-1}	[113]
K_2Rb	$\sim 13000 \text{ cm}^{-1}?$	
KRb_2	$\sim 12000 \text{ cm}^{-1}?$	

Table 10.1: Summary of the relevant molecular energetics involved in possible chemical reactions. The binding energies are given with respect to the threshold energy for free atoms in the absence of a magnetic field. The $^{87}\text{Rb}_2$ and $^{40}\text{K}_2$ binding energies include isotope shifts from the data in the respective references. The trimer binding energies are unknown and we give here crude estimates as a sum of the binding energies of the three relevant pairs. For example for K_2Rb , we list twice the binding energy of KRb plus the binding energy of K_2 . Calculations are needed and will undoubtedly change the values given here.

10.1 Atom-Molecule Collisions

We first study two-body collisions of atoms and molecules. As a prerequisite, we assume and will verify in section 10.3 that inelastic collisions of our spin-polarized fermionic molecules occur only at a relatively low rates.

To prepare the atom-molecule mixture, we control the atom density by selectively removing or heating up unpaired atoms after the initial molecule creation.¹ For these experiments, we typically work with an atom number about 5 to 15 times larger than the molecule number. All atoms and molecules are prepared in their lowest energy states at 545.9 G. Specifically, K atoms are in their $|F = 9/2, m_F = -9/2\rangle$ state, Rb in $|F = 1, m_F = 1\rangle$, and KRb in $|-4, 3/2\rangle$.

¹ The procedure of removing selective amounts of K is the following. We partially transfer the population of K atoms from $|F = 9/2, m_F = -9/2\rangle$ to $|9/2, -5/2\rangle$ using two successive rf pulses. We then clean out K atoms in the $|9/2, -9/2\rangle$ state using resonant light as described in Chapter 4.1.2. Once they are heated out of the trap, we again use rf pulses to spin flip K $|9/2, -5/2\rangle$ atoms back down to $|9/2, -9/2\rangle$. To selectively vary the density of Rb, we perform a complete spin flip from $|1, 1\rangle$ to $|2, 2\rangle$ and then turn on resonant light for a duration between 1 μs to 10 μs . The resonant light both removes Rb atoms and heats up the remaining gas. After the resonant light pulse, Rb atoms are transferred back to the lowest hyperfine state $|1, 1\rangle$. We then apply an additional resonant light pulse to remove any residual Rb in $|2, 2\rangle$, thus ensuring that all Rb atoms are in the $|1, 1\rangle$ state.

Here F is the total atomic spin and m_F is the spin projection. We performed two separate experiments, one with a combination of K and KRb and the second with a combination of Rb and KRb. In both cases, the background of atoms in the other, undesired, atomic species was less than 1000 atoms, corresponding to a density below $5 \times 10^9 \text{ cm}^{-3}$. Since both the atoms and the molecules are prepared in their lowest energy states, trap loss due to inelastic spin-changing collisions is not possible. However, loss from chemical reactions for the case of $\text{K} + \text{KRb}$ is energetically allowed since $\text{K} + \text{KRb} \rightarrow \text{K}_2 + \text{Rb}$ is exothermic, while $\text{Rb} + \text{KRb} \rightarrow \text{Rb}_2 + \text{K}$ is endothermic (Table 10.1).

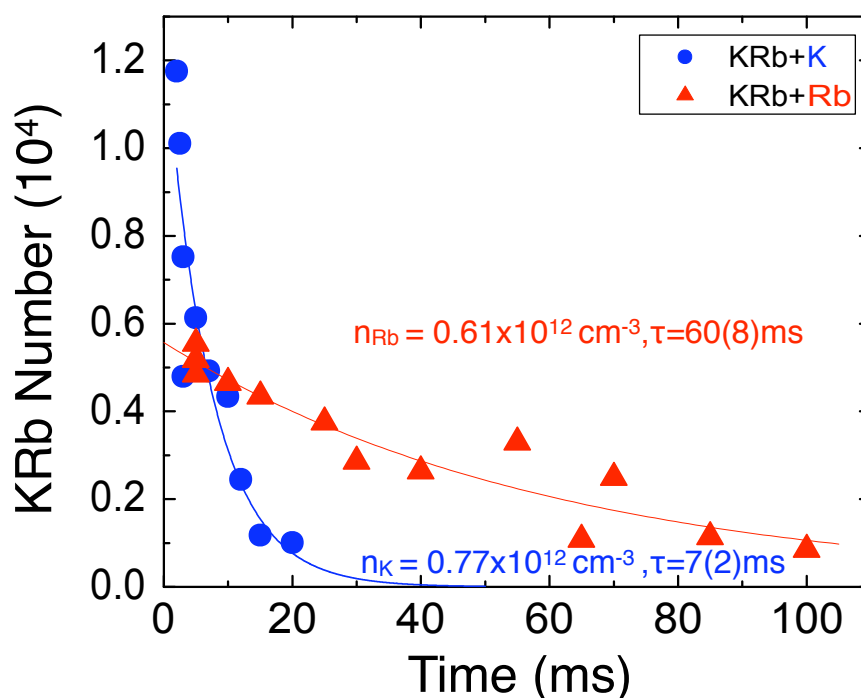


Figure 10.1: Sample decay curves for the molecular number when subject to collisions with K atoms (circles) and with Rb atoms (triangles). All species are prepared in their lowest energy internal states. The atom numbers are 5 to 15 times higher than the molecule numbers. The reduced initial molecule number for KRb+Rb is due to the collisional quenching of the initial weakly bound KRb Feshbach molecules with Rb [24] before the two-photon Raman process that transfers the molecules down to the ro-vibronic ground state.

For each experiment, we measured the time-dependence of the trapped molecule population. Typical molecular loss curves are shown in Fig. 10.1. To extract the inelastic collision rate, we assume that the atom number density is constant. This is approximately true because the number of atoms is much larger than the number of molecules. The trapped molecular number should then decay as

$$\frac{d}{dt}N_{molecule} = -\beta \cdot N_{molecule} \cdot n_{atom}, \quad (10.1)$$

where $N_{molecule}$ is the number of molecules, n_{atom} is the atomic density, and β is the inelastic rate coefficient. We can then extract β via an exponential fit, $e^{-\beta \cdot n_{atom} \cdot t}$. As can be seen in Fig. 10.1, in general we find that the molecules are lost from the trap at a much faster rate when K atoms are present than when a similar density of Rb is present.

To see if the molecule loss is due to atom-molecule collisions, we measure the dependence of the loss rate on the atom gas density. For the case of KRb + K, we see a clear linear dependence on the atomic density and extract an inelastic collision rate coefficient of $1.7(3) \cdot 10^{-10} \text{ cm}^3/\text{s}$. In contrast, for KRb + Rb collisions, the density dependence of the loss rate is much less clear. Nevertheless, we again fit the dependence as linear and obtain a suppressed rate coefficient of $0.13(4) \cdot 10^{-10} \text{ cm}^3/\text{s}$. A possible mechanism for a loss rate that is independent of the atom density would be collisions of ground-state KRb molecules with undetected molecules in high lying vibrationally excited states. These contaminant molecules could be produced by inelastic collisions of Rb atoms with our weakly bound KRb Feshbach molecules [24] before the two-photon Raman process that produces ground-state molecules. The fact that we observe a smaller initial number of ground-state molecules when Rb atoms are present is consistent with this picture. The linear fit to β vs n_{Rb} provides an upper limit for the KRb + Rb

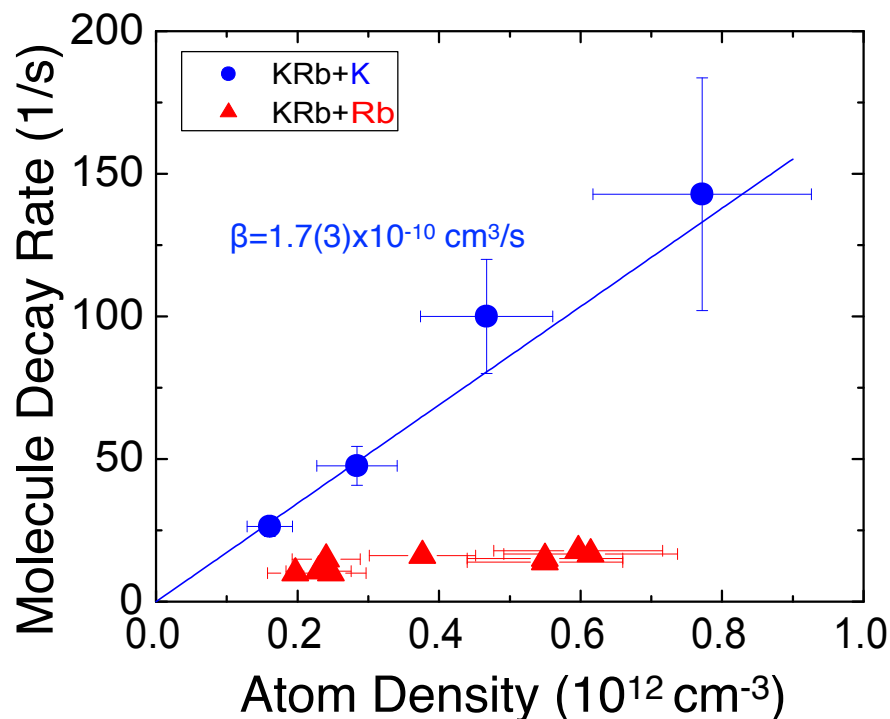


Figure 10.2: Dependence of the molecule loss rate on the atomic gas density for collisions of atoms and molecules in their lowest energy internal states. We observe strong molecule loss with $\beta = 1.7(3) \cdot 10^{-10} \text{ cm}^3/\text{s}$ for KRb+K collisions and suppressed loss of KRb for KRb+Rb collisions. This suggests that the KRb decay mechanism is due to the exothermic chemical reaction $\text{K} + \text{KRb} \rightarrow \text{K}_2 + \text{Rb}$. The corresponding reaction for $\text{Rb} + \text{KRb}$, $\text{Rb} + \text{KRb} \rightarrow \text{Rb}_2 + \text{K}$, is endothermic and is not energetically possible at ultralow temperatures.

inelastic rate coefficient that is one order of magnitude smaller than what we measure for $\text{KRb} + \text{K}$. This is consistent with $\text{KRb} + \text{K}$ collisional loss due to the chemical reaction $\text{KRb} + \text{K} \rightarrow \text{K}_2 + \text{Rb}$ (at ultracold temperatures!) In the case of $\text{KRb} + \text{Rb}$, there is no two-body chemical reaction pathway and the inelastic rate for atom-molecule collisions is strongly suppressed.

We note that we only observe this suppressed loss rate when both KRb and Rb are prepared in their lowest energy internal states at 545.9 G. We have measured an inelastic rate coefficient of the order $10^{-10} \text{ cm}^3/\text{s}$ when KRb is prepared

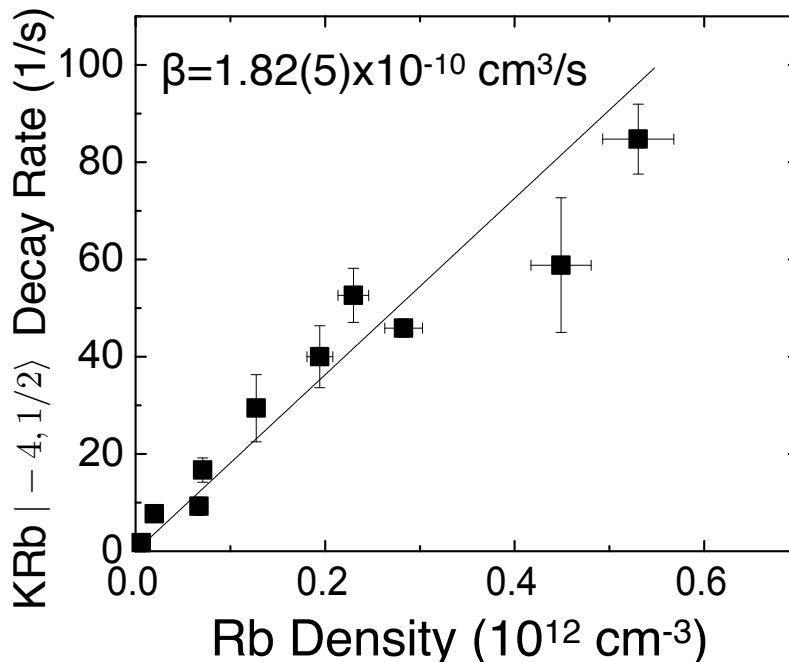


Figure 10.3: KRb+Rb collisions when KRb molecules are prepared at an excited hyperfine state, $| -4, 1/2 \rangle$, and Rb atoms are prepared in their lowest energy state $|1, 1\rangle$. We observe a strong molecular loss rate of $1.82(5) \cdot 10^{-10} \text{ cm}^3/\text{s}$.

in the higher energy $| -4, 1/2 \rangle$ hyperfine state (Fig. 10.3) and/or Rb is prepared in its $|2, 2\rangle$ hyperfine state. Therefore, for practical reasons, removing Rb atoms is important for creating a long-lived sample of ground-state KRb molecules.

10.2 Universal Loss Rate

To understand the loss rates, we use a model based on the formalism of multi-channel quantum defect theory (MQDT) [114, 89] to estimate their values. In this model, our collision process is characterized by a van der Waals intermolecular potential, $-C_6/R^6$, where C_6 is the van der Waals dispersion coefficient. When the collisional partners come within the van der Waals length of each other, inelastic collisions happen with some probability which we assume to be unity for

now. The van der Waals length is defined as

$$l_{vdw} = \frac{\cos(\pi/4) \Gamma(3/4)}{2 \Gamma(5/4)} \left(\frac{2\mu C_6}{\hbar^2} \right)^{1/4}, \quad (10.2)$$

where μ is the reduced mass of the system and Γ stands for the Gamma function.

The inelastic loss rate is

$$\beta_{inelastic} = \left(\frac{4\pi\hbar}{\mu} \right) \text{Im}(a), \quad (10.3)$$

where $\text{Im}(a)$ is the imaginary part of the scattering length. In this model where the van der Waals length is assumed to be the characteristic length, we can replace $\text{Im}(a)$ with l_{vdw} , and predict a universal loss rate that is solely determined by the long-range part of the potential.

Now, we estimate the universal inelastic collision rates for KRb + K (due to chemical reactions) from the van der Waals length characterizing the long-range part of the potential between the collision partners. The van der Waals lengths are directly calculated from the corresponding C_6 coefficients which are calculated by S. Kotochigova. For KRb + K, C_6 is 7019 atomic unit (a.u., 1 a.u. is $E_{Hartree} \cdot a_0^6$, where $E_{Hartree} = 4.36 \cdot 10^{-18}$ J and $a_0 = 0.53 \cdot 10^{-10}$ m.), which gives a predicted reaction rate of $1.1 \cdot 10^{-10}$ cm³/s. The rate agrees well with the experimental measurement, which supports the universal loss model where long-range quantum scattering and short-range unity loss characterize the inelastic process.

10.3 Molecule-Molecule Collisions

We have learned so far that atom-molecule collisions lead to rapid inelastic or chemically reactive loss of trapped KRb molecules. Therefore, to have a long-lived sample of molecules and to study intrinsic collisions of molecules, we remove all atoms using the procedure described in Chapter 4.1.2. Right away, we observed molecular lifetimes on the order of 300 ms. However, the observed lifetime did

not depend on the molecular density but rather depended on the intensity of our crossed-beam dipole trap (corresponding roughly to a power law with exponent 2 to 3). Since we were using a broad linewidth (~ 1 nm) multi-mode 1090 nm laser, we suspected that the two laser beams might give rise to molecule loss through a multi-photon processes. We then exchanged the dipole trap laser for a single frequency 1064 nm laser and offset the frequencies of the two crossed beams by 130 MHz. This resulted in a longer molecule lifetime and enabled our study of intrinsic molecular collisions.

Molecule-molecule collisions can lead to a few possible decay mechanisms. From a purely energetic argument based on the energetics summarized in Table 10.1, the molecule-molecule collisions have three possible exothermic chemical reactions, namely $\text{KRb} + \text{KRb} \rightarrow \text{K}_2 + \text{Rb}_2$, $\text{KRb} + \text{KRb} \rightarrow \text{K}_2\text{Rb} + \text{Rb}$, and $\text{KRb} + \text{KRb} \rightarrow \text{KRb}_2 + \text{K}$. All of these reactions require breaking and making molecular bonds. If the KRb molecules are prepared in an excited hyperfine state, an additional inelastic scattering mechanism is spin relaxation to a lower hyperfine state.

The quantum statistics of the molecules plays an essential role for collisions of molecules at a temperature of a few hundreds of nanoKelvin. At these ultralow temperatures, collisions with large-impact parameters and correspondingly large centrifugal barriers are frozen out and the collisions are typically dominated by a single partial wave, with relative angular momentum quantum number $L=0$ (s -wave) or $L=1$ (p -wave). Our KRb molecules are fermions and therefore the collisional wave function has to be antisymmetric with respect to particle exchange. For spin-polarized molecules, where they are all prepared in exactly the same internal quantum state, p -wave is the lowest allowed collision channel. The height of the centrifugal barrier for $L=1$ KRb molecule-molecule collisions is $k_B \cdot 24 \mu\text{K}$.²

This barrier height is an order of magnitude higher than $k_B T$, where T is the translational temperature of the molecular gas. Thus, collisions of spin-polarized molecules are expected to proceed predominately by tunneling through the p -wave barrier. If two molecules make it through the barrier to short range, chemical reactions or hyperfine state-changing can take place, leading to a loss of the entrant channel population.

10.3.1 p -wave Collisions

The quantum nature of the collisions can be seen in the temperature dependence of loss rates. The Bethe–Wigner threshold law [115] predicts that the p -wave inelastic/reactive collision rate should be linear in temperature ($\propto T$). To look for this behavior, we first prepared spin-polarized molecules in the single hyperfine state $|-4, 1/2\rangle$ for various T ranging from 200 to 900 nK. The temperature is measured from the expansion energy of the molecular gas after releasing it from the optical trap. For each initial temperature, we observed the time-dependent molecular loss and extracted a two-body loss rate β (which is 2 times the collisional event rate) by fitting the measured decay of the molecular gas density n vs. time t (Fig. 10.4) to the solution of the following differential equation,

$$\frac{dn}{dt} = -\beta n^2 - \alpha n. \quad (10.4)$$

Here, the first term accounts for number loss and the measured β can be compared to theoretical predictions. The second term accounts for density change due to heating of the trapped gas during the measurement. Within a single measurement, we observe an increase in temperature that is at most 30%. In the analysis for each data set, we fit the measured temperature to a linear heating and obtain

² The height of the p -wave barrier is determined by the molecule-molecule long-range potential, namely $\frac{\hbar^2 L(L+1)}{2\mu R^2} - \frac{C_6}{R^6}$, for $L = 1$ and $C_6 = 16130$ a.u.

a constant slope c . In Eq. 10.4, we then use $\alpha = \frac{3}{2} \frac{c}{T+ct}$, where T is the initial temperature. The time evolution of the molecular density based on Eq. 10.4 is

$$n(t) = \frac{c n_0 T^{3/2}}{(ct + T)(-2n_0 \beta T^{3/2} + c\sqrt{ct + T} + 2n_0 \beta T \sqrt{ct + T})}. \quad (10.5)$$

At our lowest temperature of 250 nK, the heating was 7(1) nK/s and $\beta = 3.3(7) \cdot 10^{-12} \text{ cm}^3/\text{s}$ (Fig. 10.4). The measured dependence of β vs. T is summarized in Fig. 10.5 (closed circles). Here, we fit the data to a power law $\beta(T) \propto T^L$ and find that $L = 1.1(2)$, which agrees with the predicted p -wave threshold law. This demonstrates that indistinguishable $^{40}\text{K}^{87}\text{Rb}$ molecules at ultralow temperatures collide via tunneling through a p -wave barrier followed by an inelastic collision in the short range. A linear fit to the data ($L = 1$) yields a slope of the decay rate coefficient of $1.2(3) \cdot 10^{-5} \text{ cm}^3/\text{s}/\text{Kelvin}$.

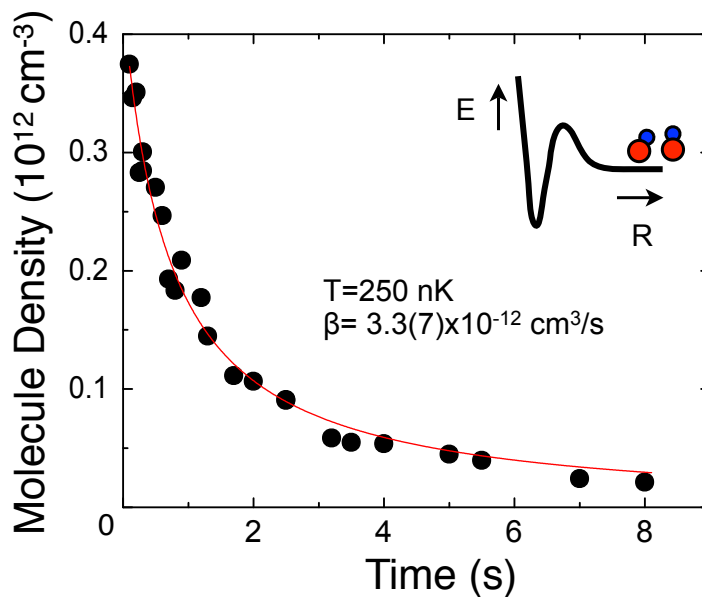


Figure 10.4: A sample molecular density decay vs time for inelastic collisions between indistinguishable fermionic molecules in the ro-vibronic ground-state of $^{40}\text{K}^{87}\text{Rb}$. Here the molecules are prepared in a single hyperfine state, $|-4, 1/2\rangle$, and the molecular density decays slowly with a rate coefficient of $3.3(7) \cdot 10^{-12} \text{ cm}^3/\text{s}$ at $T = 250 \text{ nK}$.

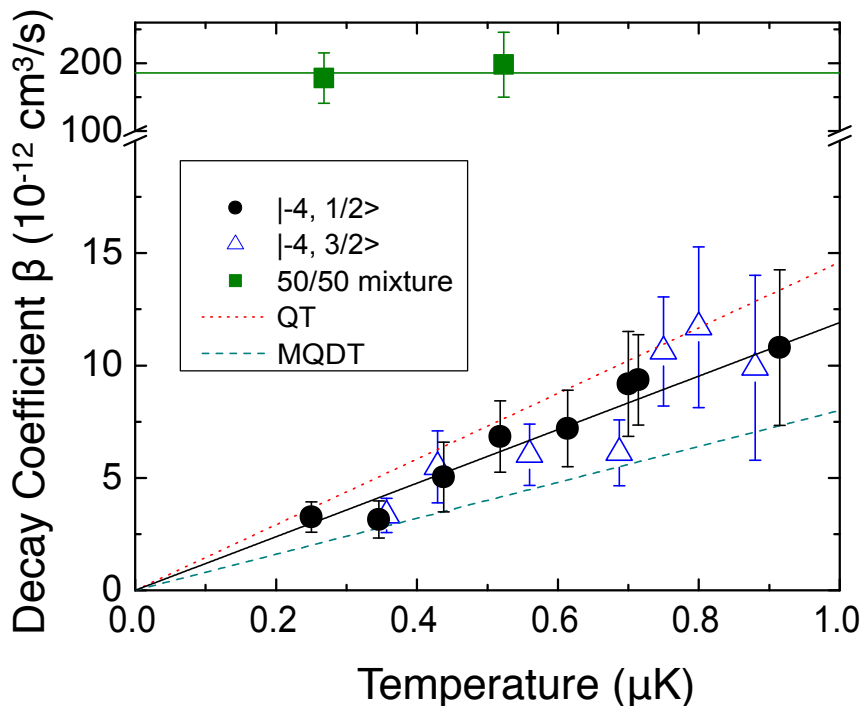


Figure 10.5: Inelastic collision rate coefficient vs temperature for fermionic molecules in the ro-vibronic ground state of $^{40}\text{K}^{87}\text{Rb}$. For the lower decay coefficients, the collision rate coefficients were measured for molecules prepared in either $|-4, 1/2\rangle$ (closed circles) or the lowest energy state $|-4, 3/2\rangle$ (open triangles). We observe the loss rate increases linearly with temperature for spin-polarized molecules, which verifies that the dominant collision channel is p -wave. A linear fit (solid line) to the $|-4, 1/2\rangle$ data yields the temperature-dependent loss rate to be $1.2(3) \cdot 10^{-5} \text{ cm}^3/\text{s}/\text{Kelvin}$. For the $|-4, 3/2\rangle$ case, where the collisional loss can only be due to chemically reactive scattering, the loss rate is similar. The dotted and dashed lines are theoretical predictions from the QT model and MQDT (describe in the text), respectively. In contrast, when the molecular sample is prepared in a mixture of two hyperfine spin states, $|-4, 1/2\rangle$ and $|-4, 3/2\rangle$ (filled squares), s -wave collisions dominate. Here we observe a temperature-independent decay rate that is 10 – 100 times higher than for the spin polarized case.

We repeated this measurement for molecules in the lowest hyperfine state $|-4, 3/2\rangle$ (open triangles in Fig. 10.5). The data again show $\beta \propto T$ with a slope of $1.1(3) \cdot 10^{-5} \text{ cm}^3/\text{s}/\text{Kelvin}$, similar to that measured for molecules in the $|-4, 1/2\rangle$ state. However, in the case of $|-4, 3/2\rangle$ molecules, hyperfine state-changing collisions are no longer possible and the only possible loss channels

are the three chemical reactions discussed earlier. Thus, we find that the rate of chemical reactions is determined by the p -wave angular momentum barrier and the chemical reaction barrier must be below the collision energy. This suggests that these reactions are barrierless and can thus occur freely at ultralow temperatures. However, we cannot distinguish among the three possible exothermic mechanisms at this time. Meanwhile, the fact that the same loss rate is observed for both $|-4, 1/2\rangle$ and $|-4, 3/2\rangle$ state molecules suggests that chemical reactions dominate the loss in these ground-state molecular collisions.

To understand the loss rates, we again use the MQDT model introduced in section 10.2 to estimate the rates where the collision process is characterized by combining the p -wave barrier and a van der Waals inter-molecular potential. The MQDT formalism for p -wave collision is provided by Z. Idziaszek and P. Julienne [116], where they derived the loss rate analytically and gave $\beta = (11.48 \cdot \text{Im}(a))^3 (k_B T/h)$, where $\text{Im}(a)$ can be replaced by l_{vdw} in Eq. 10.2. Based on $C_6 = 16130$ a.u. for KRb-KRb (calculated by S. Kotochigova), $\beta = 0.8(1) \cdot 10^{-5} \text{ cm}^3/\text{s/Kelvin}$, which is close to the experimental result.

In addition, we also use a simple quantum threshold (QT) model developed by Quéméner and Bohn to estimate the rate [117]. (This same model will be used in the next chapter when describing inelastic dipolar collisions.) The inelastic collisional cross section for indistinguishable particles (a factor of 2 bigger than the distinguishable particle case) is given quantum mechanically by

$$\sigma_{L,m_L}^{in} = \frac{\hbar^2 \pi}{\mu E_c} |T_{L,m_L}^{in}|^2, \quad (10.6)$$

where E_c is the collisional energy and T_{L,m_L}^{in} is the inelastic transition matrix. In the QT model, the maximum loss rate is determined by setting the $|T|^2$ matrix to unity for the collisional energy E_c at the height of the p -wave barrier V (i.e. chemical reaction proceeds with unit probability once the molecules pass through

the barrier.) When the collisional energy is below the height of the p -wave barrier, the loss is suppressed and the rate scales linearly with collisional energy (temperature) by the Bethe-Wigner threshold law. In this regime, $|T_{L,m_L}^{in}|^2 = (E_c/V)^{L+1/2}$. Since the p -wave barrier height is directly related to the attractive van der Waals potential (characterized by C_6), the QT model gives an upper limit for the rate coefficient to be

$$\frac{\pi}{4} \left(\frac{3^{17} \mu^3 C_6^3}{\hbar^{10}} \right)^{1/4} k_B T. \quad (10.7)$$

For KRB, $\beta = 1.5(1) \cdot 10^{-5} \text{ cm}^3/\text{s/Kelvin}$, which again agrees well with our experimental measurement (Fig. 10.5).

These simple theories, which both provide reasonable agreement with our molecule-molecule collisional loss measurements, suggest that chemical reaction rates are strongly influenced by the long-range interactions. This opens intriguing control possibilities as the long-range interaction can be controlled by selecting quantum states and tuning collision energies.

10.3.2 s -wave Collisions

Reaction rates should be dramatically different if molecules are prepared in a mixture of different hyperfine states as s -wave scattering is now allowed. We measured the inelastic collision rates for ro-vibronic ground-state molecules that were prepared in a roughly 50-50 incoherent mixture of the two hyperfine spin states $| - 4, 3/2 \rangle$ and $| - 4, 1/2 \rangle$. The time-dependent number density of trapped molecules was measured for both spin states. We observed the same loss rate for both states, consistent with loss due to collisions between distinguishable molecules in different spin states. The rate coefficient is determined to be $1.9(4) \cdot 10^{-10} \text{ cm}^3/\text{s}$, independent of temperature, as shown in closed squares in Fig. 10.5. In comparison to our measurements for p -wave collisions between spin-polarized

molecules, the *s*-wave collision rate between molecules in different hyperfine states is 10 - 100 times larger for a similar temperature range.

As in the atom-molecule *s*-wave collisions, molecule-molecule *s*-wave inelastic collision rates can be estimated using the MQDT model. Here, the relevant length scale is determined by the inter-molecular van der Waals potential without any angular momentum barrier [85]. We assume that when the molecules approach each other within the van der Waals length, chemical reactions take place and remove these entrant molecules with a near-unity probability. The universal loss rate coefficient predicts a β value of $0.8 \cdot 10^{-10} \text{ cm}^3/\text{s}$, which is about half of the experimentally observed value. This difference suggests that short-range physics may play some role in the loss dynamics. An enhancement in the rate coefficient (up to the energy-dependent unitarity limit, which is $4 \cdot 10^{-10} \text{ cm}^3/\text{s}$ for a gas at 400 nK) is possible if there is a partial reflection of the colliding species back into the entrance channel. The reflected amplitude interferes with the incoming amplitude and can either increase or decrease the rate coefficient from its “universal” value. Additional theory and experiment are needed to explore this possibility [116].

Together the results presented here allow us to draw the conclusion that we have observed barrierless chemical reactions in the short range, with the rates determined completely by long-range scattering dynamics dictated by quantum statistics, angular momentum barriers, and threshold laws. In particular, these studies show that chemical reactions can proceed with high rates in the ultracold regime, and that, furthermore, it will be possible to experimentally control the reaction rates because they depend primarily on long-range interactions. And most importantly, with our understanding of the intrinsic collisional molecular lifetime, we can now turn on an applied electric field and begin to study electric dipole-dipole collisions.

Chapter 11

Electric Dipole-Dipole Collisions

In the last chapter, we investigated density- and temperature-dependent lifetime of our fermionic ro-vibronic ground-state molecules, which is on the order of a second. Finally, we are ready to turn on an electric field to manipulate a unique property of polar molecules – their large and tunable electric dipole moment. After working with alkali atoms and weakly bound Feshbach molecules for many years, where their magnetic moment is about $\sim 1 \mu_b$ and their electric dipole moment is essentially zero, it took some getting used to molecules with an electric dipole moment and essentially zero magnetic dipole moment. In this chapter, I will start by introducing technical things we learned while working with electric dipoles and then discuss some of the exciting first results of electric-field controlled dipolar collisions.

11.1 Working with Electric Dipoles

The induced dipole moment of our polar molecules is directly related to the applied external electric field. Figure 11.1 shows the induced dipole moment vs electric field from the permanent electric dipole moment (0.574 Debye) and the rotational constant ($h \cdot 1.1139$ GHz) we measured previously (Chapter 8.3). We typically work with an electric field up to ~ 5.0 kV/cm (corresponding to a dipole moment up to ~ 0.21 Debye.)

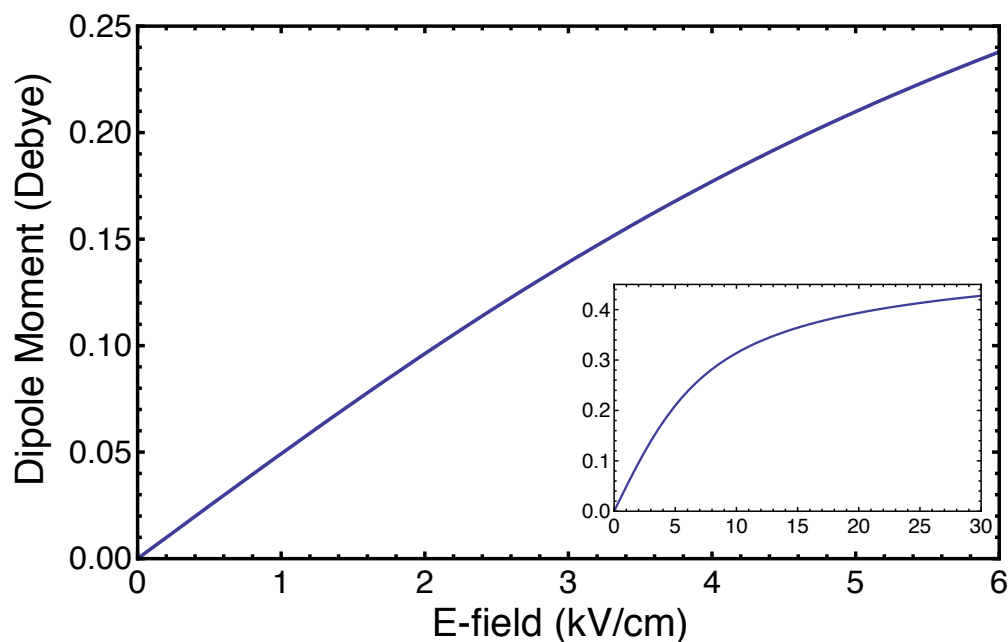


Figure 11.1: Calculated KRb induced dipole moment vs electric field for the permanent dipole moment of 0.574 Debye and the rotational constant of $h \cdot 1.1139$ GHz that we measured[15]. A larger range of dipole moment vs electric field is shown in the inset.

11.1.1 E-field Gradients

The electric field at our molecules is provided by a pair of parallel voltage plates (see Fig. 3.2). However, due to the machining precision of a spacer/holder in between the plates plus gluing the two plates to the holder, the plates may not be perfectly parallel. We first suspected this when we saw a shift in the molecular cloud equilibrium position when we turned on the electric field to increasing values (see Fig. 11.2). This shift occurred in the weak direction of a single-beam optical trap (perpendicular to the field direction). We then estimated the electric-field gradient that could arise from a slight tilt between two plates. First, to a good approximation within the range of our applied electric field, we consider electric field mixing of only $N = 0$ and $N = 1$ rotational states. The induced dipole

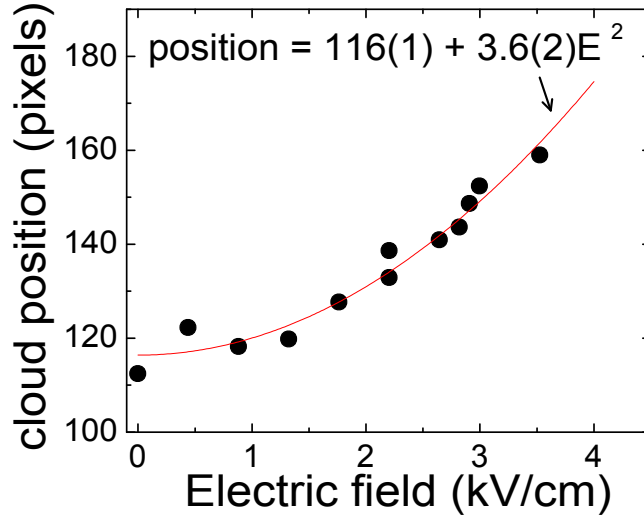


Figure 11.2: An electric-field gradient pushes the molecular cloud in the weak direction of the optical trap confinement. Each camera pixel is $5.4 \mu\text{m}$ in our system. For this data, the electric field is turned on for 40 ms. For a given duration, the cloud position shift is proportional to the gradient force which in turns is proportional to the square of the applied electric field. We fitted the shift to the quadratic term of the electric field that is $20 \mu\text{m}/(\text{kV}/\text{cm})^2$ and backed out the amount of electric-field gradient.

moment, $\langle d \rangle$, is

$$\langle d \rangle \approx \frac{d}{\sqrt{3}} \sqrt{\frac{(\varepsilon/\varepsilon_0)^2}{3 + (\varepsilon/\varepsilon_0)^2}}, \quad (11.1)$$

where d is the permanent electric dipole moment, ε is the applied electric field, and $\varepsilon_0 = 3.85 \text{ kV}/\text{cm}$ is the critical electric field (see Chapter 8.3 for definition) for KRb. The force on the molecules from the electric field is

$$F = -\frac{d}{dx} (\langle \vec{d} \rangle \cdot \vec{\varepsilon}) = -\langle d \rangle \cdot \frac{d\varepsilon}{dx} - \varepsilon \frac{\partial \langle d \rangle}{\partial \varepsilon} \frac{\partial \varepsilon}{\partial x} \approx -2 \cdot \frac{d}{\sqrt{3}} \frac{\varepsilon/\varepsilon_0}{\sqrt{3 + (\varepsilon/\varepsilon_0)^2}} \cdot \frac{d\varepsilon}{dx} \propto \varepsilon^2 \quad (11.2)$$

The shift of the cloud position (Fig. 11.2) was due to the electric-field gradient (countered by an optical confinement in this weak direction which we neglected here). From Eq. 11.1, we can calculate the gradient we measured in Fig. 11.2 to be $1.8 \text{ V}/\text{cm}^2$ per $1 \text{ kV}/\text{cm}$ applied. The gradient could be explained by the separation of the E-field plates varying by $\sim 25 \mu\text{m}$ over 1 cm . This is a very

small fraction of the 1.35 cm average separation. From the experimental point of view, this shows that the effect of the molecular electric dipole moment is huge!

11.1.2 Fringing Fields and a Non-symmetric Ground Plane

We overcame the electric-field gradient problem by replacing the single beam optical dipole trap with a crossed-beam dipole trap. This increased the optical trap confinement in the weak direction by a factor of 10 in trap frequency and reduced the effect of the field gradient in this direction. (This was done for all the data presented in Chapter 9 and 10). However, we encountered yet another gradient problem in the direction parallel to the electric field (Fig. 11.3) (also the direction of gravity) where the optical confinement is the strongest. Since any tilt of the field plates would only cause a gradient in the horizontal plane, we needed to investigate other possible causes.

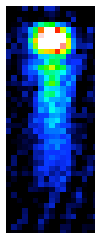


Figure 11.3: Molecule leaking out of the optical trap due to a strong electric field gradient at an applied field 3 kV/cm.

We considered the effect of the electric-field plates being surrounded by ground planes and also the fringing field from the finite-size of the plates. In our first attempt to apply an electric field, we had the top plate grounded and applied a high voltage to the bottom plate. We did this because the top plate was close to a grounded microwave coil (Fig. 3.2) and we were concerned about dielectric breakdown. This asymmetry in the applied voltage combined with the existence of nearby grounded magnetic coils give rise to a vertical E-field gradient. The

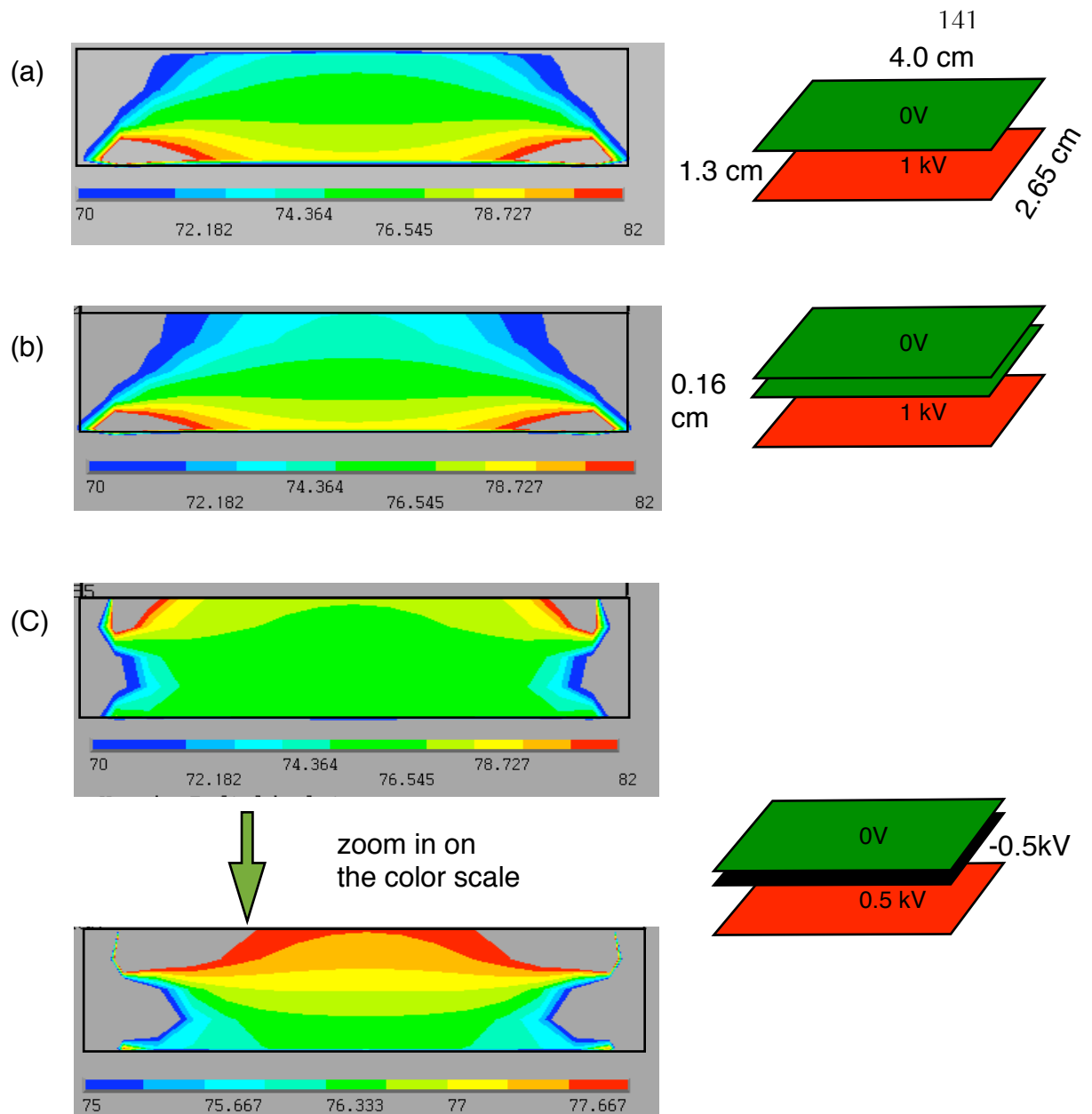


Figure 11.4: Finite-element simulation of the electric-field for our E-field plates surrounded by nearby grounded planes. (a) We ground the top E-field plate and apply 1 kV at the bottom plate. The plates are surrounded by a grounded 3-D box that is 4 times bigger than the space spanned by the plates and their separation. The field gradient is ~ -40 V/cm² at the geometric center. (b) Add an additional ground plane that is only 0.16 cm away from the top plate. The field gradient is the same as in (a) but the effect of fringe fields moves closer to the center. (c) When splitting the voltage difference between the top and the bottom plates, the field gradient is reduced to 10 V/cm² and changes sign.

electric field will be stronger near the bottom plate and weaker near the top plate because field lines can go to grounded planes other than our grounded E-field top plate. To estimate the magnitude of the gradient, we performed a finite-element calculation using a program called ANSYS. To illustrate the importance of each effect – finite size, fringing field, position of the grounded plane, and the non-symmetric applied voltage, we calculated the field by adding one effect at a time (we ignored the glass cell between the plates here). Our simulation was the following: 1. We first considered grounding the top plate, and applying 1kV at the bottom plate. In the model, the pair of E-field plates are surrounded by a grounded 3-D box that is four times the size of the space spanned by the area and the separation of the plates. At the geometric center between the plates, the field gradient is about -40 V/cm^2 while the E-field $\sim 750 \text{ V/cm}$ (Fig. 11.4(a)). Experimentally we observed a gradient that is about a factor 2 larger than the simulation based on the crude geometry. 2. Adding a grounded plane to simulate the effect of the nearby microwave coil, the gradient at the center did not change, but the fringing fields cause the region of uniform field strength to shrink farther from the edge of the plates. Therefore, if the cloud is off-centered in the horizontal plane, the gradient can be larger and pointed in a direction other than the vertical direction. (Fig. 11.4(b)) 3. When split the applied voltage difference between the two plates (top plate at -0.5 kV and bottom plate at 0.5 kV), the sign of the vertical gradient changed and the magnitude is reduced to $<10 \text{ V/cm}^2$. (Fig. 11.4(c)) This is obviously an improvement which we have experimentally verified as well. However, to get the lowest possible field gradient, we need to further experimentally vary the voltage ratio of the two plates due to the non-symmetric ground planes, which comes from surrounding metal coils in the experiments.

11.2 Inelastic Dipolar Collisions

With the two electric-field gradient problems solved, we can turn up the electric field in our experiment without perturbing cloud position. Previously, we have established that at zero applied electric field (zero effective dipole moment) our indistinguishable fermionic KRb collide via p -wave followed by a near-unity probability of chemical reactions in the short range (Chapter 10.3.1). This collision is universal in the sense that the collision rate is solely determined by the long-range potential, $\frac{\hbar^2 L(L+1)}{2\mu R^2} - \frac{C_6}{R^6}$, which in our case sets the p -wave barrier height. By tuning the external electric field, we can adjust the effective dipole moment, $\langle d \rangle$, of the molecules (Fig. 11.1), which introduces an additional $\frac{-C_3}{R^3}$ term from the electric dipole-dipole interaction in our gas. The C_3 is given by

$$C_3 = 2 \cdot (-1)^{m_L} \sqrt{(2L+1)(2L'+1)} \begin{pmatrix} L & 2 & L' \\ -m_L & 0 & m'_L \end{pmatrix} \begin{pmatrix} L & 2 & L' \\ 0 & 0 & 0 \end{pmatrix} \frac{\langle d \rangle^2}{4\pi\epsilon_0}. \quad (11.3)$$

This term shows that dipole-dipole interactions 1. are long-range and anisotropic among m_L s and 2. mix different partial waves of the same parity.

The anisotropy nature of the dipole-dipole interaction directly modifies the long-range potential according to the m_L s (shown in Fig. 11.5 and 11.6). At zero effective dipole moment, the p -wave barrier for $m_L = 0$ and $m_L = \pm 1$ channels are degenerate (dashed line in Fig. 11.5). As the effective dipole moment is turned on, e.g. 0.1 D (Fig. 11.5), the p -wave barrier is raised for the $m_L = \pm 1$ “side-by-side” repulsive collision channels and is lowered for the $m_L = 0$ “head-to-tail” attractive channel. Figure 11.6 shows the anisotropy of the barrier heights vs dipole moment. At a large effective dipole moment (> 0.15 D), the $m_L = \pm 1$ p -wave barrier is again lowered, which is due to mixing with higher partial waves, e.g. $L = 3, 5, 7, \dots$. As seen in the QT model (developed by Quémener and Bohn

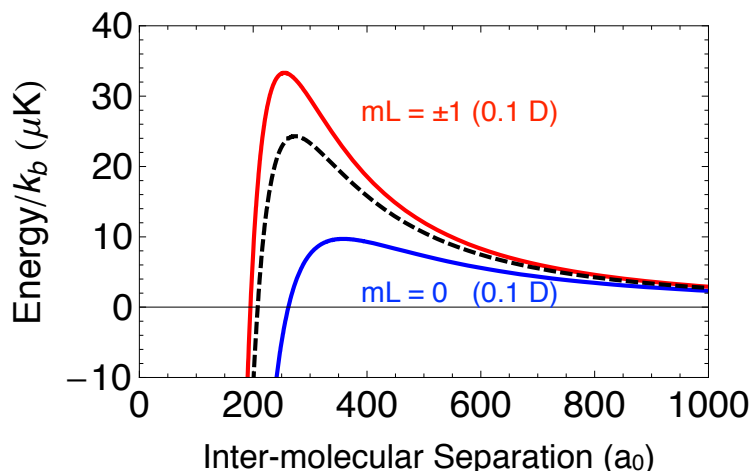


Figure 11.5: Adiabatic energy curves of the long-range part of KRb-KRb potential (shown for p -wave, $L = 1$). When no electric field is applied, the p -wave barriers for angular momentum projection $m_L = 0, 1, -1$ are degenerate (central dashed line). When an electric field is applied and the dipole moment of the molecules is turned on, e.g. 0.1 Debye, the barriers for the $m_L = \pm 1$ channels are raised (upper branch) and the barrier for the $m_L = 0$ channel is lowered (lower branch).

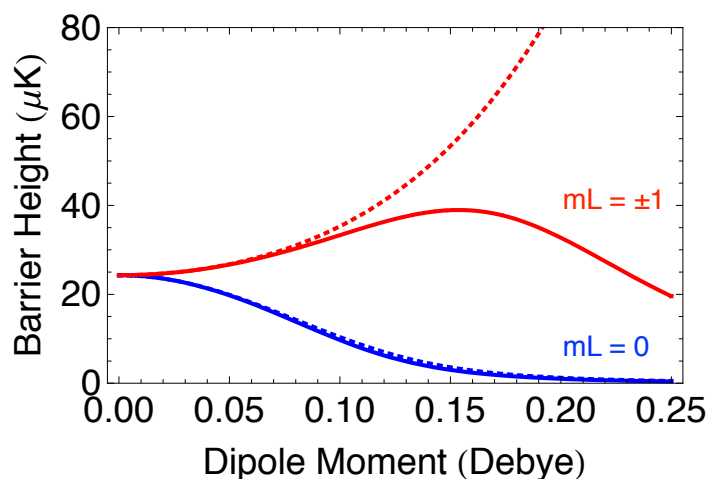


Figure 11.6: Barrier height vs effective dipole moment, $\langle d \rangle$. The solid lines are calculated using the adiabatic energies considering partial wave mixings up to $L = 7$. The $m_L = \pm 1$ barrier heights rise as the effective dipole moment increases. However, when $d > 0.15$ D, the barrier height reduces due to mixings of higher partial waves. The $m_L = 0$ barrier height reduces as the dipole moment increases. The dashed lines are the diabatic curves without partial wave mixing.

in [117]) in Chapter 10.3.1, the inelastic collision rate is directly determined by the collisional barrier. The consequence of dipolar interaction in our gas, which is a thermal average of all collisional channels, is that the inelastic collision is dominated by the lowering of the p -wave barrier due to the attractive $m_L = 0$ channel.

11.2.1 Anisotropy of Losses

Experimentally, we measured the inelastic loss rate of molecules as a function of the effective dipole moment (Fig. 11.7(a)). At small dipole moments, we observed a constant inelastic collision rate that is mainly determined by the attractive van der Waals potential. At large dipole moments, the inelastic loss rate grows with $\langle d \rangle^p$ where p was measured to be 6.1(0.4) (fitting to an additional offset, $c + A \cdot \langle d \rangle^p$, $p = 6.7(0.5)$). The large power-law dependence came from the steep lowering of the barrier height due to the attractive dipolar interaction (the $m_L = 0$ channel, Fig. 11.7(b)). This can be seen in the analytical formulas of the QT model, which predicts the inelastic rate for the attractive channel ($m_L = 0$) to grow as $\langle d \rangle^6$ in the limit of $\frac{C_3}{R^3} \gg \frac{C_6}{R^6}$ [117]. For the repulsive channel ($m_L = \pm 1$) in the limit of $\frac{C_3}{R^3} \gg \frac{C_6}{R^6}$, but before mixings with higher partial waves become important (i.e. in the diabatic limit), the inelastic rate decreases as $\langle d \rangle^{-6}$ [117].

Our experimental data (Fig. 11.7(a)) shows qualitative agreement with the QT model (Fig. 11.7(b)). However, the quantitative agreement can be made if we introduce two fitting parameters, pb and C_6 , to adjust the QT predicted loss rate. “ pb ” is the probability or an overall scaling factor of the loss at the short-range and C_6 determines the zero E-field barrier height, hence the molecular loss rate at low dipole moment. For the best fit to our data, we found $pb = 0.34(12)$ and $C_6 = 31000(16000)$ a.u.

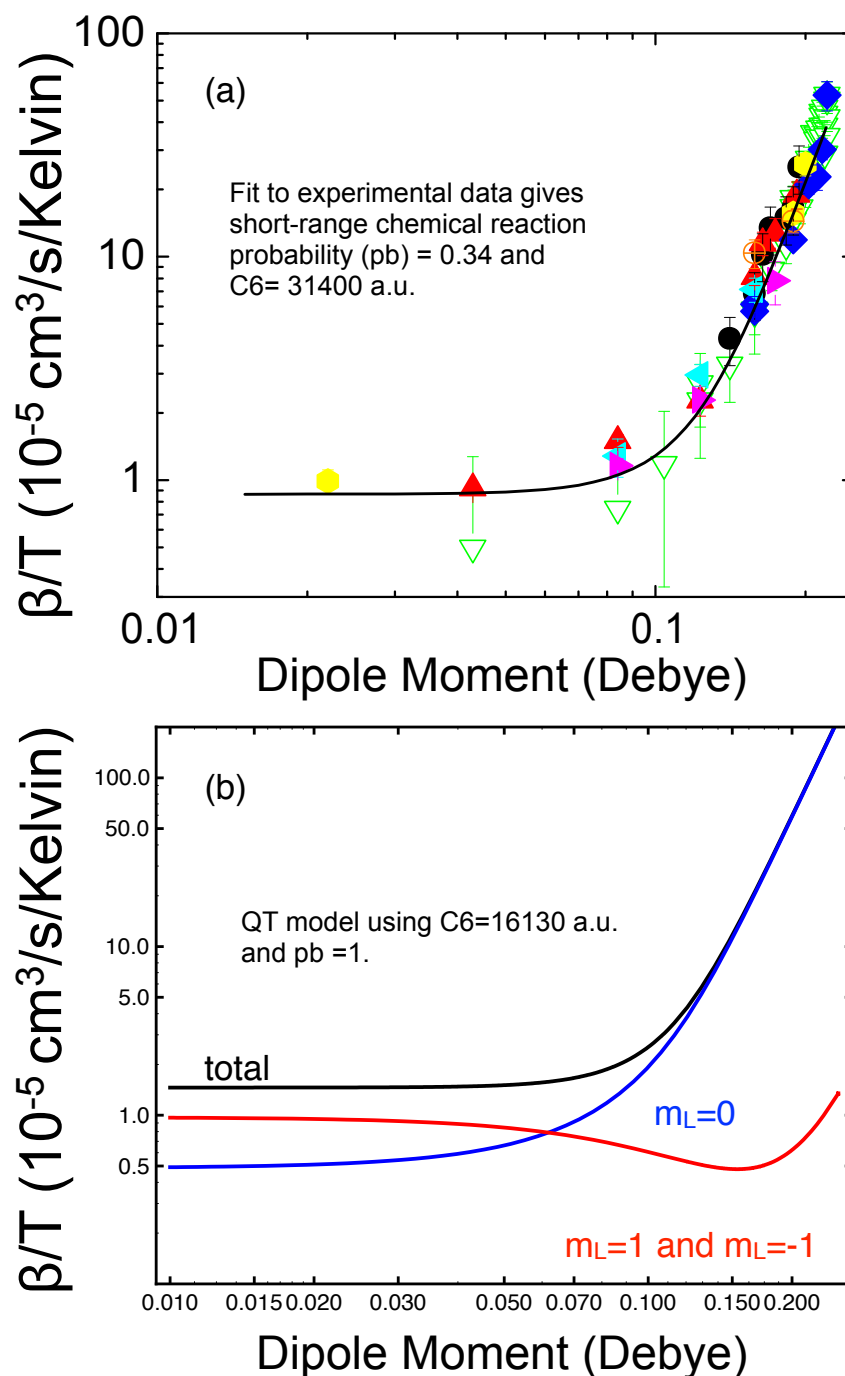


Figure 11.7: Inelastic dipolar collisions. (a) experimental observation of inelastic losses as the function of effective dipole moment. The fit is based on the QT loss rate model that uses p -wave barrier height from the adiabatic energies with an overall scaling factor of 0.34 and a van der Waals dispersion coefficient $C_6 = 31400 \text{ a.u.}$ (b) Predicted loss rate from the QT model based on $C_6 = 16130 \text{ a.u.}$ (C_6 was calculated by S. Kotochigova) and $\text{pb} = 1$. The QT model is a “classical” calculation tailored to describe quantum threshold laws. Contributions of $m_L = 0$ and $m_L = \pm 1$ respectively are shown, where the losses we observe at high dipole moments are predominately from the attractive $m_L = 0$ channel.

11.2.2 Anisotropic Heating

Along with the strong inelastic loss of molecules with an increasing dipole moment, we observed strong corresponding heating for the trapped gas (Fig. 11.9). Here, we consider the heating of the trapped gas due to the so-called “anti-evaporation” process from inelastic collisions. The main inelastic loss in our gas is two-body collisions ($\dot{n} = -\beta \cdot n^2$), where the losses of molecules occur most frequently at the densest part of the cloud. Since our gas is in a harmonic trap, the highest density region coincides with the coldest part of the gas (Fig. 11.8(a)). Therefore, when molecules in this region are removed, the average temperature of the remaining gas increases (Fig. 11.8(b)). However, there is a competing cooling effect due to $\beta \propto T$ for p -wave collisions. To understand the overall heating of the gas, we will consider both the cooling and the heating effects from p -wave inelastic collisions.

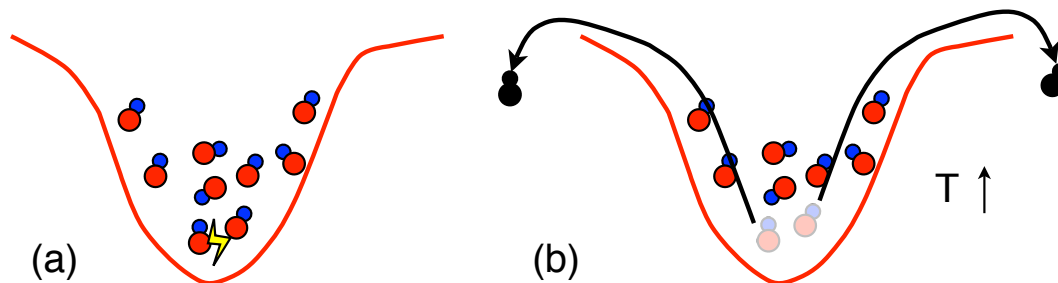


Figure 11.8: Anti-evaporation of a trapped gas due to inelastic collisions. (a) inelastic collisions occur most frequently at the densest part of the gas which coincides with the coldest part of the gas. (b) when molecules in the coldest part are lost, the average temperature of the remaining gas increases.

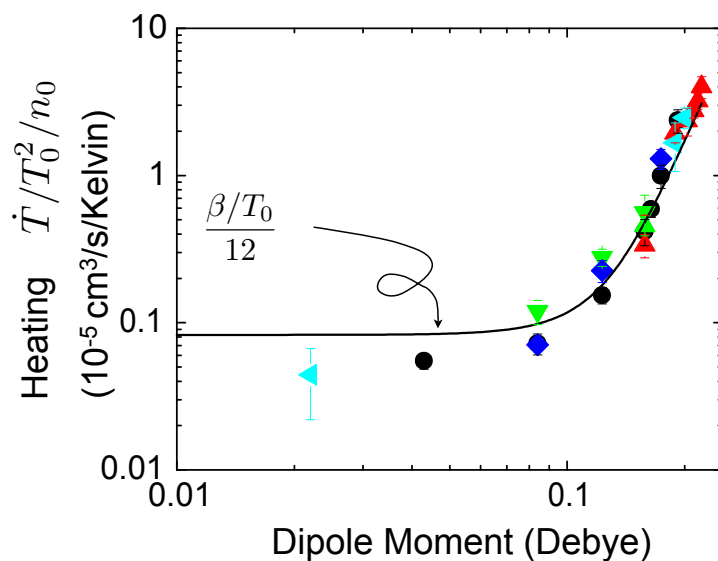


Figure 11.9: Strong heating in our trapped gas when an E-field is turned on. This is due to “anti-evaporation” where the cold molecules from the densest part of the gas are preferentially removed. The line to the data is the inelastic dipolar loss (β/T_0) we measured in Fig. 11.7(a) scaled by 1/12, which confirms that the heating comes directly from inelastic collisions.

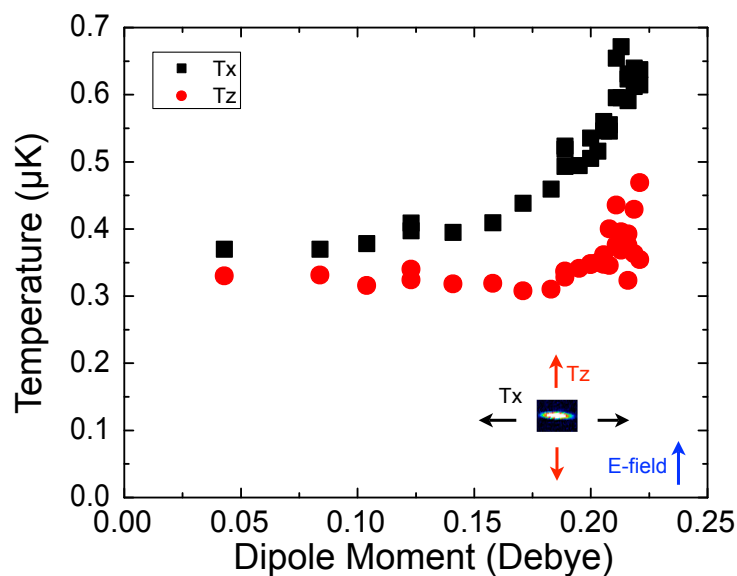


Figure 11.10: Individual temperatures, along (T_z) and perpendicular (T_x) to the applied E-field direction. We observed heating in T_x and cooling in T_z (for small dipole moment). The anisotropy of heating can be explained by the dominate dipolar collisions in our gas being the attractive channel.

Here I will only give a brief sketch of the analysis as it is still ongoing during the time when this thesis is written. The temperature evolution of the gas follows directly from the inelastic collision events. (Temperature changes due to elastic dipolar collisions are ignored here.) For each collisional event, two molecules are removed from the trap with an energy change including their kinetic energy and potential energy. The energy change is then re-distributed among the remaining molecules in the trap. Furthermore, the rate of the temperature change is the product of the temperature change per collision and the inelastic collision rate, which depends on the collisional energy (temperature). Our model based on this analysis shows that the initial heating rate of the gas is directly related to the inelastic loss rate β by an overall factor of 1/12. Plotting $\frac{\beta}{T_0}/12$ where $\frac{\beta}{T_0}$ was fitted from the loss measurement in Fig. 11.7(a), we see that the overall heating is explained well by the model sketched above (Fig. 11.9).

Beside an overall heating due to the inelastic collisions, we also observed an anisotropy in the heating along (T_z) and perpendicular (T_x) to the applied E-field direction (along z). In Fig. 11.10, we measured the molecular gas temperature T_z and T_x as a function of the effective dipole moment after holding the gas in the trap for 100 ms while the E-field is on. This measurement shows that T_z is mostly cooled during the 100 ms period, while T_x is heated. At large effective dipole moment, both directions are heated. This effect makes sense because we expect cooling in T_z and heating in T_x for the attractive dipolar collisions, which are the dominant collisions in our 3D gas. However, at high effective dipole moment, we observed a rise in the temperatures for both directions. This could be due to strong elastic dipolar collisions that transfer energy from one direction to another.

11.3 Elastic Dipolar Collisions

The presence of an E-field not only turns on strong inelastic collisions, but also turns on long-range elastic dipolar collisions. The elastic collisions due to the long-range dipole-dipole interaction is independent of the short-range elastic cross section, which for fermionic molecules is expected to be small and suppressed (as is the case of fermionic K atoms [118]). However, the long-range elastic collision cross section could still be large. In Chapter 1.3.1 (Fig. 1.1), I have summarized the result of universal elastic dipolar collisions from Bohn *et al.* [36] (a similar result was also obtained in [119]), where the elastic collisional cross section in the threshold regime (applicable to our experiments) is directly proportional to $\langle d \rangle^4$. This result was derived using the Born approximation, where the elastic collisional cross section written in a generic T -matrix form is

$$\sigma^{el} = \frac{\pi l_D^2}{k^2} \sum_{L,L',m_L} |T_{L,L'}^{m_L}|^2. \quad (11.4)$$

Here l_D is the dipole length as defined in Chapter 1.3 and k is the wavenumber of the relative motion of the dipoles. An additional factor of 2 needs to be multiplied for collisions of indistinguishable particles. The T -matrix labelled by angular momentum channels is an integral of both the angular part ($C_{L,L'}^{m_L}$) and the radial part ($\Gamma_{L,L'}$) of the wavefunction.

$$T_{L,L'}^{m_L} = -k \cdot C_{L,L'}^{m_L} \cdot \Gamma_{L,L'}, \quad (11.5)$$

where

$$C_{L,L'}^{m_L} = (-1)^{m_L} \sqrt{(2L+1)(2L'+1)} \begin{pmatrix} L & 2 & L' \\ -m_L & 0 & m'_L \end{pmatrix} \begin{pmatrix} L & 2 & L' \\ 0 & 0 & 0 \end{pmatrix} \quad (11.6)$$

and

$$\Gamma_{L,L'} = \begin{cases} \frac{4}{L(L+1)}, & \text{if } L = L' \\ \frac{4}{3(L+1)(L+2)}, & \text{if } L = L' + 2. \end{cases} \quad (11.7)$$

From the explicit expression of $C_{L,L'}^{m_L}$, it is clear that dipolar collisions only mix states of the same parity. Therefore, Bohn *et al.* have derived the elastic collisional cross section for the even and the odd partial waves separately, which depend on the quantum statistics of the collisions.

In our case, the indistinguishable fermionic molecules collide via odd partial waves, and $\sigma^{el} = 6.7 \cdot 10^{-8} \frac{\langle d \rangle^4}{\text{Debye}^4} \text{ cm}^2$. This collisional cross section is quite large. For a comparison, Rb elastic collision cross section with a background scattering length $\sim 100 a_0$ is $8\pi a_0^2 = 7 \cdot 10^{-12} \text{ cm}^2$, which is equivalent to the elastic dipolar cross section of fermionic polar molecules with a dipole moment of 0.1 Debye. Since the total cross section is a sum of many angular momentum channels, we can directly compute the contribution of each partial-wave channel using the Born approximation. The contribution of $L = 1, m_L = 0$ is $\sim 60 \%$, $L = 1, m_L = \pm 1$ is $\sim 15 \%$ each, and higher partial waves is only $\sim 10\%$ of the total cross section.

Using the theoretical predicted elastic dipolar collision cross section and the measured inelastic collision rates, we can calculate the ratio of the elastic to inelastic dipolar collision rate ($\beta_{elastic} = \langle \sigma^{el} \cdot v \rangle / \beta_{inelastic}$) as a function of the effective dipole moment. From Fig. 11.11, we can see that the highest ratio is slightly above 1 around 0.13 D, which suggests that further evaporative cooling using dipolar collisions is difficult without suppressing the inelastic collisions.

11.4 Cross-dimensional Rethermalization

We attempt to measure the elastic dipolar collision cross section in the ultracold gas of ground-state KRb by using the method of cross-dimensional rethermalization [120]. The molecules are confined in a pancake-shaped optical dipole trap with an aspect ratio of ~ 7 . Typical trap frequencies for the optical dipole trap used are $f_x \approx f_y \approx 40 \text{ Hz}$ and $f_z \approx 280 \text{ Hz}$. For these measurements, we heat the gas in one direction, T_z (or T_x), by modulating the trap at twice the

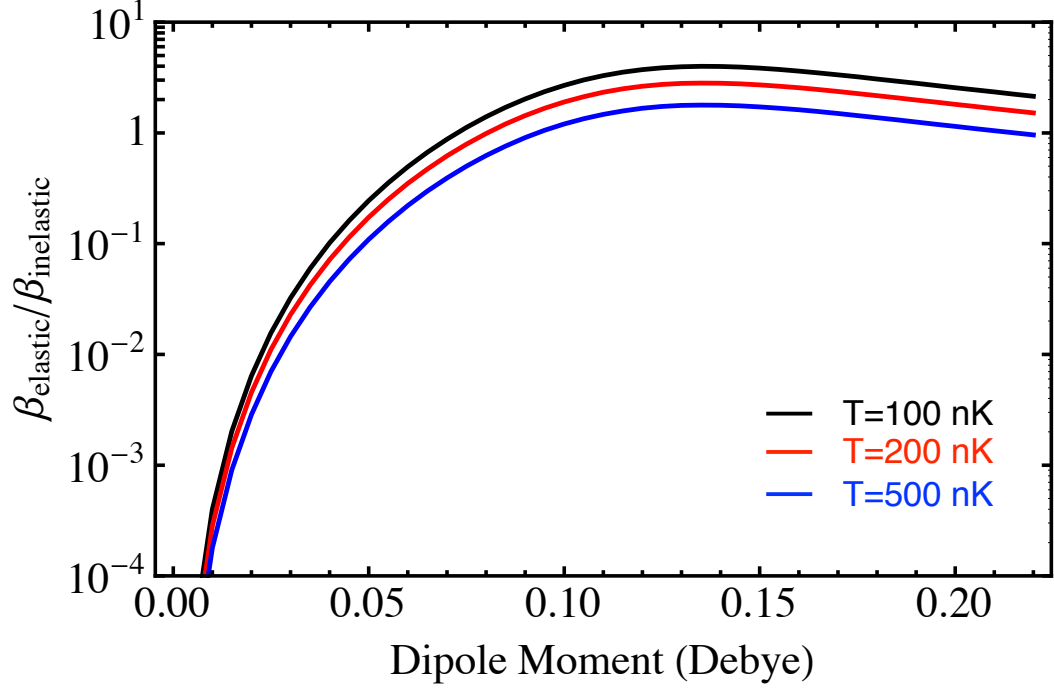


Figure 11.11: The ratio of the elastic dipolar collision rate $\beta_{elastic}$ (calculated based on [36]) to the inelastic dipolar collision rate $\beta_{inelastic}$ (measured) vs the effective dipole moment for KRb. The elastic collision rate scales as $T^{1/2}$ and the inelastic collision rate scales as T . The ratio is the highest (> 1) around 0.13 D.

frequency $2f_z$ (or $2f_x$) to excite a breathing mode and watch the gas come to a thermal equilibrium due to energy transfer from one direction to another. The rethermalization time scale (τ_{reth}) can be related to the elastic collisional cross section by an expression $\tau_{reth} = (n \cdot \sigma^{el} \cdot v)/\alpha$, where n is the density, v is the mean velocity of the gas, and α accounts for the geometric factor of the number of collisions required for rethermalization. However, in this measurement inelastic collisions that cause anisotropic heating could mimic the rethermalization effect of elastic collisions. This is because both types of collisions affect the thermal anisotropy of the gas.

Figure 11.12 shows data from our cross-dimensional rethermalization measurements. For the data in the first column, we heat the gas in the z direction. We observe the temperatures in two directions (T_x, T_z) approach each other rapidly

as a function of the dipole moment. However, the temperatures eventually cross each other. For the data in the second column, we heat the gas in the x and y directions simultaneously. However, the temperature in the x direction and the z direction never appear to “rethermalize.” This can be explained mostly by the inelastic anisotropic heating model as briefly sketched out in section 11.2.2, which reinforces our observation of the anisotropic nature of inelastic collisions. Furthermore, our preliminary attempt to fit the data based on the model shows good agreement (Fig. 11.12) if we include the elastic collision term $(\langle d \rangle^4)$ as described in the last section 11.3) to describe the temperature behavior of the rethermalization data.

Although the data analysis for the dipolar collisions is still on-going, I have presented here our measurements that show both the long-range and the anisotropic nature of dipole-dipole interactions.

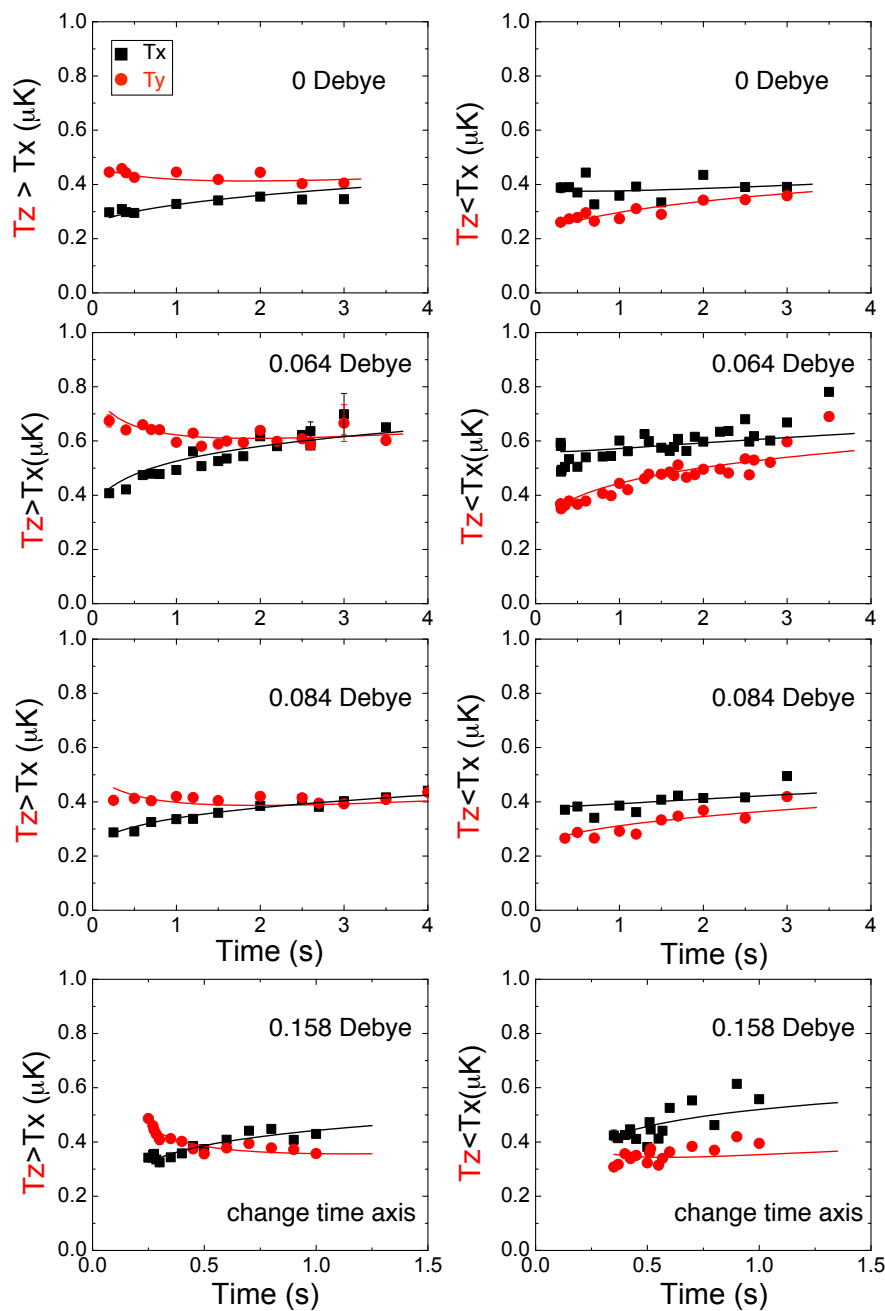


Figure 11.12: Sample data for cross-dimensional rethermalization. For initial $T_z > T_x$, we observed T_x and T_z approach each other with a decreasing time scale as a function of dipole moment. However, the temperatures did not come to a thermal equilibrium but rather crossed each other. For initial $T_x > T_z$, the two temperatures never rethermalize and even diverge. This is mainly due to anisotropic heating for attractive dipolar collisions in our 3D gas.

Chapter 12

Conclusions and Future Directions

12.1 Conclusion

In this thesis, I have presented the story of the experimental realization of a high phase-space-density gas of $^{40}\text{K}^{87}\text{Rb}$ polar molecules and some initial investigations of ultracold molecular chemical reactions and dipolar collisions. These ultracold polar molecules at a few hundreds of nanoKelvins and at 1.4 times their Fermi temperature are created with two coherent transfer steps from an ultracold gas mixture of ^{40}K and ^{87}Rb . The first step is to transfer atoms into extremely weakly bound molecules (molecular size of $\sim 250 a_0$) near a Fano-Feshbach resonance. The second step is to transfer these weakly bound molecules into their ro-vibronic ground state (molecular size of $\sim 8 a_0$) with a coherent two-photon Raman technique. The first step was demonstrated in J. Zirbel's thesis to be about 25% efficient [24], while the second step demonstrated in this thesis is 90% efficient. We verified that the ro-vibronic ground-state molecules are polar by measuring their permanent electric dipole moment spectroscopically.

Once molecules were prepared in the ro-vibronic ground state, we implemented a scheme to manipulate their molecular internal hyperfine state and explored various scenarios of ultracold collisions. We observed ultracold chemical reactions between KRb and K. Once all the atoms were removed, we observed fermionic $^{40}\text{K}^{87}\text{Rb}$ lifetime on the order of a second. This is limited by molecule-

molecule p -wave collisions where molecules tunnel through a $24 \mu\text{K}$ p -wave angular momentum barrier followed by a near-unity probability of chemical reactions. Furthermore, we began to explore the polar nature of the molecules in collisions through their large and tunable electric dipole moment. For large effective dipole moments, we observed enhanced inelastic collision rates that scale as d^6 and anisotropic heating of the gas.

12.2 Future Work

An immediate goal in the future is to evaporate our near quantum degenerate gas further and begin to realize some of the many exciting proposals for molecular quantum gases. To evaporate our gas of spin-polarized fermionic polar molecules, one can turn on strong elastic dipolar collisions by applying an electric field. However, our work so far suggests that strong inelastic collisions also happen at the same time as the elastic collisions, and these cause significant loss and heating of the gas. Therefore, to reach quantum degeneracy, inelastic collisions need to be suppressed. One way is to suppress the dominant inelastic channel (the attractive dipole-dipole interactions) by going to reduced dimensions [110]. Figure 12.1 shows the ratio of the elastic to inelastic dipolar collision rate when the attractive collision channel is completely suppressed. This ratio is favorable for further evaporative cooling of KRb when the effective dipole moment is increased. Given the advances we have already made and all that we have learned, I am optimistic that the future of a quantum gas of polar molecules is bright and exciting!

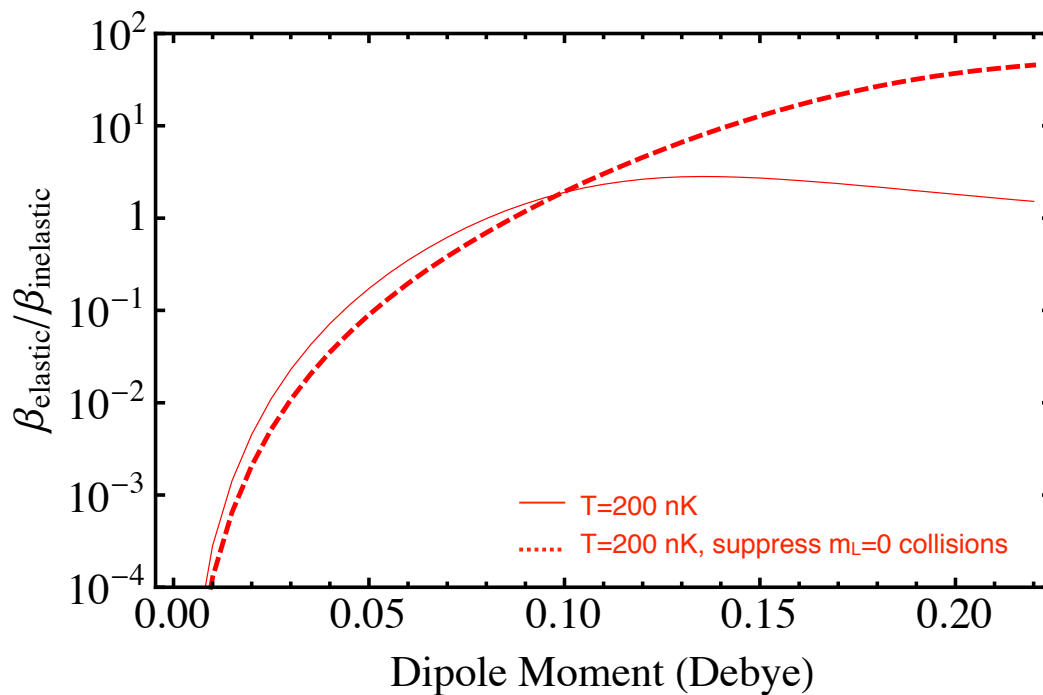


Figure 12.1: The ratio of the elastic dipolar collision rate (calculated based on [36]) to the inelastic dipolar collision rate (measured) vs the effective dipole moment for KRb at 200 nK. The dashed line shows the ratio when the $m_L = 0$ collisional channel is completely suppressed. In this case, the ratio increases dramatically with increasing dipole moment, which makes dipolar collisions favorable for further evaporative cooling of our KRb gas.

Bibliography

- [1] P. G. H. Sandars, Measurability of the Proton Electric Dipole Moment, *Phys. Rev. Lett.* **19**, 1396 (1967).
- [2] M. G. Kozlov and L. N. Labzowsky, Parity violation effects in diatomics, *Journal of Physics B: Atomic, Molecular and Optical Physics* **28**, 1933 (1995).
- [3] E. R. Hudson, H. J. Lewandowski, B. C. Sawyer, and J. Ye, Cold Molecule Spectroscopy for Constraining the Evolution of the Fine Structure Constant, *Phys. Rev. Lett.* **96**, 143004 (2006).
- [4] C. Ticknor and J. L. Bohn, Long-range scattering resonances in strong-field-seeking states of polar molecules, *Phys. Rev. A* **72**, 032717 (2005).
- [5] A. V. Avdeenkov and J. L. Bohn, Linking Ultracold Polar Molecules, *Phys. Rev. Lett.* **90**, 043006 (2003).
- [6] R. V. Krems, Cold controlled chemistry, *Physical Chemistry Chemical Physics* **10**, 4079 (2008).
- [7] D. DeMille, Quantum Computation with Trapped Polar Molecules, *Phys. Rev. Lett.* **88**, 067901 (2002).
- [8] A. Andre, D. DeMille, J. M. Doyle, M. D. Lukin, S. E. Maxwell, P. Rabl, R. J. Schoelkopf, and P. Zoller, A coherent all-electrical interface between polar molecules and mesoscopic superconducting resonators, *Nat. Phys.* **2**, 636 (2006).
- [9] S. F. Yelin, K. Kirby, and R. Côté, Schemes for robust quantum computation with polar molecules, *Phys. Rev. A* **74**, 050301 (2006).
- [10] M. A. Baranov, Theoretical progress in many-body physics with ultracold dipolar gases, *Physics Reports* **464**, 71 (2008).
- [11] L. Santos, G. V. Shlyapnikov, P. Zoller, and M. Lewenstein, Bose-Einstein Condensation in Trapped Dipolar Gases, *Phys. Rev. Lett.* **85**, 1791 (2000).

- [12] G. Pupillo, A. Micheli, H. Büchler, and P. Zoller, Condensed Matter Physics with Cold Polar Molecules, *arXiv:0805.1896v1* (2008).
- [13] M. H. Anderson, J. R. Ensher, M. R. Matthews, C. E. Wieman, and E. A. Cornell, Observation of Bose-Einstein condensation in a dilute atomic vapor, *Science* **269**, 198 (1995).
- [14] B. DeMarco and D. S. Jin, Onset of Fermi degeneracy in a trapped atomic gas, *Science* **285**, 1703 (1999).
- [15] K.-K. Ni, S. Ospelkaus, M. H. G. de Miranda, A. Pe'er, B. Neyenhuis, J. J. Zirbel, S. Kotochigova, P. S. Julienne, D. S. Jin, and J. Ye, A High Phase-Space-Density Gas of Polar Molecules, *Science* **322**, 231 (2008).
- [16] E. A. Donley, N. R. Claussen, S. T. Thompson, and C. Wieman, Atom-molecule coherence in a Bose-Einstein condensate, *Nature* **417**, 529 (2002).
- [17] C. A. Regal, C. Ticknor, J. L. Bohn, and D. S. Jin, Tuning p -wave interactions in an ultracold Fermi gas of atoms, *Phys. Rev. Lett.* **90**, 053201 (2003).
- [18] J. J. Zirbel, Ultracold Fermionic Feshbach Molecules, Ph.D. thesis, University of Colorado - Boulder, 2008.
- [19] M. T. Hummon, W. C. Campbell, H.-I. Lu, E. Tsikata, Y. Wang, and J. M. Doyle, Magnetic trapping of atomic nitrogen (^{14}N) and cotrapping of NH ($X^3\Sigma^-$), *Phys. Rev. A* **78**, 050702 (2008).
- [20] S. Y. T. van de Meerakker, P. H. M. Smeets, N. Vanhaecke, R. T. Jongma, and G. Meijer, Deceleration and Electrostatic Trapping of OH Radicals, *Phys. Rev. Lett.* **94**, 023004 (2005).
- [21] B. C. Sawyer, B. K. Stuhl, D. Wang, M. Yeo, and J. Ye, Molecular Beam Collisions with a Magnetically Trapped Target, *Phys. Rev. Lett.* **101**, 203203 (2008).
- [22] J. M. Sage, S. Sainis, T. Bergeman, and D. DeMille, Optical Production of Ultracold Polar Molecules, *Phys. Rev. Lett.* **94**, 203001 (2005).
- [23] C. Ospelkaus, S. Ospelkaus, L. Humbert, P. Ernst, K. Sengstock, and K. Bongs, Ultracold Heteronuclear Molecules in a 3D Optical Lattice, *Phys. Rev. Lett.* **97**, 120402 (2006).
- [24] J. J. Zirbel, K.-K. Ni, S. Ospelkaus, J. P. D'Incao, C. E. Wieman, J. Ye, and D. S. Jin, Collisional Stability of Fermionic Feshbach Molecules, *Phys. Rev. Lett.* **100**, 143201 (2008).

- [25] K. Winkler, F. Lang, G. Thalhammer, P. v. d. Straten, R. Grimm, and J. H. Denschlag, Coherent Optical Transfer of Feshbach Molecules to a Lower Vibrational State, *Phys. Rev. Lett.* **98**, 043201 (2007).
- [26] S. Ospelkaus, A. Pe'er, K. K. Ni, J. J. Zirbel, B. Neyenhuis, S. Kotochigova, P. S. Julienne, J. Ye, and D. S. Jin, Efficient state transfer in an ultracold dense gas of heteronuclear molecules, *Nat. Phys.* **4**, 622 (2008).
- [27] C. Amiot, The K Rb $(2)^3\Sigma^+$ Electronic State, *Journal of Molecular Spectroscopy* **203**, 126 (2000).
- [28] A. Pashov, O. Docenko, M. Tamanis, R. Ferber, H. Knockel, and E. Tiemann, Coupling of the $X^1\Sigma^+$ and a $^3\Sigma^+$ states of K Rb, *Phys. Rev. A* **76**, 022511 (2007).
- [29] J. G. Danzl, E. Haller, M. Gustavsson, M. J. Mark, R. Hart, N. Bouloufa, O. Dulieu, H. Ritsch, and H.-C. Nagerl, Quantum Gas of Deeply Bound Ground State Molecules, *Science* **321**, 1062 (2008).
- [30] F. Lang, K. Winkler, C. Strauss, R. Grimm, and J. H. Denschlag, Ultracold Triplet Molecules in the Rovibrational Ground State, *Phys. Rev. Lett.* **101**, 133005 (2008).
- [31] S. Kotochigova, private communication.
- [32] J. Stuhler, A. Griesmaier, T. Koch, M. Fattori, T. Pfau, S. Giovanazzi, P. Pedri, and L. Santos, Observation of Dipole-Dipole Interaction in a Degenerate Quantum Gas, *Phys. Rev. Lett.* **95**, 150406 (2005).
- [33] T. Lahaye, T. Koch, B. Frohlich, M. Fattori, J. Metz, A. Griesmaier, S. Giovanazzi, and T. Pfau, Strong dipolar effects in a quantum ferrofluid, *Nature* **448**, 672 (2007).
- [34] T. Lahaye, J. Metz, B. Fröhlich, T. Koch, M. Meister, A. Griesmaier, T. Pfau, H. Saito, Y. Kawaguchi, and M. Ueda, d-Wave Collapse and Explosion of a Dipolar Bose-Einstein Condensate, *Phys. Rev. Lett.* **101**, 080401 (2008).
- [35] T. Lahaye, C. Menotti, L. Santos, M. Lewenstein, and T. Pfau, The physics of dipolar bosonic quantum gases, *arXiv:0905.0386* (2009).
- [36] J. L. Bohn, M. Cavagnero, and C. Ticknor, Quasi-universal dipolar scattering in cold and ultracold gases, *New Journal of Physics* **11**, 055039 (2009).
- [37] A. V. Gorshkov, P. Rabl, G. Pupillo, A. Micheli, P. Zoller, M. D. Lukin, and H. P. Büchler, Suppression of Inelastic Collisions Between Polar Molecules With a Repulsive Shield, *Phys. Rev. Lett.* **101**, 073201 (2008).

- [38] L. P. Pitaevskii, in *Proceedings of the International School of Physics - Enrico Fermi*, edited by M. Inguscio, S. Stringari, and C. E. Wieman (IOS Press, ADDRESS, 1999), p. 287.
- [39] H. P. Büchler, E. Demler, M. Lukin, A. Micheli, N. Prokof'ev, G. Pupillo, and P. Zoller, Strongly Correlated 2D Quantum Phases with Cold Polar Molecules: Controlling the Shape of the Interaction Potential, *Phys. Rev. Lett.* **98**, 060404 (2007).
- [40] G. Pupillo, A. Griessner, A. Micheli, M. Ortner, D.-W. Wang, and P. Zoller, Cold Atoms and Molecules in Self-Assembled Dipolar Lattices, *Phys. Rev. Lett.* **100**, 050402 (2008).
- [41] S. Chu, Nobel Lecture: The manipulation of neutral particles, *Rev. Mod. Phys.* **70**, 685 (1998).
- [42] C. N. Cohen-Tannoudji, Nobel Lecture: Manipulating atoms with photons, *Rev. Mod. Phys.* **70**, 707 (1998).
- [43] W. D. Phillips, Nobel Lecture: Laser cooling and trapping of neutral atoms, *Rev. Mod. Phys.* **70**, 721 (1998).
- [44] P. Domokos and H. Ritsch, Collective Cooling and Self-Organization of Atoms in a Cavity, *Phys. Rev. Lett.* **89**, 253003 (2002).
- [45] G. Morigi, P. W. H. Pinkse, M. Kowalewski, and R. de Vivie-Riedle, Cavity Cooling of Internal Molecular Motion, *Phys. Rev. Lett.* **99**, 073001 (2007).
- [46] B. L. Lev, A. Vukics, E. R. Hudson, B. C. Sawyer, P. Domokos, H. Ritsch, and J. Ye, Prospects for the cavity-assisted laser cooling of molecules, *Phys. Rev. A* **77**, 023402 (2008).
- [47] M. D. D. Rosa, Laser-cooling molecules - Concept, candidates, and supporting hyperfine-resolved measurements of rotational lines in the A-X(0,0) band of CaH, *Eur. Phys. J. D* **31**, 395 (2004).
- [48] B. K. Stuhl, B. C. Sawyer, D. Wang, and J. Ye, Magneto-optical Trap for Polar Molecules, *Phys. Rev. Lett.* **101**, 243002 (2008).
- [49] J. D. Weinstein, R. deCarvalho, T. Guillet, Bretislav Friedrich, and J. M. Doyle, Magnetic trapping of calcium monohydride molecules at millikelvin temperatures, *Nature* **395**, 148 (1998).
- [50] L. D. van Buuren, C. Sommer, M. Motsch, S. Pohle, M. Schenk, J. Bayerl, P. W. H. Pinkse, and G. Rempe, Electrostatic Extraction of Cold Molecules from a Cryogenic Reservoir, *Phys. Rev. Lett.* **102**, 033001 (2009).
- [51] H. L. Bethlem, G. Berden, and G. Meijer, Decelerating Neutral Dipolar Molecules, *Phys. Rev. Lett.* **83**, 1558 (1999).

- [52] S. D. Hogan, D. Sprecher, M. Andrist, N. Vanhaecke, and F. Merkt, Zeeman deceleration of H and D, *Phys. Rev. A* **76**, 023412 (2007).
- [53] E. Narevicius, A. Libson, C. G. Parthey, I. Chavez, J. Narevicius, U. Even, and M. G. Raizen, Stopping Supersonic Beams with a Series of Pulsed Electromagnetic Coils: An Atomic Coilgun, *Phys. Rev. Lett.* **100**, 093003 (2008).
- [54] R. Fulton, A. I. Bishop, M. N. Shneider, and P. F. Barker, Controlling the motion of cold molecules with deep periodic optical potentials, *Nat Phys* **2**, 465 (2006).
- [55] S. A. Rangwala, T. Junglen, T. Rieger, P. W. H. Pinkse, and G. Rempe, Continuous source of translationally cold dipolar molecules, *Phys. Rev. A* **67**, 043406 (2003).
- [56] M. S. Elioff, J. J. Valentini, and D. W. Chandler, Subkelvin Cooling NO Molecules via "Billiard-like" Collisions with Argon, *Science* **302**, 1940 (2003).
- [57] M. Gupta and D. Herschbach, Slowing and Speeding Molecular Beams by Means of a Rapidly Rotating Source, *The Journal of Physical Chemistry A* **105**, 1626 (2001).
- [58] J. van Veldhoven, H. L. Bethlem, and G. Meijer, ac Electric Trap for Ground-State Molecules, *Phys. Rev. Lett.* **94**, 083001 (2005).
- [59] B. C. Sawyer, B. L. Lev, E. R. Hudson, B. K. Stuhl, M. Lara, J. L. Bohn, and J. Ye, Magneto-electrostatic Trapping of Ground State OH Molecules, *Phys. Rev. Lett.* **98**, 253002 (2007).
- [60] J. J. Gilijamse, S. Hoekstra, S. Y. T. van de Meerakker, G. C. Groenenboom, and G. Meijer, Near-Threshold Inelastic Collisions Using Molecular Beams with a Tunable Velocity, *Science* **313**, 1617 (2006).
- [61] K. Maussang, D. Egorov, J. S. Helton, S. V. Nguyen, and J. M. Doyle, Zeeman Relaxation of CaF in Low-Temperature Collisions with Helium, *Phys. Rev. Lett.* **94**, 123002 (2005).
- [62] E. R. Hudson, C. Ticknor, B. C. Sawyer, C. A. Taatjes, H. J. Lewandowski, J. R. Bochinski, J. L. Bohn, and J. Ye, Production of cold formaldehyde molecules for study and control of chemical reaction dynamics with hydroxyl radicals, *Phys. Rev. A* **73**, 063404 (2006).
- [63] K. M. Jones, E. Tiesinga, P. D. Lett, and P. S. Julienne, Ultracold photoassociation spectroscopy: Long-range molecules and atomic scattering, *Reviews of Modern Physics* **78**, 483 (2006).

- [64] D. Wang, J. Qi, M. F. Stone, O. Nikolayeva, H. Wang, B. Hattaway, S. D. Gensemer, P. L. Gould, E. E. Eyler, and W. C. Stwalley, Photoassociative Production and Trapping of Ultracold KRb Molecules, *Phys. Rev. Lett.* **93**, 243005 (2004).
- [65] M. W. Mancini, G. D. Telles, A. R. L. Caires, V. S. Bagnato, and L. G. Marcassa, Observation of Ultracold Ground-State Heteronuclear Molecules, *Phys. Rev. Lett.* **92**, 133203 (2004).
- [66] C. Haimberger, J. Kleinert, M. Bhattacharya, and N. P. Bigelow, Formation and detection of ultracold ground-state polar molecules, *Phys. Rev. A* **70**, 021402 (2004).
- [67] J. Deiglmayr, A. Grochola, M. Repp, K. Mörtlbauer, C. Glück, J. Lange, O. Dulieu, R. Wester, and M. Weidemüller, Formation of Ultracold Polar Molecules in the Rovibrational Ground State, *Phys. Rev. Lett.* **101**, 133004 (2008).
- [68] C. M. Dion, C. Drag, O. Dulieu, B. Laburthe Tolra, F. Masnou-Seeuws, and P. Pillet, Resonant Coupling in the Formation of Ultracold Ground State Molecules via Photoassociation, *Phys. Rev. Lett.* **86**, 2253 (2001).
- [69] A. J. Kerman, J. M. Sage, S. Sainis, T. Bergeman, and D. DeMille, Production of Ultracold, Polar RbCs* Molecules via Photoassociation, *Phys. Rev. Lett.* **92**, 033004 (2004).
- [70] J. Deiglmayr, P. Pellegrini, A. Grochola, M. Repp, R. Cote, O. Dulieu, R. Wester, and M. Weidemüller, Influence of a Feshbach resonance on the photoassociation of LiCs, *New Journal of Physics* **11**, 055034 (2009).
- [71] P. Pellegrini, M. Gacesa, and R. Côté, Giant Formation Rates of Ultracold Molecules via Feshbach-Optimized Photoassociation, *Phys. Rev. Lett.* **101**, 053201 (2008).
- [72] E. Kuznetsova, M. Gacesa, P. Pellegrini, S. F. Yelin, and R. Cote, Efficient formation of ground-state ultracold molecules via STIRAP from the continuum at a Feshbach resonance, *New Journal of Physics* **11**, 055028 (2009).
- [73] A. Pe'er, E. A. Shapiro, M. C. Stowe, M. Shapiro, and J. Ye, Precise Control of Molecular Dynamics with a Femtosecond Frequency Comb, *Phys. Rev. Lett.* **98**, 113004 (2007).
- [74] E. A. Cornell and C. E. Wieman, Nobel Lecture: Bose-Einstein condensation in a dilute gas, the first 70 years and some recent experiments, *Rev. Mod. Phys.* **74**, 875 (2002).
- [75] W. Ketterle, Nobel lecture: When atoms behave as waves: Bose-Einstein condensation and the atom laser, *Rev. Mod. Phys.* **74**, 1131 (2002).

- [76] L. Chen, High-Precision Spectroscopy of Molecular Iodine: From Optical Frequency Standards to Global Descriptions of Hyperfine Interactions and Associated Electronic Structure, Ph.D. thesis, University of Colorado - Boulder, 2005.
- [77] S. Foreman, Femtosecond Frequency Combs for Optical Clocks and Timing Transfer, Ph.D. thesis, University of Colorado - Boulder, 2007.
- [78] W. C. Stwalley, Stability of spin-aligned hydrogen at low temperatures and high magnetic fields: New field-dependent scattering resonance and predisociations, *Phys. Rev. Lett.* **37**, 1628 (1976).
- [79] E. Tiesinga, B. J. Verhaar, and H. T. C. Stoof, Threshold and resonance phenomena in ultracold ground-state collisions, *Phys. Rev. A* **47**, 4114 (1993).
- [80] S. Inouye, M. R. Andrews, J. Stenger, H.-J. Miesner, D. M. Stamper-Kurn, and W. Ketterle, Observation of Feshbach resonances in a Bose-Einstein condensate, *Nature* **392**, 151 (1998).
- [81] C. Chin, R. Grimm, P. Julienne, and E. Tiesinga, Feshbach Resonances in Ultracold Gases, *arXiv:0812.1496* (2008).
- [82] C. A. Regal and D. S. Jin, in *Advances in Atomic, Molecular, and Optical Physics* (Elsevier, London, 2006), Vol. 54, Chap. 1.
- [83] J. L. Roberts, N. R. Claussen, S. L. Cornish, E. A. D. and E. A. Cornell, and C. E. Wieman, Controlled collapse of a Bose-Einstein condensate, *Phys. Rev. Lett.* **86**, 4211 (2001).
- [84] K. E. Strecker, G. B. Partridge, A. G. Truscott, and R. Hulet, Formation and propagation of matter-wave soliton trains, *Nature* **417**, 150 (2002).
- [85] T. Kohler, K. Goral, and P. S. Julienne, Production of cold molecules via magnetically tunable Feshbach resonances, *Rev. Mod. Phys.* **78**, 1311 (2006).
- [86] C. A. Regal, C. Ticknor, J. L. Bohn, and D. S. Jin, Creation of ultracold molecules from a Fermi gas of atoms, *Nature* **424**, 47 (2003).
- [87] E. Hodby, S. T. Thompson, C. A. Regal, M. Greiner, A. C. Wilson, D. S. Jin, E. A. Cornell, and C. E. Wieman, Production efficiency of ultracold Feshbach molecules in bosonic and fermionic systems, *Phys. Rev. Lett.* **94**, 120402 (2005).
- [88] J. J. Zirbel, K.-K. Ni, S. Ospelkaus, T. L. Nicholson, M. L. Olsen, P. S. Julienne, C. E. Wieman, J. Ye, and D. S. Jin, Heteronuclear molecules in an optical dipole trap, *Phys. Rev. A* **78**, 013416 (2008).
- [89] P. S. Julienne, Ultracold molecules from ultracold atoms: a case study with the KRb molecule, *Faraday Discussions* **142**, 361 (2009).

- [90] S. Inouye, J. Goldwin, M. L. Olsen, C. Ticknor, J. L. Bohn, and D. S. Jin, Observation of Heteronuclear Feshbach Resonances in a Mixture of Bosons and Fermions, *Phys. Rev. Lett.* **93**, 183201 (2004).
- [91] F. Ferlaino, C. D’Errico, G. Roati, M. Zaccanti, M. Inguscio, G. Modugno, and A. Simoni, Feshbach spectroscopy of a K-Rb atomic mixture, *Phys. Rev. A* **73**, 040702 (2006).
- [92] C. Klempt, T. Henninger, O. Topic, J. Will, W. Ertmer, E. Tiemann, and J. Arlt, $^{40}\text{K}^{87}\text{Rb}$ Feshbach resonances: Modeling the interatomic potential, *Phys. Rev. A* **76**, 020701 (2007).
- [93] S. B. Papp and C. E. Wieman, Observation of Heteronuclear Feshbach Molecules from a ^{85}Rb – ^{87}Rb Gas, *Phys. Rev. Lett.* **97**, 180404 (2006).
- [94] S. Kotochigova, P. S. Julienne, and E. Tiesinga, Ab initio calculation of the KRb dipole moments, *Phys. Rev. A* **68**, 022501 (2003).
- [95] J. M. Brown and A. Carrington, in *Rotational spectroscopy of diatomic molecules* (Cambridge Univ., Cambridge, UK, 2003), pp. 224–230.
- [96] R. L. Roy and R. Bernstein, Dissociation Energy and Long-Range Potential of Diatomic Molecules from Vibrational Spacings of Higher Levels, *Journal of Chemical Physics* **52**, 3869 (1970).
- [97] W. C. Stwalley, The dissociation energy of the hydrogen molecule using long-range forces, *Chemical Physics Letters* **6**, 241 (1970).
- [98] D. Wang, Production of Ultracold Heteronuclear KRb Molecules, Ph.D. thesis, University of Connecticut, 2007.
- [99] S. Kotochigova, E. Tiesinga, and P. Julienne, Multi-channel modelling of the formation of vibrationally cold polar KRb molecules, *New Journal of Physics* **11**, 055043 (2009).
- [100] K.-K. Ni, S. Ospelkaus, D. J. Nesbitt, J. Ye, and D. S. Jin, A dipolar gas of ultracold molecules, *Physical Chemistry Chemical Physics* **11**, 9626 (2009).
- [101] R. Wynar, R. S. Freeland, D. J. Han, C. Ryu, and D. J. Heinzen, Molecules in a Bose-Einstein Condensate, *Science* **287**, 1016 (2000).
- [102] K. Bergmann, H. Theuer, and B. W. Shore, Coherent population transfer among quantum states of atoms and molecules, *Rev. Mod. Phys.* **70**, 1003 (1998).
- [103] W. C. Stwalley, Efficient conversion of ultracold Feshbach-resonance-related polar molecules into ultracold ground state ($X^1\Sigma v = 0 J = 0$) molecules, *Eur. Phys. J. D* **31**, 221 (2004).

- [104] S. Ospelkaus, K.-K. Ni, M. H. G. de Miranda, B. Neyenhuis, D. Wang, S. Kotochigova, P. S. Julienne, D. S. Jin, and J. Ye, Ultracold polar molecules near quantum degeneracy, *Faraday Discussions* **142**, 351 (2009).
- [105] S. T. Cundiff and J. Ye, Colloquium: Femtosecond optical frequency combs, *Rev. Mod. Phys.* **75**, 325 (2003).
- [106] M. Aymar and O. Dulieu, Calculation of accurate permanent dipole moments of the lowest $^1\Sigma^+$ states of heteronuclear alkali dimers using extended basis sets, *The Journal of Chemical Physics* **122**, 204302 (2005).
- [107] B. Arora, M. S. Safronova, and C. W. Clark, Determination of electric-dipole matrix elements in K and Rb from Stark shift measurements, *Phys. Rev. A* **76**, 052516 (2007).
- [108] S. Ospelkaus, K.-K. Ni, G. Quéméner, D. Wang, B. Neyenhuis, M. H. G. de Miranda, J. L. Bohn, J. Ye, and D. S. Jin, Controlling the hyperfine state of rovibronic ground-state polar molecules, *submitted* (2009).
- [109] J. Aldegunde, B. A. Rivington, P. S. Żuchowski, and J. M. Hutson, Hyperfine energy levels of alkali-metal dimers: Ground-state polar molecules in electric and magnetic fields, *Phys. Rev. A* **78**, 033434 (2008).
- [110] A. Micheli, G. Pupillo, H. P. Büchler, and P. Zoller, Cold polar molecules in two-dimensional traps: Tailoring interactions with external fields for novel quantum phases, *Phys. Rev. A* **76**, 043604 (2007).
- [111] N. R. Cooper and G. V. Shlyapnikov, Stable Topological Superfluid Phase of Ultracold Polar Fermionic Molecules, *Phys. Rev. Lett.* **103**, 155302 (2009).
- [112] C. Amiot, Laser-induced fluorescence of Rb_2 : The $(1)\Sigma_g^+(X)$, $(2)^1\Sigma_g^+$, $(1)^1\Pi_u(B)$, $(1)^1\Pi_g$, and $(2)^1\Pi_u(C)$ electronic states, *The Journal of Chemical Physics* **93**, 8591 (1990).
- [113] S. Falke, I. Sherstov, E. Tiemann, and C. Lisdat, The $A^1\Sigma_u^+$ state of K_2 up to the dissociation limit, *The Journal of Chemical Physics* **125**, 224303 (2006).
- [114] P. S. Julienne and F. H. Mies, Collisions of ultracold trapped atoms, *J. Opt. Soc. Am. B* **6**, 2257 (1989).
- [115] E. P. Wigner, On the Behavior of Cross Sections Near Thresholds, *Phys. Rev.* **73**, 1002 (1948).
- [116] Z. Idziaszek and P. Julienne, manuscript in preparation (2009).
- [117] G. Quéméner and J. Bohn, manuscript in preparation (2009).

- [118] B. DeMarco, J. L. Bohn, J. P. Burke, Jr., M. Holland, and D. S. Jin, Measurement of p -wave threshold law using evaporatively cooled fermionic atoms, *Phys. Rev. Lett.* **82**, 4208 (1999).
- [119] S. Hensler, J. Werner, A. Griesmaier, P. Schmidt, A. Görlitz, T. Pfau, S. Giovanazzi, and K. Rzażewski, Dipolar relaxation in an ultra-cold gas of magnetically trapped chromium atoms, *Applied Physics B: Lasers and Optics* **77**, 756 (2003).
- [120] C. R. Monroe, E. A. Cornell, C. A. Sackett, C. J. Myatt, and C. Wieman, Measurement of Cs-Cs elastic scattering at $T = 30 \mu\text{K}$, *Phys. Rev. Lett.* **70**, 414 (1993).
- [121] B. DeMarco, Quantum Behavior of an Atomic Fermi Gas, Ph.D. thesis, University of Colorado - Boulder, 2001.

Appendix A

Sample Mathematica Code

Throughout the thesis, I have presented a few calculations, for examples, the KRb Stark shifts and the KRb-KRb long-range adiabatic potentials. Those calculations were based on a very simple code in Mathematica that were setup with the help from D. Meiser and T. Rosenband. In addition to the calculations shown in this thesis, the same code have been adapted to calculate different Hamiltonians that use the basis set of angular momentum states $|J, m_J\rangle$, e.g. Zeeman energies of ground-state and excited-state K and Rb, etc. I found the code very useful and would like to share it here. I will take the KRb Stark shift calculation as an example. The parts labeled “list of J and mJ values to be evaluated” and “define H in reduced units” are the main parts that can be adapted for any Hamiltonian of interest.

```
In[1]:= Clear[B, mu, d, r, Efield, E0, Ef];
Off[ClebschGordan: "phy"]
Off[ClebschGordan: "tri"]
Needs["NumericalCalculus`"]
Needs["NonlinearRegression`"]
Needs["LinearRegression`"]
Needs["ErrorBarPlots`"]
```

constants and units

```
In[8]:= hbar = 1.054571628 10-34 (*J s*); amu = 1.660538782 10-27 (*kg*);
c = 299792458 (*m s-1); kb = 1.3806504 10-23 (*J K-1); e = 1.602176462 10-19
(*C*); a0 = 0.5291772083 10-10 (*m*); mKRb =  $\frac{(87 \times 40)}{(87 + 40)}$  amu;

In[9]:= SetOptions[Plot, BaseStyle -> {FontFamily -> "Arial", FontSize -> 18},
PlotStyle -> {Thick}, TicksStyle -> Directive[Black, 10], Frame -> True];
SetOptions[ListPlot, BaseStyle -> {FontFamily -> "Times", FontSize -> 18},
PlotStyle -> {Thick}, TicksStyle -> Directive[Black, 10], Frame -> True];
```

list of J and mJ values to be evaluated

```
In[11]:= mjlist[j_] := Table[{j, mj}, {mj, 0, j}];
jlist[Jmax_] := Table[j, {j, Jmax, 0, -1}];
JmJ[Jmax_] := Flatten[mjlist /@ jlist[Jmax], 1]

In[14]:= JmJ[5]

Out[14]= {{5, 0}, {5, 1}, {5, 2}, {5, 3}, {5, 4}, {5, 5}, {4, 0}, {4, 1}, {4, 2}, {4, 3},
{4, 4}, {3, 0}, {3, 1}, {3, 2}, {3, 3}, {2, 0}, {2, 1}, {2, 2}, {1, 0}, {1, 1}, {0, 0}}

In[15]:= Jmax = 5; (*define how many Js I want to take into consideration*)
```

define H in reduced units

```
In[16]:= (*write hamiltonian in the energy unit of B,
write Efield is in the unit of critical field=B/d*)

In[17]:= hamiltonian2[{jprime_, mjprime_}, {j_, mj_}] :=
j * (j + 1) * KroneckerDelta[j, jprime] * KroneckerDelta[mj, mjprime] -
Ef *  $\sqrt{(2j+1)(2jprime+1)}$  (-1)mj ThreeJSymbol[{j, -mj}, {1, 0}, {jprime, mjprime}] *
ThreeJSymbol[{j, 0}, {1, 0}, {jprime, 0}];
HH2 = Outer[hamiltonian2[#1, #2] &, JmJ[Jmax], JmJ[Jmax], 1];
ev = Eigenvalues[HH2]

In[20]:= (* figure out ordering of eigenvalues at non-zero Efield *)
evOrder = Ordering[ev /. Ef -> 1 // N]
evo = ev[[evOrder]];

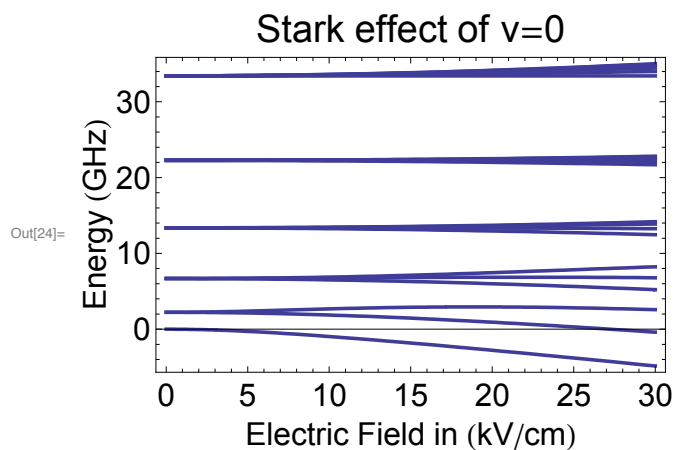
Out[20]= {16, 11, 17, 7, 12, 18, 4, 8, 13, 19, 2, 5, 9, 14, 20, 1, 3, 6, 10, 15, 21}
```

$v=0$ of singlet ground

```
In[22]:= singlet = {d → 0.22591382365886692 e a0, B →  $\frac{6.6836}{6} 10^9 \text{ hbar } 2 \pi$ };
(*dipole moment and rotational constant*)
```

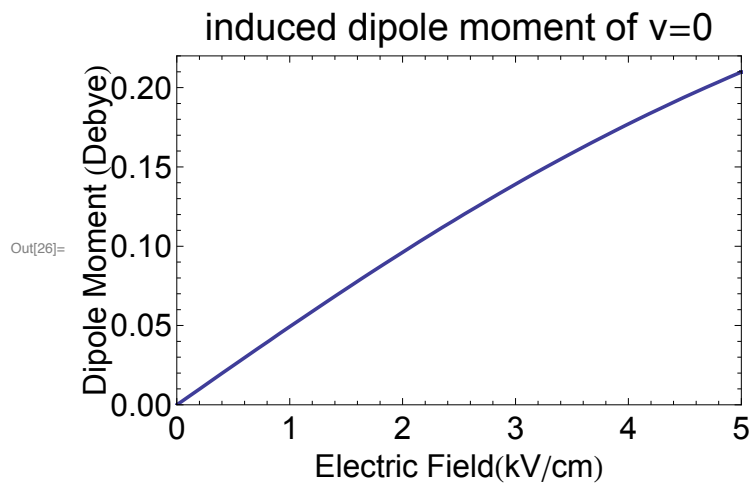
```
In[23]:= E0 =  $\frac{B}{d}$  /. singlet; (*define critical electric field for singlet vibrational ground state*)
```

```
In[24]:= StarkPlot = Plot[ $\frac{B}{10^9 \text{ hbar } 2 \pi} \text{ evo} /. \{Ef \rightarrow (Eff 10^5) / E0\} /. \text{singlet},$ 
{Eff, 0, 30}, PlotLabel → "Stark effect of  $v=0$ ",
FrameLabel → {"Electric Field in (kV/cm)", "Energy (GHz)"}]
```



Dipole Moment (Debye) vs Electric Field (kV/cm)

```
In[26]:= DvEPlot = Plot[-D[(evo[[1]]) 0.574, Ef] /. Ef -> 10^5  $\frac{Eff}{E0}$  /. singlet,
  {Eff, 0, 5}, PlotLabel -> "induced dipole moment of v=0", FrameLabel ->
  {"Electric Field(kV/cm)", "Dipole Moment (Debye)"}, PlotRange -> {{0, 5}, {0, 0.22}}]
```



Appendix B

Tapered Amplifier Design

One of my very first projects as a graduate student was to design a tapered amplifier (TA) mount for Eagleyard TA chips that come in a C-mount. With the help from Josh Zirbel, Scott Papp, and Carl Wieman, our design has now become the standard JILA design. The major difference between previous designs and our design is the use of clamping to make the electric connections to the tapered amplifier, rather than soldering. The design of the overall geometry and the flexure mount that is used for fine adjustment of the collimation is similar to Brian DeMarco's design [121].

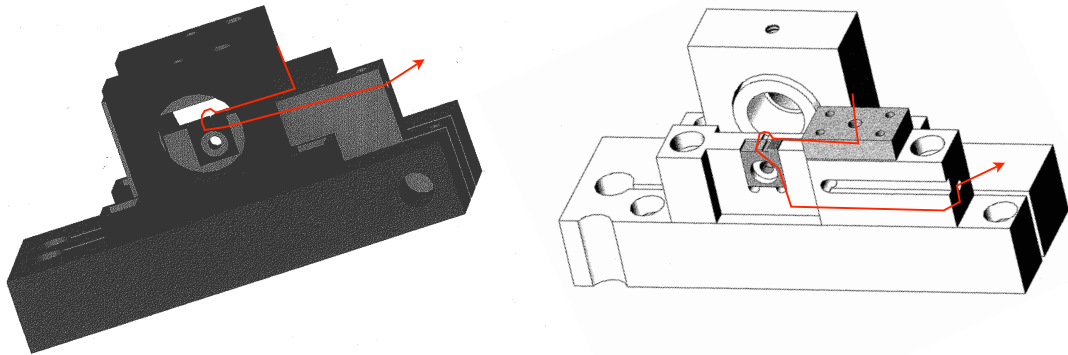


Figure B.1: Overview of the TA mechanical design. The red arrow shows the direction of the current from an electric wire through the screw hole to the clamp, then through the lead of the TA chip to the body of the chip, and finally to the wire that is connected on the side of the TA holder.

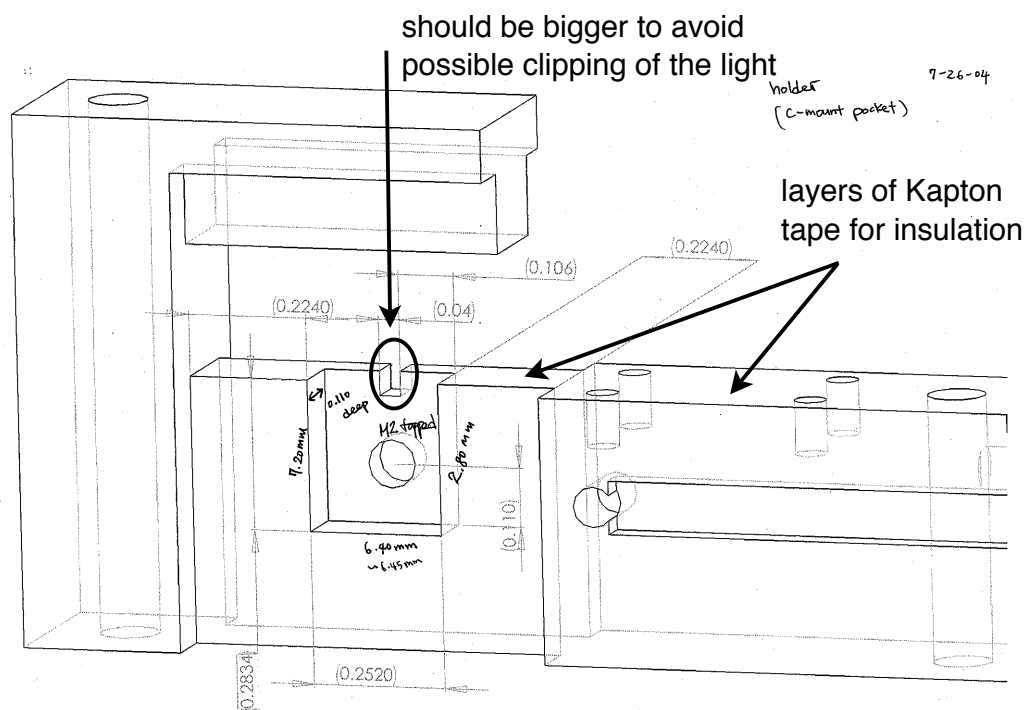


Figure B.2: Detailed dimensions (in inches unless otherwise indicated) of the C-mount pocket. To isolate the lead (either current sourcing or sinking) of the TA chip from the holder, we place 1-2 layers of Kapton on the holder where the lead sits. In addition, a thin piece of indium is sandwiched between the C-mount pocket and the C-mount of the TA chip for a good thermal contact that allows heat to flow away from the chip to the whole copper holder piece.

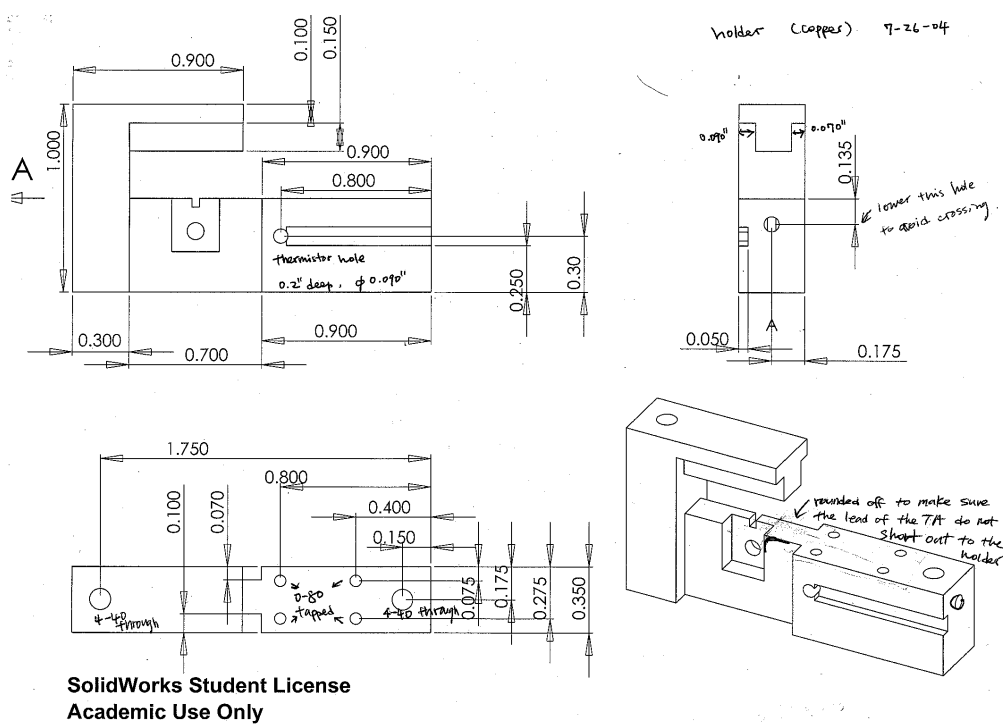


Figure B.3: Detailed dimensions of the TA holder in inches. The “arm”-like structure is to prevent dust falling onto the TA chip and the lens holder touching the chip. This part can be removed.

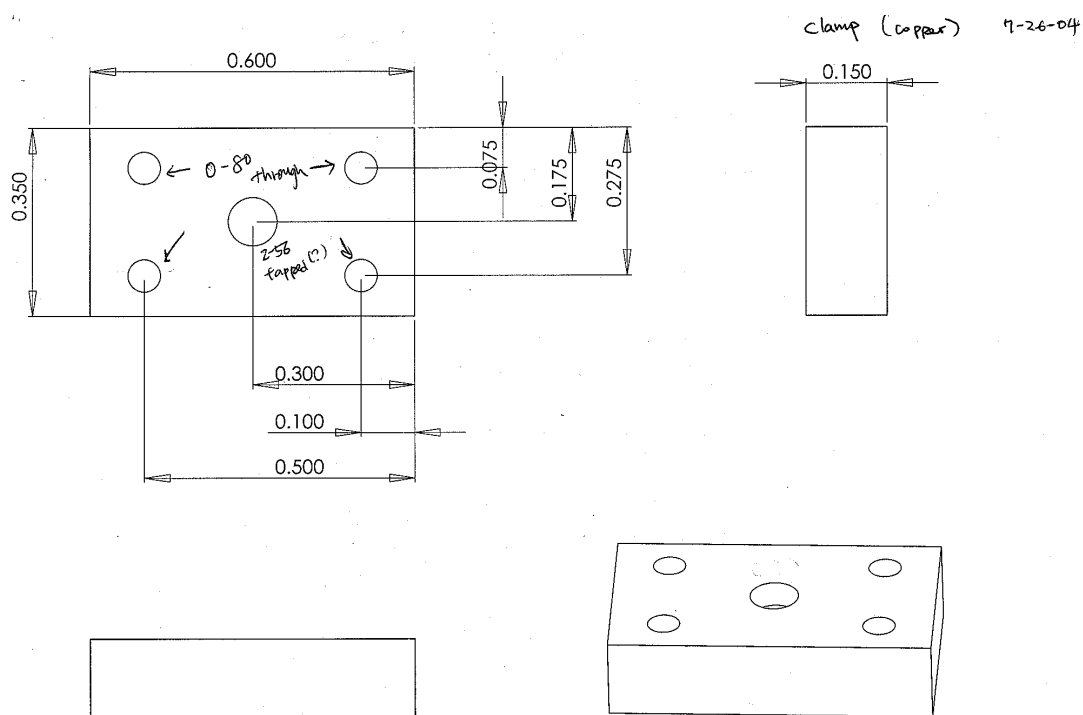


Figure B.4: Detailed dimensions of the clamp. A current source is attached to the clamp through a metal lug that is screwed onto the center screw hole. The clamp itself is screwed onto the TA holder using nylon screws.

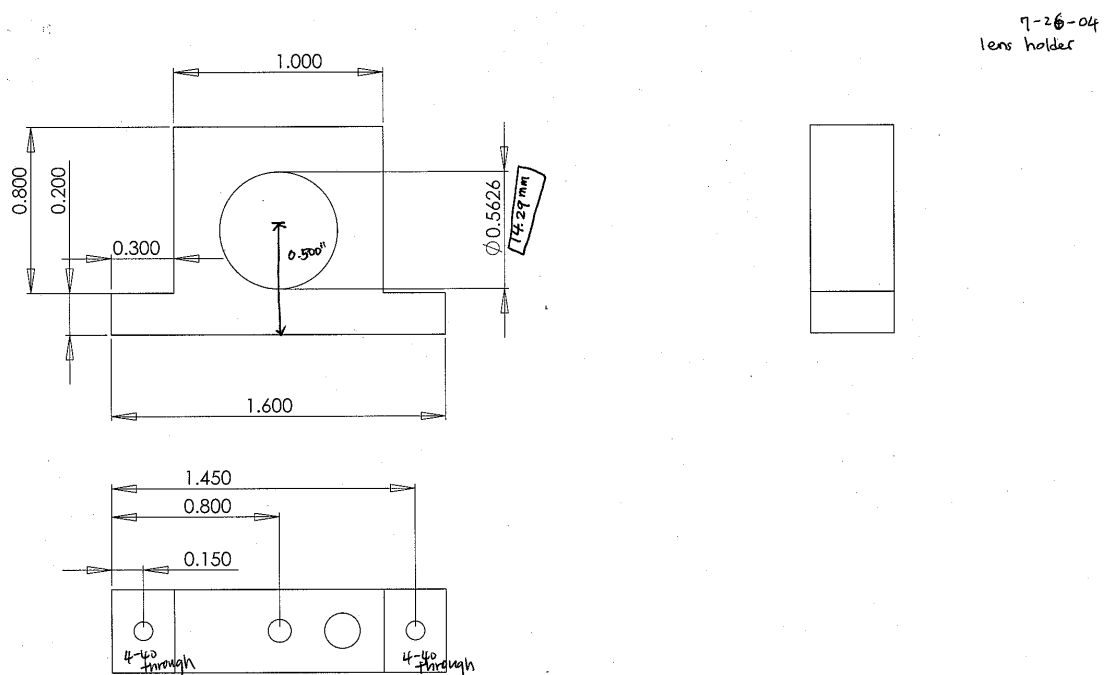


Figure B.5: Detailed dimensions of the lens holder that is used to collimate laser beams going into and out of the TA chip.

adapter 7-26-04

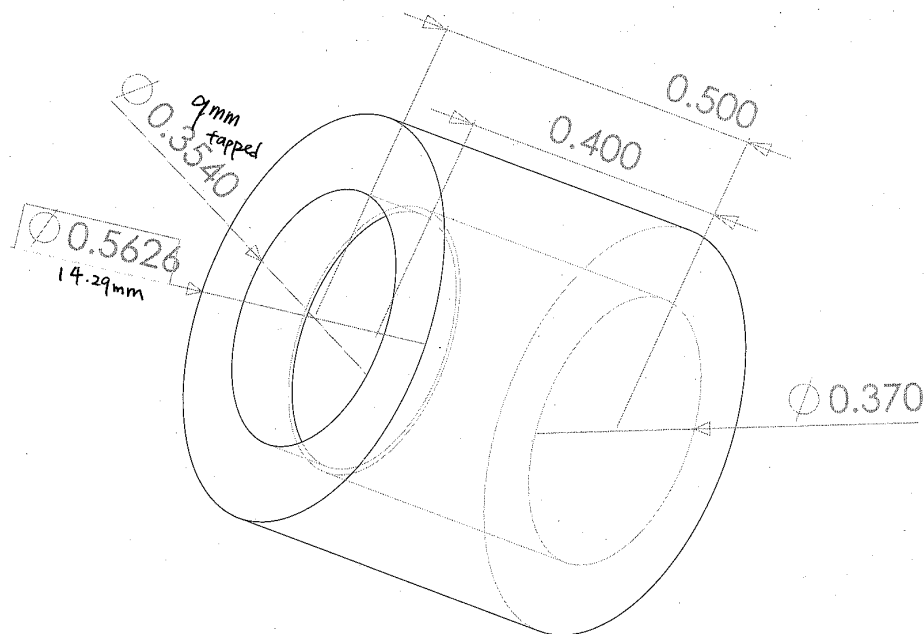


Figure B.6: Lens adapter for Thorlabs Geltech aspheric lens.

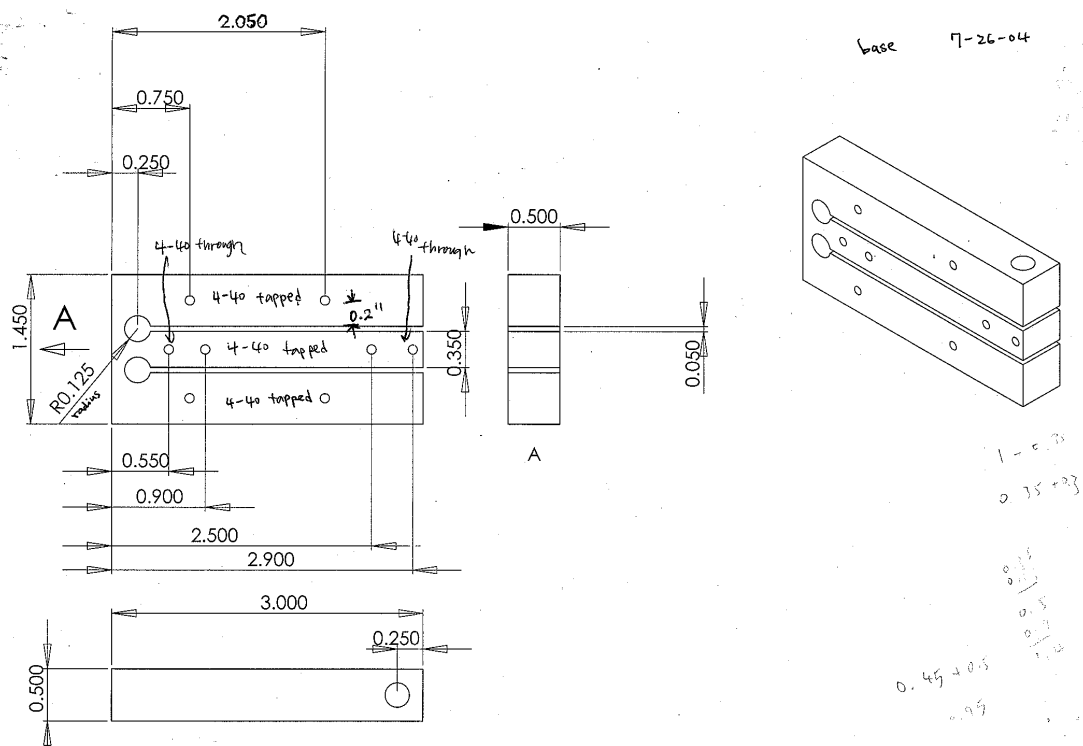


Figure B.7: Detailed dimensions of the flexure mount that is used for fine tuning of the collimation lens position relative to the TA chip.